Geodesics and Resonances of the Manko-Novikov Spacetime

By

Marisa Geyer

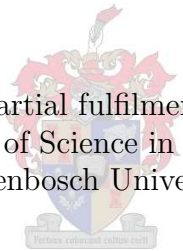

Thesis presented in partial fulfilment of the requirements
for the degree of Master of Science in the Faculty of Science at
Stellenbosch University.

Supervisor : Dr. Jeandrew Brink

Co-supervisor : Prof. Frederik G. Scholtz

March 2013

DECLARATION

By submitting this dissertation electronically, I declare that the entirety of the work contained therein is my own, original work, that I am the sole author thereof (save to the extent explicitly otherwise stated), that reproduction and publication thereof by Stellenbosch University will not infringe any third party rights and that I have not previously in its entirety or in part submitted it for obtaining any qualification.

Abstract

In this thesis I study compact objects described by the Manko-Novikov spacetime. The Manko-Novikov spacetime is an exact solution to the Einstein Field Equations that allows objects to be black hole-like, but with a multipole structure different from Kerr black holes. The aim of the research is to investigate whether we will observationally be able to tell these *bumpy* black holes, if they exist, apart from traditional Kerr black holes. I explore the geodesic motion of a test probe in the Manko-Novikov spacetime. I quantify the motion using Poincaré maps and rotation curves. The Manko-Novikov spacetime admits regions with regular motion as well as regions with chaotic motion. The occurrence of chaos is correlated with orbits for which the characteristic frequencies are resonant. The new result presented in this thesis is a global characterisation of where resonances and thus chaos are likely to occur for all orbits. These calculations are performed in the Kerr spacetime, from which I obtain that low order resonances occur within 20 Schwarzschild radii (or $40M$) of the compact object with mass M. By the KAM theorem, the occurrence of chaos is therefore limited to this region for all small perturbations from Kerr. These resonant events will be measurable in the Galactic Centre using eLISA. This confinement of low order resonances indicates that the frequency values of orbits of radii well outside of 20 Schwarzschild radii can be approximated using canonical perturbation theory.

Opsomming

In hierdie tesis word kompakte voorwerpe bestudeer soos omskryf deur die Manko-Novikov ruimtetyd. Die Manko-Novikov ruimtetyd is 'n eksakte oplossing van die Einstein Veldvergelykings. Die Manko-Novikov ruimtetyd formuleer gravitasiekolk-tipe voorwerpe waarvan die veelpool-struktuur afwyk van die tradisionele Kerr gravitasiekolk-struktuur. Die oogmerk van die navorsing is om vas te stel of ons met behulp van waarnemings hierdie *bonkige* gravitasiekolke van die tradisionele Kerr gravitasiekolke kan onderskei. Ek ondersoek die geodetiese beweging van 'n toetsmassa in die Manko-Novikov ruimtetyd. Die beweging word gekwantifiseer met behulp van Poincaré afbeeldings en rotasiekrommes. In die Manko-Novikov ruimtetyd identifiseer ek gebiede waarbinne reëlmatige beweging voorkom asook gebiede waarbinne chaotiese bane voorkom. Die ontstaan van chaos word geassosieer met bane waarvan die fundamentele frekwensies resonant is. 'n Nuwe resultaat wat in hierdie tesis voorgehou word behels 'n globale karakterisering wat aandui waar resonansies en dus chaos na alle waarskynlikheid voorkom. Laasgenoemde berekeninge word vir die Kerr ruimtetyd uitgevoer. Hierdeur toon ek alle lae orde resonansies kom voor binne 20 Schwarzschild radii (of $40M$) vanaf die kompakte voorwerp met mass M. Die KAM Stelling bepaal dan dat vir alle klein steurings toegepas op die Kerr ruimtetyd die voorkoms van chaos beperk sal wees tot bogenoemde gebied. Die resonansies binne hierdie gebied sal deur eLISA in die sentrum van die melkwegstelsel gemeet kan word. Hierdie beperking van lae orde resonansies tot 'n sekere afstand vanaf die kompakte voorwerp verseker dat die frekwensies van bane wat buite hierdie gebied val, akkuraat deur kanoniese steuringsteorie bepaal kan word.

Acknowledgements

I sincerely thank my advisor Dr. Jeandrew Brink for her continuous guidance and support over these two years. Not only for all the technical advice and help to see this project to an end, but also for all the time and energy devoted to broadening my exposure and enjoyment of general relativity and gravitational wave physics. I thank her for sharing her enthusiasm with me.

I would like to extend my gratitude to the Square Kilometre Array project and the National Research Foundation for providing the financial support for this MSc study. I also thank the National Institute of Theoretical Physics for their contributions and provision of facilities in the final stages of the project.

I would like to thank Ms Christine Ruperti from the Department of Physics at Stellenbosch University for her efficiency and hard work over the years in handling all the administrative aspects of my studies.

A special thanks to Gerrit Oliver and Aaron Zimmerman, peers who endured this thesis with me and greatly contributed to the improvement thereof.

A final thanks to my family and friends for their encouragements and their care.

CONTENTS

Abstract v

Opsomming vi

Acknowledgements vii

LIST OF FIGURES x

1. Introduction and Motivation 1

2. Testing General Relativity 4

   2.1 Extreme Mass Ratio Inspirals 4

   2.2 No-Hair Theorems 5

3. Stationary Axisymmetric Vacuum fields 7

   3.1 The Einstein Field Equations 7

   3.2 SAV metrics 7

      3.2.1 Equations of Motion 9

4. Integrability and Chaos 11

   4.1 Integrability 11

   4.2 Chaotic Orbits 13

   4.3 Nearly Integrable Systems 13

   4.4 Poincaré Maps 14

   4.5 Fixed Points and the Poincaré-Birkhoff Theorem 15

   4.6 KAM Theorem 16

   4.7 Rotation Curves 18

5. Kerr Metric 21

   5.1 Boyer-Lindquist Coordinates 22

   5.2 Prolate Spheroidal Coordinates and Factor Structure Coordinates 23

   5.3 Transformation between Prolate Spheroidal coordinates and Boyer-Lindquist coordinates 24

   5.4 The Effective Kerr Potential 24

      5.4.1 Separating the effective Kerr potential (J) 25

      5.4.2 Physical Space Plots 26

   5.5 Poincaré Maps for Kerr 27

6. Manko-Novikov Metric 30
6.1 Manko-Novikov Coefficients 31
6.2 Metric Characteristics 33
6.3 Physical Space 36
6.4 Orbital Motion 39
6.5 Poincaré Maps 39
6.6 Rotation Curves and Resonances 42
6.7 Observational Signatures 45
6.7.1 Quadrupole deviation 45
6.7.2 Coordinate Frequencies and Fourier Transforms 47
7. Investigating Orbital Behaviour in a Non-convex Effective Potential 50
8. Resonances in Kerr spacetime 55
8.1 The Kerr Fundamental Frequencies 57
8.2 Characterising resonances in the global parameter space 59
8.3 The Relationship between rotation curves and the Keplerian parameter study . . 62
8.4 Resonances with Carlson's Integrals 63
9. Conclusions and Outlook 67
A. Weyl Coordinates 70
B. Manko-Novikov in the Kerr Limit 72
C. Analytical roots for the effective Manko-Novikov potential 75
C.1 Roots of Potential V 75
C.2 Roots of $G - \mu^2$ 76
BIBLIOGRAPHY 80

LIST OF FIGURES

4.1 The toroidal motion for an integrable system with two degrees of freedom. 12

4.2 An integrable system in action angle variables has a circular surface of section of which the intersecting points advance with a constant increase in polar angle. . . . 16

4.3 The surface of section of a perturbed integrable system exhibiting KAM-curves, O-points and X-points. 17

4.4 Calculating the rotation number from a given Poincaré map. 19

4.5 A schematic representation of a rotation curve for a nearly integrable system, indicating the presence of plateaus and inflection points. 20

5.1 The geometry of a Kerr black hole. 22

5.2 Physical space plots of the Kerr metric with changing spin values. 27

5.3 A bounded region of the 3 dimensional effective Kerr potential and the associated Poincaré map. 28

6.1 Ergoregions and regions of closed timelike curves for the Manko-Novikov metric as a function of quadrupole deviation. 34

6.2 Contour lines corresponding to the ergoregion and region of closed timelike curves of the Manko-Novikov spacetime with $q = 0.95$. 35

6.3 The Manko-Novikov physical space for constant angular momentum (L_z) and varying energy (E). 36

6.4 The Manko-Novikov physical space for constant energy (E) and varying angular momentum (L_z). 37

6.5 The three dimensional effective potential of the Manko-Novikov metric with $E = 0.95$, $L_z = 3$, $S = 0.9$ and $q = 0.95$. 38

6.6 Orbital trajectories in the Manko-Novikov potential with $E = 0.95$, $L_z = 3$, $S = 0.9$ and $q = 0.95$. 38

6.7 Poincaré maps of the Manko-Novikov metric for which $E = 0.95$, $L_z = 3$, $S = 0.9$ and $q = 0.95$. 40

6.8 Orbital trajectories associated with certain Birkhoff chains of islands in the corresponding Poincaré maps. 43

6.9 Rotation curves for the Manko-Novikov metric. 44

6.10 The rotation curve for the 1/2-resonance along the line $p_\rho = 0.1$. 45

6.11 Poincaré maps and their associated rotation curves, corresponding to changes in the quadrupole deviation parameter (q). 46

6.12 Oscillatory data and Fourier spectra for the radial and polar coordinates of a Manko-Novikov orbit. 47

6.13 An empirical relationship found between the orbital rotation number and the most prominent peaks in the associated Fourier spectra. 48

7.1 Orbits in a non-convex Manko-Novikov potential. 52

7.2 Poincaré maps corresponding to orbits in a non-convex Manko-Novikov potential. . 53

7.3 Two orbital trajectories in the Manko-Novikov effective potential for which $E = 0.98$ and $L_z = 2$. 54

8.1 Orbital parameters describing trajectories in the Kerr spacetime completely. 56

8.2 The ratio of fundamental Kerr frequencies as a function of the distance from the black hole. 59

8.3 The occurrence of the 2/3-resonance in the Kerr spacetime presented in terms of the global parameter space (p, e, ι) for prograde orbits with different spin values of the black hole. 60

8.4 The occurrence of the 2/3 resonance in the Kerr spacetime presented in terms of p and ι and for a constant eccentricity. Plots for both prograde and retrograde orbits with different spin values of the black hole are shown. 61

8.5 Correlating the relationship between rotation curves and the Keplerian parameter space. 63

A.1 Orbital trajectories of the Manko-Novikov spacetime in Weyl coordinates. 71

B.1 The Manko-Novikov physical space and corresponding Poincaré map in the Kerr limit for which the quadrupole deviation parameter (q) is set to zero. 74

C.1 The roots of potential V. 76

C.2 The biggest numerical root for J is well approximated by the analytical expression presented in this section. 79

CHAPTER 1
Introduction and Motivation

There are restrictive theorems in general relativity that predict that quiescent black holes have simple structures. They are spheroidal objects and defined entirely by only their mass and spin. The metric associated with black holes that obey these No-Hair theorems is the Kerr metric. These uncomplicated Kerr objects are believed to be the end state of any stellar collapse.

In the forthcoming decade we will be able to verify this prediction of the structure of black holes observationally by means of gravitational wave detectors and radio astronomy observations. The expanding ground-based gravitational wave detector network currently consists of more than five detectors globally. Amongst these the Laser Interferometer Gravitational-Wave Observatory (LIGO) in the United States is the most sensitive. A spaced based detector called the evolved Laser Interferometer Space Antenna (eLISA) has also been proposed. Upon completion in 2024 the Square Kilometre Array (SKA) will provide us with a radio telescope that has 10^4 times the survey speed and 50 times the sensitivity of the best current day telescopes.

Since compact objects like black holes curve the spacetime so strongly that not even light can escape from them, measurements of the structure of black holes will have to be done indirectly. One such indirect way in which we can obtain structural information of a black hole is to study the trajectory of a low mass probe as it slowly moves inward around a stationary black hole. These events are termed Extreme Mass Ratio Inspirals (EMRIs), since the central object is several orders of magnitude more massive than the probe. The central object is typically a supermassive black hole and the orbiting test mass a neutron star or white dwarf.

As the orbiting low mass probe slowly spirals in toward the central compact object, the probe loses energy and angular momentum in the form of gravitational waves. Ground-based gravitational wave detectors such as LIGO and space-based detectors like eLISA can detect the gravitational waves emitted by the inspiraling probe. LIGO is typically sensitive to orbits around compact objects with masses below $100M_\odot$ (where $M_\odot$ is the mass of our Sun). eLISA on the other hand has sensitivity in the low frequency band, 10^{-4}Hz - 10^{-1}Hz, which makes eLISA ideal for detecting orbits around compact masses between $10^5 M_\odot$ and $10^7 M_\odot$.

The closest black hole to Earth is Sagittarius A* (SgrA*), which lies at the centre of the Milky Way. SgrA* is a supermassive black hole with a mass of roughly $4.3 \times 10^6 M_\odot$. Its large mass, along with its proximity to Earth, ensures that the associated gravitational wave or radio wave signals coming from the Galactic Centre will be loud and measurable by our detectors. Liu et

al. [43] showed that if the SKA is to find a pulsar orbiting Sgr A* with a beaming frequency of 15 GHz and an orbiting period of less than a year, we will be able to determine the quadrupole moment of Sgr A* with the precision of 1 part in 100. The SKA can also be set up as a pulsar timing array (PTA) to monitor groups of stable millisecond pulsars in the vicinity of Sgr A* [37]. The gravitational waves emitted by the low mass probe falling onto Sgr A* will interrupt the precise beaming frequency of the studied pulsars and be so detected.

From the above observations we seek to answer the question of whether the compact object involved in the EMRI event that was studied is indeed a Kerr black hole or if perhaps the compact object has a more interesting structure. In practice analysing the *structure* of the black hole means measuring its *multipole moments*. An example of a spacetime that describes compact objects more general than the Kerr black hole is the Manko-Novikov metric. The characteristics of this metric are discussed in Chapter 6. In the Manko-Novikov spacetime you can specify all the multipole moments independently, which is not possible in the Kerr metric where they are related to the mass and spin. Compact objects like these, with a multipole moment structure different from Kerr, have been termed *bumpy black holes* by Collins and Hughes [13].

The Kerr spacetime currently provides the basis for the templates for the EMRI searches to be used by LIGO and eLISA. The Kerr spacetime has the feature that all its orbits are integrable, so that given a set of initial conditions, the subsequent motion is predictable. In a more general non-Kerr metric, such as the Manko-Novikov metric, this may not be the case. There exists the possibility that some of the orbits may be chaotic and display sensitive dependence on initial conditions. A more rigorous definition of integrability and chaos is given in Chapter 4.

The question of mathematical interest is to what extent chaos occurs in non-Kerr spacetimes and where. If the EMRI being studied passes through a chaotic region in the spacetime there are several observational implications. In Chapters 6 to 8 we see that the frequency evolution during the orbital inspiral remains constant when the orbit crosses a resonance. In the event of strong chaos, however, the orbit is no longer characterised by distinct frequencies, making detections difficult.

On the other hand if the non-Kerr spacetime is integrable, perturbation theory can be used to analyse the orbital frequencies from which we can infer the structure of the compact object. The first proof of principle for this technique was presented by Ryan in 1995 [53]. He showed that for nearly circular, nearly equatorial orbits the phase evolution of the emitted gravitational radiation encodes all the information of the multipole moments, such as the values of the mass, spin and quadrupole moment.

Most of the detailed investigation of the Manko-Novikov metric to date, such as the studies

performed by Gair et al. [22] and Lukes-Gerakopoulos et al. [45], have focussed on carefully characterising orbital motion for a small subset of the Manko-Novikov parameter space. Trajectories of a particle with fixed energy (E) and angular momentum (L_z) around a black hole of intrinsic spin (S) and quadrupole deviation parameter (q) are explored by plotting their Poincaré maps and computing the rotation curve. In Chapters 6 and 7 I employ a similar strategy by numerically analysing the geodesic motion. Using Poincaré maps I numerically verify that chaotic orbits occur where the frequencies associated with the motion are resonant. This is in accordance with the KAM theorem described in Chapter 4, Sections 4.5 and 4.6. In Chapter 6 I quantify the occurrences of resonances more carefully by computing the rotation number defined in Section 4.7.

The shortfall of exploring a group of orbits with fixed E and L_z is that it only characterises a subset of the parameter space. When we conduct an observational study Nature will not grant us the luxury of labelling the orbits by their parameters *a priori*. For this reason it is important to make statements about the complete parameter range, i.e. about all the possible orbits in a pre-defined spacetime. In Chapter 8 I begin the first quantitative steps for such a global characterisation by studying resonances in the Kerr spacetime. The results so obtained will give an indication of the dynamics involved in small perturbations of the Kerr metric. I find that the lower order resonances and therefore chaos are likely to occur within 20 Schwarzschild radii (or 40M) of the event horizon of the compact object. The astrophysical implications of these results are discussed in Chapter 9 along with an outlook on future studies.

CHAPTER 2
Testing General Relativity

I have mentioned in Chapter 1 that Extreme Mass Ratio Inspiral (EMRI) events are a source of gravitational waves from which we hope to analyse the structure of compact objects. Studying the gravitational waves emitted by the low mass probe falling onto the compact object can in principle uncover whether all black holes are indeed described by the Kerr metric and if deviations from these traditional black holes do exist. In this chapter I will briefly describe the nature of the inspiral laboratory and the measurements we are envisaging in order to test the validity of the No-Hair theorems.

2.1 Extreme Mass Ratio Inspirals

Extreme Mass Ratio Inspirals, as the name suggests, are binary events between two objects that differ greatly in mass – a low mass probe with rest mass μ and a central compact object of mass M. The extreme mass ratio provides an ideal backdrop for analysing black hole spacetimes, since in its limit ($\mu/M \to 0$) the low mass probe acts as a test particle whose dynamics is purely modelled by gravitational effects of the central compact object [28, 27].

Typical examples of low mass probes are neutron stars, white dwarfs, or solar mass black holes, i.e. black holes with a mass of the order of the mass of our Sun ($\sim$ a few $M_\odot$). The hope is to study low mass probes like these as they gradually spiral in onto a highly compact object such as a supermassive black hole at the centre of a galaxy. The probes under consideration will typically spend many years and complete more than 10^5 orbits around the compact object before permanently disappearing from view [22, 25].

Observations have shown that the cores of nearly all nearby galaxies contain a massive compact object, which are generally believed to be black holes [39, 13]. Supermassive black holes (SMBH) are black holes with mass ranging from $10^5 M_\odot - 10^9 M_\odot$. They are most often associated with the centre of galaxies, although the existence of intermediate black holes (IMBH), with masses $10^2 M_\odot - 10^4 M_\odot$, has also been suggested [13].

The theory of general relativity requires that the low mass probe loses energy and angular momentum as it spirals in. This energy and angular momentum are radiated away in the form of gravitational waves, causing the orbit of the probe to shrink. As the orbits shrink the probe moves closer and closer to the compact object. Since the time-scale over which the probe loses energy and angular momenta is much longer than the typical orbital time-scale, it is sensible to

approximate the orbital energy and angular momenta with slowly evolving constants of motion. This is known as the *adiabatic approximation*. The inspiral is so slow, however, that as a first approximation we can consider the probe to always be moving along a *geodesic*. This means I approximate the energy and angular momentum of an orbit with constants of motion.

A realistic portrayal of an EMRI event would include the loss of energy and angular momentum. This however lies beyond the scope of my thesis. For examples of studies that do include the time dependence of the orbital energy and angular momentum see [22, 45].

2.2 No-Hair Theorems

Black holes are believed to form through the gravitational collapse of heavy stars. According to the mathematical theorems known as the *No-Hair theorems*, every black hole is fully described by just three quantities: its mass, spin and charge. All other properties (*hairs*) are lost during the formation process.

The assumptions that underlie the No-Hair theorems are Penrose's Cosmic Censorship Conjecture (CCC) and the assumption that there are no closed timelike curves in the external field of a black hole [32]. These assumptions describe an *astrophysical* black hole, since the CCC ensures that all black holes possess an event horizon* and the assumption of no closed timelike loops excludes time travel within spacetime [11, 31]. I will revisit these requirements in Chapter 5 and 6 when I discuss the Kerr and Manko-Novikov metrics.

By Penrose's CCC [49] all the singularities of an asymptotically flat spacetime are hidden within its event horizon. Since the Kerr black hole has a maximum spin value at which it still exhibits an event horizon, the CCC requires the dimensionless spin parameter χ to satisfy

$$\chi \equiv \frac{c}{G}\frac{S}{M^2} \leq 1, \tag{2.1}$$

where S is the spin of the black hole, M its mass, c is the speed of light and G the gravitational constant. For simplicity I set both c and G equal to 1†. Throughout this thesis I will also work in units of M, i.e. $M = 1$. These simplifications reduce Eq. (2.1) to $S \leq 1$.

Following the assumptions of the CCC and not allowing for closed timelike curves, the No-Hair theorems dictate that all black holes are completely described by their mass, spin and charge. In *Gravitation* by Misner, Thorne and Wheeler (Chapter 33) [47], the authors explain why these

*Beyond the event horizon no particle or photon can escape the gravitational field of the black hole any longer and will plunge onto the black hole.

†This is known as *geometric units*. In geometric units time is interpreted as the distance travelled by light in a given time interval. That means time has geometric units of length. Energy and angular momentum obtain dimensions of length as well. To convert from mass expressed in kilograms to mass expressed in metres we multiply by the conversion factor G/c^2.

three are necessarily the remaining properties. They argue, that of all the quantities that define a source of gravity and electromagnetic radiation, only the mass, charge and spin have unique descriptions in the far out field. All the other initial conditions disappear when the star plunges through the event horizon to form a black hole. Passed the event horizon, no particle or photon can escape back out again. In this way the star loses all its *hairs* as it collapses into a black hole, while the asymptotic flat fields conserve the mass, charge and spin. Even the charge of an astrophysical black hole is believed to be short-lived as it uncharges into the surrounding plasma. The only two remaining quantities needed to describe the black hole then are its mass and spin [12]. In essence this means the Kerr metric (discussed in Chapter 5) is the only stationary, axisymmetric and asymptotically flat solution to the vacuum field equations that describes an astrophysical black hole.

Once the mass M and spin S are known, the No-Hair theorems [23, 24, 30] require that the l-th order multipole moment of the Kerr spacetime depend on the mass and spin through the relation

$$M_l + iS_l = M\left(i\frac{S}{M}\right)^l. \tag{2.2}$$

The mass moment is obtained for $l = 0$ ($M_0 = M$) and the spin moment for $l = 1$ ($S_1 = S$). For $l \geq 2$, M_l has a non-zero value only if l is even and S_l has a non-zero value only for l odd. The quadrupole moment for the Kerr black hole is given by $M_2 = -S^2/M$. This will become an important point of reference when I study how the quadrupole moment of the Manko-Novikov metric deviates from the quadrupole moment of the Kerr spacetime. All Kerr higher order moments can be calculated in a similar manner from Eq. (2.2).

If we were to parameterise the spacetime metric describing a compact object in terms of its multipole moments and observationally measure these moments, we could test whether the No-Hair condition of Eq. (2.2) holds [33, 43].

CHAPTER 3
Stationary Axisymmetric Vacuum fields

3.1 The Einstein Field Equations

In Chapter 1 it was noted that an astrophysical black hole is described by the Kerr metric in agreement with the No-Hair theorems of general relativity (GR). The theory of GR was introduced by Einstein in 1915 in the form of the Einstein Field Equations (EFE). It superseded Newton's theory of gravity by accurately predicting the precession of Mercury's orbit [19]. The EFE's are a non-linear set of equations in spacetime coordinates (i.e. in four dimensions),

$$G_{\mu\nu} = R_{\mu\nu} - \frac{1}{2}Rg_{\mu\nu} = 8\pi G T_{\mu\nu} \tag{3.1}$$

where $G_{\mu\nu}$ on the LHS is the Einstein Tensor and a measure of the curvature of spacetime. It contains the Ricci tensor $R_{\mu\nu}$, Ricci scalar R, and the metric $g_{\mu\nu}$. $T_{\mu\nu}$ on the RHS is the stress-energy-momentum tensor that measures the energy and momentum content of matter. G is the gravitational constant. The relationship described by Eq. (3.1) is popularly interpreted as *matter tells spacetime how to curve and spacetime tells matter how to move*. For background reading on the EFE's and its construction I refer the reader to an introductory textbook on GR such as [10].

After the Field Equations were published in 1915, many scientists worked to find solutions to them. Because of their non-linearity, the only solutions that exist today are those which have assumed certain constraints on the equations. The assumptions most often chosen are that the spacetime being described is stationary, axisymmetric and in vacuum (SAV), as is discussed in the next section.

3.2 SAV metrics

Here I consider Stationary Axisymmetric Vacuum spacetimes. The specific spacetimes considered in this thesis, namely Kerr and Manko-Novikov, are both members of the group of SAV spacetimes. I will briefly look at the formalism of SAV spacetimes as well as the assumptions that go into constructing them. After introducing the general SAV metric, I will continue to introduce first Kerr as a simple example of such a type of spacetime (Chapter 5) and next the Manko-Novikov spacetime (Chapter 6), which will be the focus of subsequent discussion and analysis.

As the name indicates, SAV metrics are firstly stationary, which means the spacetime does not evolve in time. Secondly, it conserves azimuthal angular momentum making it axially symmetric. Thirdly, SAV metrics are in vacuum, such that it describes a gravitational field free of matter exterior to the black hole. Having a stationary metric is physically well motivated, since we expect black holes to be quiescent. The vacuum approximation is analogous to the EMRI limit in which the ratio of the mass of the probe to the mass of the compact object (μ/M) goes to zero. However choosing an axisymmetric spacetime is a simplification purely made in order to have a problem that is mathematically tractable.

An SAV metric can mathematically be expressed as a spacetime with two Killing vectors (written as $\boldsymbol{\partial_t}$ and $\boldsymbol{\partial_\phi}$) which introduce conserved quantities. A Killing vector satisfies the Killing equation,

$$\xi_{a;b} + \xi_{b;a} = 0, \tag{3.2}$$

where the semi-colon indicates the covariant derivative. If the Killing vector is given by $\boldsymbol{\xi} = \partial_x$ then the metric components g_{ab} are independent of x [56]. In the case of an SAV metric, the metric components are independent of both t and ϕ. Without these symmetries we would make little progress in analysing the properties of spacetimes. Note however that a truly realistic spacetime would have no Killing vectors [20].

The Weyl-Papapetrou line element for a SAV spacetime has the general form

$$ds^2 = k^2 e^{-2\psi}[e^{2\gamma}(d\rho^2 + dz^2) + R^2 d\phi^2] - e^{2\psi}(dt - \omega d\phi)^2, \tag{3.3}$$

where ψ, γ, ω and R are functions of the spatial coordinates ρ and z and k is a real constant. Note that the choice $R^2 = \rho^2$ is often made when working in Weyl coordinates. The ρ and z coordinates used here are not necessarily Weyl coordinates. Refer to Appendix A for the transformation between Weyl coordinates (ρ_w, z_w) and the *factor structure* coordinates (ρ, z) used throughout this thesis. For further reading on different SAV coordinate systems I direct the reader to *Exact Solutions of Einstein's Field Equations* Chapter 20 by Stephani et al. [56].

The line element of Eq. (3.3) gives the distance between any two points in the curved SAV spacetime, expressed as a function of the spacetime parameters and the coordinates in question. This line element is known as the Weyl-Papapetrou or sometimes Weyl-Lewis-Papapetrou line element in recognition of the contributors to its form. In 1917 Weyl considered *static* axisymmetric vacuum solutions to the Einstein Field equations [59]. Static in this case means a non-spinning spacetime. Weyl was able to show that metrics of this kind are characterised by two commuting hypersurface orthogonal Killing vectors. Weyl's original work was expanded on by Lewis (1932)

and Papapetrou (1966). They showed that the general line element for an SAV metric which *does* include rotation and admits the Killing vectors $\boldsymbol{\xi} = \boldsymbol{\partial_t}$ (making it stationary) and $\boldsymbol{\eta} = \boldsymbol{\partial_\phi}$ (creating the axial symmetry), has the form given by Eq. (3.3) [56, 41].

The functions ψ, γ, ω and R of Eq. (3.3) can be solved for by means of the Ernst equation for a complex potential $\mathcal{E}$,

$$\Re(\mathcal{E})\vec{\nabla}^2\mathcal{E} = \vec{\nabla}\mathcal{E}\cdot\vec{\nabla}\mathcal{E}. \tag{3.4}$$

Refer to [21] to see how solutions to Eq. (3.4) are obtained. An example of how the line element functions relate to the complex potential $\mathcal{E}$ is that $e^{2\psi}$ is equal to the real part of the potential, $\Re(\mathcal{E})$. The other functions, γ and ω, can also be solved once the potential $\mathcal{E}$ is known. For further reading on SAV spacetimes and solutions to the Einstein Field equations I again refer the reader to Stephani et al. [56] and references therein.

3.2.1 Equations of Motion

In order to study a low mass probe inspiraling into a black hole, or into some highly curved region of a SAV spacetime, we need to understand the dynamics of particles moving within these gravitational potentials. In this section the equations of motion are discussed for a general SAV spacetime. These will be implemented numerically for the Kerr metric in Chapter 5 and Manko-Novikov metric in Chapter 6, respectively.

The Hamiltonian associated with the geodesic motion in a general SAV spacetime is given by the expression

$$\mathcal{H}(\boldsymbol{q},\boldsymbol{p}) = \frac{1}{2}g^{\mu\nu}p_\mu p_\nu \tag{3.5}$$

with $\boldsymbol{q} = (\rho, z, \phi, t)$ and $\boldsymbol{p} = (p_\rho, p_z, p_\phi, p_t)$ the generalised coordinates and conjugate momenta respectively. The metric tensor is $g_{\mu\nu}$. Its entries can be interpreted from the line element in Eq. (3.3) with for example $g_{\rho\rho}$ the coefficient to the $d\rho^2$-term. The inverse of the metric, written as $g^{\mu\nu}$, appears in Eq. (3.5). Note that the expression above makes use of the Einstein summation convention to contract over the indices μ and ν.

To derive the equations of motion for particles in the SAV spacetime, consider the well-known Hamilton's equations $\dot{\boldsymbol{q}} = \frac{\partial\mathcal{H}}{\partial\boldsymbol{p}}$ and $\dot{\boldsymbol{p}} = -\frac{\partial\mathcal{H}}{\partial\boldsymbol{q}}$, expressed with respect to proper time. From this we can show that for a metric independent of t and ϕ (as was suggested through the Killing vectors) it follows that $\dot{p_t} = 0$ and $\dot{p_\phi} = 0$. Conventionally we choose $p_t = -E$ and $p_\phi = L_z$ [13, 22], where E is the conserved energy of the particle in motion, and L_z the azimuthal component of its angular momentum.

After choosing these two constants of motion the original four-dimensional problem has been reduced to a dynamical system with two degrees of freedom. This means that I can split the contraction of the indices of the Hamiltonian into two summations,

$$\mathcal{H} = H = \frac{1}{2}[g^{\alpha\beta}p_\alpha p_\beta + g^{\gamma\delta}p_\gamma p_\delta] \tag{3.6}$$

where α and β run over ρ and z, and γ and δ run over the conserved quantities t and ϕ. The inverse of $g_{\alpha\beta}$ is equal to

$$g^{\alpha\beta} = \frac{1}{k^2}e^{2\psi-2\gamma}\boldsymbol{\delta}^{\alpha\beta}, \tag{3.7}$$

with delta the identity matrix. It follows that

$$H = \frac{1}{2}\Big[\frac{1}{V}(p_\rho^2 + p_z^2) - G\Big] \tag{3.8}$$

with $V = V(\rho, z) = k^2e^{-2\psi}e^{2\gamma}$ and $G = G(\rho, z, E, L_z) = -g^{\gamma\delta}p_\gamma p_\delta$[‡].

Furthermore the Hamiltonian constant, which is the value of the Hamiltonian evaluated along the worldline of the particle [54], is given by.

$$H = -\frac{1}{2}\mu^2, \tag{3.9}$$

where μ is the rest mass of the test particle. The reduced Hamiltonian given in Eq. (3.8) (containing 2 constants of motion) together with the above Hamiltonian constant results in an expression for the effective gravitational potential. Setting Eq. (3.8) equal to Eq. (3.9) fixes the sum of the squares of the two remaining momenta such that

$$J(\rho, z, E, L_z, \mu) \equiv (G - \mu^2)V = p_\rho^2 + p_z^2, \tag{3.10}$$

where J can be interpreted as the effective gravitational potential. Substituting Eqs. (3.8) and (3.10) into Hamilton's equations, the geodesic equations of motion obtain the form

$$\dot{q}_i = \frac{p_i}{V} \qquad\qquad \dot{p}_i = \frac{\partial_{q_i}J}{2V}, \tag{3.11}$$

with the index i running over ρ and z and the derivative taken with respect to proper time[8]. These will be used for analysing geodesic motion in the Kerr and Manko-Novikov spacetimes.

[‡]This G should not be confused with the gravitational constant of Section 2.2. The gravitational constant is set equal to 1 throughout this thesis.

CHAPTER 4
Integrability and Chaos

In Chapter 3 it was shown that SAV spacetimes are constructed by admitting two Killing vectors or two constants of motion. The more conserved quantities exist the easier it becomes to handle the dynamical equations and understand orbital motion within the spacetime. The Kerr solution to the Einstein Field Equations is an example of an SAV metric where apart from the conventional constants of motion, namely energy E, angular momentum L_z and rest mass μ, an extra conserved quantity, known as the Carter constant Q, exists. I will discuss the Kerr metric in more detail in Chapter 5.

In this chapter I analyse the nature of chaotic and integrable systems. Thereafter I consider the relevant theorems for uncovering conserved quantities in a pre-defined spacetime. There are two mathematical theorems of particular interest to my thesis, the Poincaré Birkhoff Theorem and the KAM theorem. These theorems help devise a classification scheme to describe chaotic behaviour in conservative systems [55].

4.1 Integrability

A system for which the Hamiltonian has a maximum number of mutually independent constants of motion is said to be *integrable*. This implies that for a system of N degrees of freedom, the Hamilton-Jacobi equations are separable into N independent equations [55]. Consider a Hamiltonian system $H(\boldsymbol{q}, \boldsymbol{p})$ described by the generalised coordinates $\boldsymbol{q}$ and conjugate momenta $\boldsymbol{p}$. In the case of an integrable system there exists a suitable choice of canonical coordinates $(\boldsymbol{Q}, \boldsymbol{P})$, known as the *action angle variables*, for which the new momenta P_i are constants of motion and the new coordinates Q_i vary linearly in time [4, 60, 55].

In mathematical terms this means that a Hamiltonian $H(\boldsymbol{p}, \boldsymbol{q})$ is integrable if there exists a characteristic function $W(\boldsymbol{q}, \boldsymbol{P})$ which generates the new action angle variables $\boldsymbol{Q}$ and $\boldsymbol{P}$ by means of the equations

$$\boldsymbol{p} = \frac{\partial W(\boldsymbol{q}, \boldsymbol{P})}{\partial \boldsymbol{q}} \qquad\qquad \boldsymbol{Q} = \frac{\partial W(\boldsymbol{q}, \boldsymbol{P})}{\partial \boldsymbol{P}}. \tag{4.1}$$

It is required that in the new coordinates the Hamiltonian depends only on the new momenta $\boldsymbol{P}$. This is similar to ensuring that $W(\boldsymbol{q}, \boldsymbol{P})$ is a solution to the Hamilton-Jacobi equation,

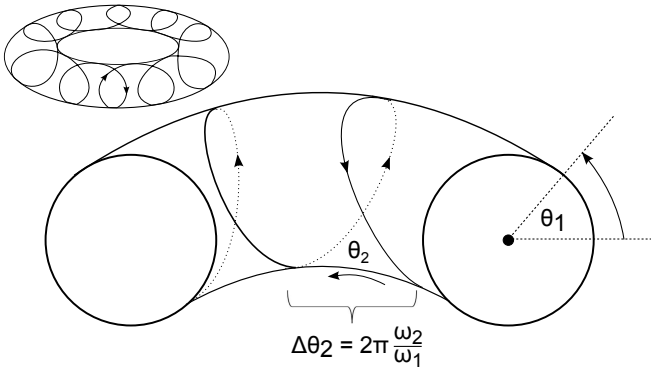

Figure 4.1: **The orbits in an integrable system with two degrees of freedom can be visualised as trajectories wrapping around a two dimensional torus with characteristic frequencies ω_1 and ω_2, relating to the angular advances θ_1 and θ_2. For rational values of ω_2/ω_1 the orbital trajectory will retrace its path, while for irrational values of ω_2/ω_1 a trajectory will fill the torus densely.**

$$H(\boldsymbol{q}, \partial W/\partial \boldsymbol{q}) = \Big[\boldsymbol{q}, \partial W/\partial \boldsymbol{q}\Big] = \bar{H}(\boldsymbol{P}), \tag{4.2}$$

where the definition of the Poisson bracket has been used and $\bar{H}(\boldsymbol{P})$ is the form of the Hamiltonian which only depends on the new momenta $\boldsymbol{P}$ [60, 55].
The equations of motion in $\boldsymbol{P}$ and $\boldsymbol{Q}$ are now equal to

$$\dot{\boldsymbol{P}} = -\frac{\partial \bar{H}}{\partial \boldsymbol{Q}} = 0 \qquad\qquad \dot{\boldsymbol{Q}} = \frac{\partial \bar{H}}{\partial \boldsymbol{P}} = \omega(\boldsymbol{P}). \tag{4.3}$$

Integrating the above gives a set of constants of motion and a set of coordinates with periodicity in time

$$\boldsymbol{P} = \text{constant} \qquad\qquad \boldsymbol{Q} = \boldsymbol{\omega} t + \boldsymbol{k} \tag{4.4}$$

For each pair of action angle variable coordinates (P_i, Q_i) the orbits of these integrable systems are nested circles with radius P_i and polar angle Q_i. For N pairs of action-angle variables, the orbits lie on N-dimensional invariant tori in the $2N$-dimensional phase space [60, 55]. If we consider an integrable system with two degrees of freedom, that is a four-dimensional phase space (as is the case for Kerr spacetime), we can express the motion as trajectories winding around a 2-dimensional torus. Periodic orbits that follow the same trajectory as it spirals around the torus will only occur if the ratio of the characteristic frequencies associated with each coordinate

degree of freedom is a rational fraction, i.e.

$$\frac{\omega_2}{\omega_1} = \frac{m}{n} = \text{rational} \qquad m, n = 1, 2, 3... \tag{4.5}$$

with the ω's as calculated from Eq. (4.4). Orbits for which the ratio of characteristic frequencies have a rational fraction value, are often called *resonant* orbits, for reasons that will become clear in Sections 4.5 and 4.6.

Figure 4.1 illustrates this for a system with two degrees of freedom. In the figure the average angle with which the orbit advances as it wraps around the torus is labelled $\Delta\theta_2$. This angle can be expressed in terms of the characteristic frequencies such that $\Delta\theta_2 = 2\pi(\omega_2/\omega_1)$. If ω_2/ω_1 is a rational fraction, $\Delta\theta_2$ will be a rational fraction of 2π such that, after a sufficient amount of windings, the trajectory will retrace its path. For irrational frequency ratios the orbit never retraces its path, but fills the entire torus densely over time.

In Chapter 8 I will utilise the above action angle variable formalism in order to compute the occurrence of low-order resonances for all orbits in the Kerr spacetime.

4.2 Chaotic Orbits

In contrast to the periodicities exhibited by orbits of integrable systems, non-integrable systems can display chaotic orbits. Orbits are considered chaotic if the long-term behaviour of the orbit remains non-periodic and the orbit depends sensitively on its initial conditions. This sensitive dependence on initial conditions is quantified mathematically by a positive Lyapunov exponent. A positive Lyapunov exponent of a given orbit characterises the mean exponential rate with which other trajectories surrounding the orbit diverge away from it [57, 42]. As was noted in Chapter 1, the existence of orbits that are sensitive to initial conditions will hinder the extraction of physical properties from observational data.

4.3 Nearly Integrable Systems

We have seen that the integrability of Hamiltonian systems depends on the system having a maximum number of independent constants of motion. In Chapter 5 I will consider the Kerr metric as an example of an integrable system, where the additional constant of motion is known as the Carter constant [12]. A next system of interest is one where the Hamiltonian is not exactly integrable, but *nearly integrable* instead. Near-integrable systems are system for which the Hamiltonian can be expressed as the Hamiltonian of an integrable system plus some

perturbation of the integrable Hamiltonian,

$$H = H_0 + \epsilon H_1, \tag{4.6}$$

where $H_0 = H_0(\boldsymbol{P})$ is the unperturbed Hamiltonian which is only a function of the actions $\boldsymbol{P}$ in Eq. 4.4. $H_1 = H_1(\boldsymbol{P}, \boldsymbol{Q})$ is a periodic function called the perturbation Hamiltonian and $\epsilon << 1$.

Whether nearly integrable systems can remain stable was a question central to the celestial mechanics of the nineteenth century. During this period mathematicians like Hamilton, Liouville and Poincaré were attempting to find solutions to the so called N-body problem. The N-body problem describes the motion of N masses interacting according to Newton's laws of gravitation. Through fossil records and other observations scientists were motivated to believe in the long-time stability of our solar system and yet they had difficulty proving this mathematically [60, 42].

For $N \geq 3$ the problem is not solvable in general, but the hope was that, if the three body system was treated as a perturbation of the integrable two body problem, an approximate solution could be found. This promoted the refinement of perturbation techniques. The two particular mathematical difficulties that arose within these techniques were the so-called problem of *secular terms* and the problem of *small divisors* [60].

Secular terms are often formed when expansions of the generalised coordinates used in perturbation theories lead to coordinate solutions that have a form such as $t \sin t$, when the solution should have been periodic instead. These types of solutions are only valid for very small times, which is unfortunate since in celestial mechanics the long-time scales are of great importance. Several methods were discovered to overcome this problem, most of which are known as the *averaging method*. The small divisors problem is introduced when the ratio of the characteristic frequencies of the system is rational, consequently causing the characteristic function (W from Section 4.1) to diverge [60, 50, 40]. The system cannot be integrated by perturbation theory for rational ratios because of these periodicities, and can at best be solved for irrational valued ratios if the perturbation series converges [55]. Side stepping the small divisor problem is much harder than solving the secular terms and was only finally overcome by the advent of the KAM theorem, which will be discussed in Section 4.6.

4.4 Poincaré Maps

At the same time of the development of perturbation techniques, Poincaré was developing a qualitative approach for dealing with the N-body problem. He suggested that a dynamical system can be represented geometrically through its *phase portrait*. The phase portrait is made up of all the trajectories which are solutions to the equations of motion of the system. These are

plotted in phase space as *orbits* or *paths* where time varies along the trajectory [60].

Since it is hard to visualise a four dimensional phase space, a two dimensional slice of the space is often chosen in which to map features of the dynamics of the system. A Poincaré map studies the successive intersections that several orbits make with the chosen two dimensional surface of section. Each time a trajectory pierces this surface, a point in the map is generated. The plot produced by a sufficient amount of successive piercing points for several orbits, is the Poincaré map as shown in Figure 4.4. If dots in a Poincaré map produce a closed curve it indicates a conserved orbital quantity, since this means that after enough iterations all the possible values, lying between the constrained minimum and maximum value of each of the two parameters, in the surface of section had been explored. This is similar to the orbits having covered the phase space torus densely over time as was explained in Section 4.1. Poincaré maps therefore facilitate the search for invariant quantities in a perturbed Hamiltonian system and can assist quantifying to what extent orbits are deviating from the paths associated with the related integrable system. In this thesis Poincaré maps will be utilised when I consider the integrability of both the Kerr and Manko-Novikov spacetime.

4.5 Fixed Points and the Poincaré-Birkhoff Theorem

One of the first properties of these maps that Poincaré investigated was that of *fixed points*. Fixed points are either points on the Poincaré map that get mapped onto themselves and therefore correspond to simple periodic orbits that close after crossing the surface of section once [60] or alternatively they can correspond to orbits with higher periodicity whose trajectories will close after crossing the surface a number of times.

From Section 4.1 we know that a completely integrable Hamiltonian system can be transformed to action angle variables. In this coordinate system the tori will have concentric circles as their surface of sections. Each point in a concentric circle is one pair of action angle variables which can be chosen to imitate polar coordinates (r, θ). As an orbit of the system spirals around the torus it will intersect the surface of section each time with a constant increase in polar angle $(\Delta\theta = \alpha)$ as shown in Figure 4.2. The polar angle can depend on the radius of the circle, varying from torus to torus, i.e. from orbit to orbit. As you move from one torus to the next, $\alpha/2\pi$ will change continuously, covering both irrational and rational values.

Poincaré investigated what would happen to this structure if both r and θ are slightly perturbed. He conjectured, and Birkhoff later proved, [6, 60] that a small change in the Hamiltonian will destroy most of the fixed points (i.e. orbits for which the ratio of frequencies are rational). He showed that under small perturbations the original torus breaks up into smaller tori. For

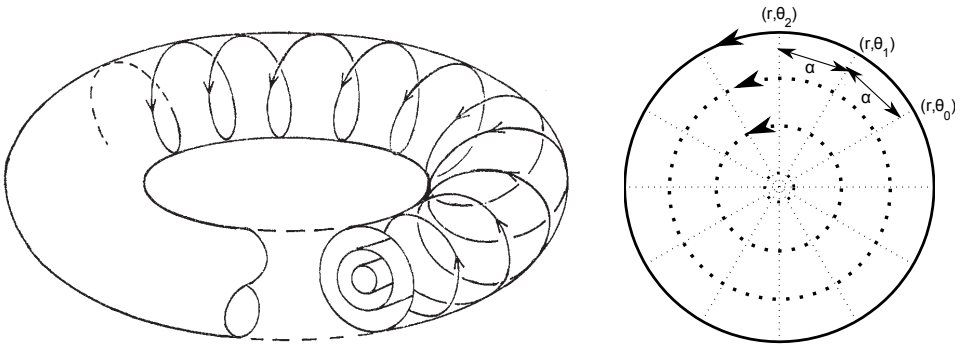

Figure 4.2: **An integrable system in action angle variables will necessarily have a circular phase space surface of section, where each concentric circle is defined by a pair of action angle variables (r, θ), chosen to correspond to polar angles. As an orbit in the system winds around the torus it will pierce the $r - \theta$ surface of section with a constant increment α in polar angle. Moving from one torus to the next α will change as a function of the radius of the circle.**

$\alpha/2\pi = m/n$, only an even multiple of n fixed points will remain. This is known as the *Poincaré Birkhoff-Theorem*. The breaks of the tori are most prominent for low order rational fractions, i.e. 1/2, 2/3 etc. For this reason these orbits are often called resonant orbits.

Two types of fixed points are distinguished, namely X-points and O-points. O-points, also known as stable points, are surrounded by elliptically shaped invariant curves. These islands of elliptical curves are often termed the *Birkhoff Chains of Islands* or *Islands of stability* [51, 5]. The width of the islands increases as the deviation from the integrable system grows [1]. An interesting property of the Birkhoff chains of islands that I investigate in this thesis is the fact that, although the characteristic frequencies associated with the orbits in the island change, the rational ratio of the frequencies remains unchanged throughout the island.

The X-points on the other hand are unstable and surrounded by hyperbolic chaotic curves. These curves form a thin chaotic layer around the islands of stability. As long as the deviation from the integrable system remains small, however, the chaotic areas as seen on the surface of section are constrained to a very narrow band. An equal number of O- and X-points exists and are arranged alternately around an unperturbed invariant curve [60] as can be seen in Figure 4.3.

4.6 KAM Theorem

The Poincaré-Birkhoff theorem from Section 4.5 teaches that perturbations can destroy the tori associated with fixed points, i.e. with periodic orbits. This theorem however draws no conclusions about the other invariant curves. Are all invariant tori destroyed by the introduction of small perturbations to an integrable Hamiltonian? The answer to this question lies with the work by Kolmogorov (1954), Arnold (1963) and Moser (1962). Their collective effort, known as

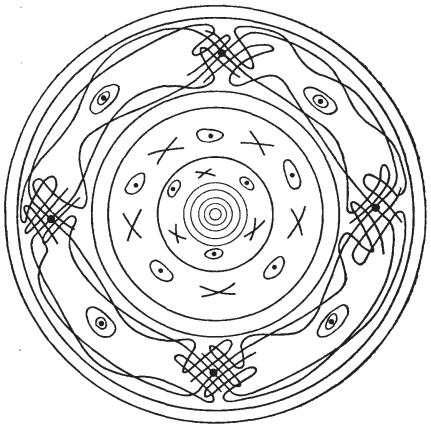

Figure 4.3: The surface of section of a perturbed integrable system as shown in Arnold's paper of 1963 [2, 60]. The perturbations cause the rational tori to break up into a finite number of periodic orbits, that show up as alternate O- and X fixed points in the surface of section. The irrational surface remain as invariant tori. These invariant curves in the surface of section are called KAM-curves.

the KAM-theorem, finally showed that integrable systems which are slightly perturbed will preserve the integrability of orbits for most initial conditions, through the presence of KAM-curves. In particular all tori for which the ratio of associated characteristic frequencies is *sufficiently irrational* will remain stable under a small perturbation of the Hamiltonian [55]. This means the tori for which the ratio of frequencies satisfy

$$\left|\frac{\omega_2}{\omega_1} - \frac{m}{n}\right| > \frac{k(\epsilon)}{n^{2.5}} \qquad m, n = 1, 2, 3... \quad \text{and} \quad k(\epsilon \to 0) \to 0 \tag{4.7}$$

are stable under the perturbation ϵH_1 (as presented in Eq. 4.6) in the limit $\epsilon << 1$ [55, 42].

The domain of frequency ratios ω_2/ω_1 for which the above does *not* hold, in other words for which the tori will become unstable, increases for lower values in n. This means for example that for more frequency values close to the 2/3-resonance will orbits become unstable, than for the 3/4-resonance.

The KAM theorem therefore shows that, when an integrable Hamiltonian is perturbed, every torus associated with a rational ratio of frequencies is destroyed, leaving only an even number of periodic orbits. On a Poincaré surface of section half of the remaining periodic orbits will appear as O-points and half of them as X-points. However, provided that the perturbation is small enough, the sufficiently irrational surfaces will still exist as invariant tori, i.e. they will remain as closed curves on the Poincaré map. Figure 4.3 shows the break-up of irrational and rational surfaces schematically.

The invariant curves surrounding the O-points have a fractal structure. Zooming in on the

tori surrounding the O-point we again see the break-up of rational surfaces and the stability of most of the irrational surfaces. For mathematical reviews and or proofs of the KAM theorem I refer the interested reader to [3, 48].

The KAM theorem finally addressed the issue of the stability of the solar system. If you consider the Earth's motion about the Sun as a completely integrable two-body problem and then introduce the other planets in the solar system as perturbations to the problem, the perturbation could possibly lead to the instability of the Earth's orbit [60]. However with the results of the KAM-theorem, Arnold [2] was able to show that the motion of all the planets will remain bound, except for a very specific set of initial conditions.

4.7 Rotation Curves

In Section 4.5 we investigated measuring the constant angle (α) between successive piercings in the Poincaré surface of section for an integrable Hamiltonian system expressed in action-angle variables. Finding a value for $\alpha/2\pi$ in turn gives the value for the ratio of characteristic frequencies associated with the system ($\alpha/2\pi = \omega_2/\omega_1$). This angle expressed as a fraction of a circle is called the *rotation number* [18, 58].

It remains useful to calculate the rotation number even when the system is nearly integrable and therefore not expressible in action angle variables and does not have a circular surface of section. In this case the angle with which each piercing in a Poincaré map advances will not be constant, but the convergent average angle of advance is still an indicator of the ratio of characteristic frequencies of the system.

The rotation number is often expressed as a function of a phase space coordinate. Refer to Section 4.5 where α for example was a function of the radius of the circular surface of section. Plotting the dependence of the rotation number on some system parameter gives the *rotation curve*. Most often the choice is made to plot the rotation number as a function of the orbital distance to the central fixed point of the Poincaré map. In action angle variables the distance from an invariant curve to the central fixed point is just the radius of the circular slice.

From Chapter 3 we know that the Hamiltonian associated with an SAV metric has two conserved quantities, $p_t = -E$ and $p_\phi = L_z$, which reduces the Hamiltonian to a two degree of freedom problem. The rotation number can therefore be used to indicate whether the frequencies related to the remaining two parameters, namely ω_r and ω_θ (or ω_ρ and ω_z in factor structure coordinates, see Section 5.2), have a rational or irrational ratio.

The rotation number of a nearly integrable system is determined from its Poincaré map as shown in Figure 4.4. Consider a closed curve within a Poincaré map corresponding to a specific

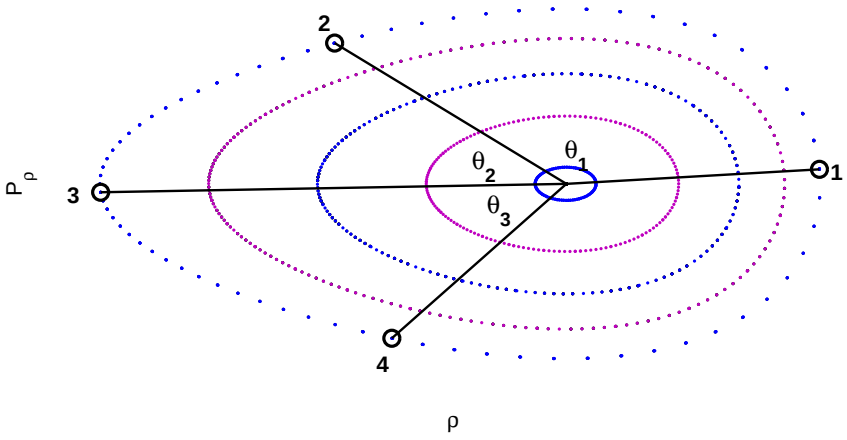

Figure 4.4: Calculating the rotation number from a given Poincaré map. Each dot in this figure represents an orbital trajectory piercing the $\rho - p_\rho$ surface from below. Four successive piercings of this surface of section is labelled 1 to 4. In order to calculate the rotation number (and hence find an estimate for the ratio of the characteristic frequencies of the orbit), calculate the clockwise angle between a sufficient amounts of successive piercings. The rotation number of a given orbit is found by averaging over the calculated angles (to obtain an average angle of advance) and then by expressing this value as a fraction of a circle. Refer to Eq. (4.8)

set of initial conditions. Label one of the piercings in the chosen surface of section as the i^{th} piercing. The next piercing on that curve is then the $(i+1)^{th}$ piercing and the clockwise angle between these two dots, relative to the fixed point at the centre of the map, is given by θ_i. Calculate θ_{i+1} and the successive angles in a similar way. In the limit where the number of angles calculated goes to infinity, the average angle expressed as a fraction of a circle is equal to the rotation number for a given orbit. The mathematical expression corresponding to the above evaluation is

$$\nu_\theta = \lim_{N\to\infty} \frac{1}{2\pi N} \sum_{i=1}^{N} \theta_i, \tag{4.8}$$

where θ_i is the clockwise angle between the i^{th} and $(i+1)^{th}$ piercing [45].

Note that when the rotation number is determined from a Poincaré map plotting ρ against p_ρ as in Figure 4.4 it will have a rational value whenever the number of oscillations along the spatial axis *piercing* the surface of section (the z-axis) is equal to a finite number of oscillations along the other spatial axis (the ρ-axis) [1]. The rotation number therefore relates to the characteristic frequencies of the system through

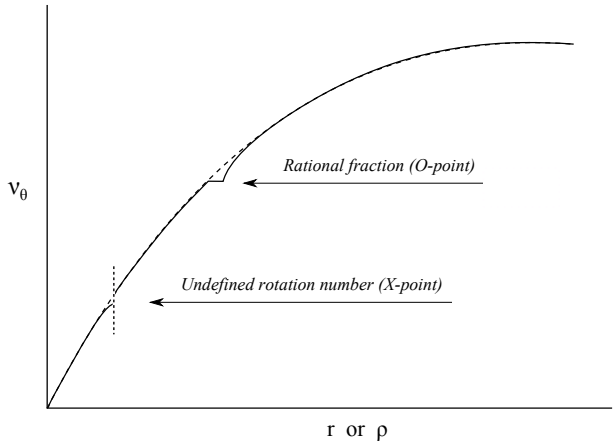

Figure 4.5: **For every rational fraction valued rotation number the rotation curve shows a plateau. This plateau corresponds to the Birkhoff chains of islands in the corresponding Poincaré map. Within these islands of stability the rotation number remains a constant. An inflection point on the rotation curve corresponds to an unstable orbit associated with an X-point, for which the rotation number is undefined. The underlying dashed curve shows the rotation curve for an integrable system such as Kerr. It has no plateaus or points of inflection.**

$$\nu_\theta = \frac{m\,\omega_\rho}{n\,\omega_z}, \tag{4.9}$$

with m and n integer numbers.

The rotation curve is obtained by plotting the rotation number as a function of the distance to the centre of the Poincaré map or similarly an initial spatial coordinate. For an integrable case such as Kerr we expect the rotation curve to be a smooth and monotonically increasing curve. (Depending on which frequency you choose as the denominator it could also be monotonically decreasing). However, in a nearly integrable case the rotation curve has many plateaus, each corresponding to a rational value of the rotation number and signifying a resonance breaking regular motion. This is shown schematically in Figure 4.5. The plateaus show that, within the Birkhoff chains of islands surrounding the O-points, the rotation number remains constant. In contrast, rotation numbers associated with unstable X-points are undefined since these points are surrounded by thin domains of chaos. These undefined rotation numbers show up as inflection points on the rotation curve. In Chapter 6 I will make use of rotation curves to investigate the occurrence of resonances in the Manko-Novikov metric.

CHAPTER 5
Kerr Metric

After Einstein introduced his theory of general relativity and the accompanying Field Equations (see Section 3.1), many physicists and mathematicians were interested in finding possible solutions to this set of 4 by 4 symmetric tensor equations. The equations are non-linear and their solutions not trivial.

One of the first solutions was discovered by Karl Schwarzschild in 1915. The Schwarzschild solution describes a non-rotating and uncharged black hole, which in its radial asymptotic limit reduces to flat spacetime. It wasn't however until the sixties that Roy Kerr would come up with a metric which included a *rotating* black hole in its description. The Kerr solution was first published in *Physics Review Letters* in 1963 [35]. For a more recent review by Kerr, where he discusses the details of this historical event and notes the excitement of finally showing the solution he had found supported rotation, refer to [36].

A rotating solution was important to describe an astrophysical black hole since black holes are believed to form through the gravitational collapse of massive stars and such a formation process is unlikely to result in a non-spinning compact object.

In this thesis the Kerr metric serves both as an example of a well-studied integrable SAV metric and as a base metric for Manko-Novikov, which reduces to Kerr when the quadrupole deviation is dialled to zero. The Kerr metric describes an asymptotically flat SAV metric, with two Killing vectors $\boldsymbol{\partial_t}$ and $\boldsymbol{\partial_\phi}$. However, apart from these two constants of motion introduced through symmetry, it was famously shown by Carter in 1968 [12] that the metric admits another constant of motion – which became known as the Carter constant. It is due to the separability of the Hamilton-Jacobi equations for Kerr that a fourth conserved quantity (after energy, angular momentum and the Hamiltonian constant) exists. The separability of the Hamilton-Jacobi equations ensures that Kerr is completely integrable. This means, as discussed in Section 4.1, that the Kerr metric can be rewritten in terms of action angle variables. The action angle formalism for Kerr was explored by Schmidt [54]. In his paper he derives expressions for computing the (invariant) fundamental orbital frequencies of the Kerr metric. I will get back to his work in Chapter 8 when I analyse the occurrence of resonances in the Kerr spacetime.

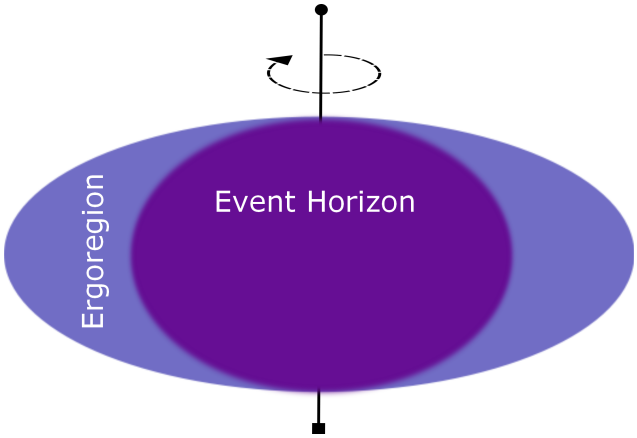

Figure 5.1: A schematic representation of the shape a Kerr black hole which shows the ergosphere and event horizon. The static limit and horizon touch where they are intersected with the black hole's axis of rotation, i.e. at $\theta = 0$ and π. Elsewhere the regions are well separated, unless the black hole is non-spinning ($a = 0$), in which case the Kerr black hole reduces to the Schwarzschild solution where the static limit and horizon coincide such that the ergoregion disappears.

5.1 Boyer-Lindquist Coordinates

Although the Boyer-Lindquist coordinates are not the coordinates in which Kerr originally formulated the spacetime, it is the coordinate system most often used because it allows for convenient physical interpretations. As we will see below, Boyer-Lindquist coordinates offer a relatively simple picture of the event horizons, limits and singularities of the Kerr metric, presented in Figure 5.1.

In Boyer-Lindquist coordinates the external gravitational field of the black hole, i.e. the gravitational field outside of the event horizon, is described by the line element,

$$\begin{aligned} ds^2 = &-\frac{\Delta}{\Sigma}\left(dt - a\sin^2\theta d\phi\right)^2 + \frac{\sin^2\theta}{\Sigma}\left((r^2+a^2)d\phi - adt\right)^2 \\ &+ \frac{\Sigma}{\Delta}dr^2 + \Sigma d\theta^2 \end{aligned} \tag{5.1}$$

where $\Sigma = r^2 + a^2\cos^2\theta$, $\Delta = r^2 - 2Mr + a^2$, M is the mass of the black hole and $a = S/M$ is the spin of the black hole per unit mass.

All the metric coefficients are independent of t and ϕ, which shows that Kerr is indeed stationary and axisymmetric. The intrinsic spin of the black hole causes inertial frames in the surroundings of the black hole to be dragged along. The closer the frame lies to the black hole, the more dramatic the dragging effect becomes. This introduces a precession effect relative to distant stars.

At the surface

$$r_s = M + \sqrt{M^2 - a^2 \cos^2 \theta} \tag{5.2}$$

the dragging is so extreme that no observer can remain at rest anymore (relative to distant stars). All observers will orbit the black hole in the same direction as the rotation of the black hole itself. This surface is known as the *static limit*.

The *horizon* or *event horizon* of the Kerr black hole is located at

$$r = r_H = M + \sqrt{M^2 - Q^2 - a^2}, \tag{5.3}$$

where Q is the fourth constant of motion or the Carter constant. No particle or photon, once it has passed the horizon, can ever escape back out again. The area that lies between the static limit and inner horizon is called the *ergoregion* or *ergosphere*.

The above mentioned Carter constant expressed in terms of Boyer-Lindquist coordinates has the form [47]

$$Q = p_\theta^2 + \cos^2 \theta [a^2(\mu^2 - E^2) + \frac{1}{\sin^2 \theta} {L_z}^2] \tag{5.4}$$

where p_θ is the θ-component of the four-momentum and a, μ, E, L_z the spin of the black hole and the rest mass, energy and angular momentum of the inspiraling probe respectively.

5.2 Prolate Spheroidal Coordinates and Factor Structure Coordinates

While the Boyer-Lindquist coordinates are valuable for understanding the physical properties of the black hole, prolate spheroidal coordinates are helpful to show the separability and therefore integrability of the Kerr potential. I will discuss the separability of the effective Kerr potential in Section 5.4. Prolate spheroidal coordinates (x, y) also serve you well when you generalise from the Kerr metric to the Manko-Novikov metric. For this reason most of the calculations in the thesis will be done in this coordinate system. Most often I will make the choice $x = \cosh \rho$ and $y = \cos z$, where (x, y) are the prolate spheroidal coordinates and (ρ, z) factor structure coordinates [8]. These should not be confused with the Weyl coordinates (ρ_w, z_w) used in [22, 45]. Since much of the work done on the Kerr metric is presented in Boyer-Lindquist coordinates however, I will give the needed transformation between the coordinate systems next.

The Kerr line element in prolate spheroidal coordinates is

$$ds^2 = k^2 e^{-2\psi_\kappa} e^{2\gamma_\kappa} \left(\frac{dx^2}{x^2-1} + \frac{dy^2}{1-y^2} \right)$$
$$+k^2 e^{-2\psi_\kappa}(x^2-1)(1-y^2)d\phi^2 - e^{2\psi_\kappa}(dt - \omega_\kappa d\phi)^2, \tag{5.5}$$

where

$$e^{2\psi_\kappa} = \frac{p^2x^2 + q^2y^2 - 1}{(px+1)^2 + q^2y^2} \tag{5.6}$$
$$e^{2\gamma_\kappa} = \frac{p^2x^2 + q^2y^2 - 1}{p^2} \tag{5.7}$$
$$\omega_\kappa = \frac{2kq(1-y^2)(px+1)}{p(p^2x^2 + q^2y^2 - 1)}. \tag{5.8}$$

The boundary of the ergoregion of an SAV spacetime occurs at $g_{tt} = 0$, i.e. for Kerr when $e^{2\psi_K} = 0$. Also note that p and q are chosen such that $p^2 + q^2 = 1$, with p and q real constants and k a real constant. For convenience the choice $k = 1$ is often made [10].

5.3 Transformation between Prolate Spheroidal coordinates and Boyer-Lindquist coordinates

The transformation between the Boyer-Lindquist coordinates (t, r, θ, ϕ) and the prolate spheroidal coordinates (t, x, y, ϕ) [44, 56] is given by

$$r = M(px+1) \qquad\qquad y = \cos\theta \tag{5.9}$$

while choosing

$$p = \frac{\sqrt{M^2 - a^2}}{M} \qquad\qquad q = \frac{a}{M} \tag{5.10}$$

Comparing the coefficients of the dt^2 terms in the line elements of Eqs. (5.1) and (5.5) is the simplest way with which to verify this coordinate transform.

5.4 The Effective Kerr Potential

From Eq. (3.10) we have seen that the effective potential J for an SAV metric can be expressed in terms of two potentials G and V and the squares of the conjugate momenta, such that $J = (G - \mu^2)V = p_\rho^2 + p_z^2$.

It follows that the potential must be positive, since p_ρ and p_z must be real to have physical meaning. The region for which $J > 0$ is referred to as the *physical space* or the *allowed region* and describes the parameter space in which the orbits analysed can have a physical interpretation. Since the Kerr Hamiltonian is integrable it follows that the associated Hamilton-Jacobi equations for Kerr are separable. This separability can be demonstrated by showing that the effective Kerr potential is separable. In the next subsection I show how the Kerr potential separates when using the prolate spheroidal coordinates of Section 5.2.

5.4.1 Separating the effective Kerr potential (J)

To show that the effective Kerr potential is separable in prolate spheroidal coordinates (x, y), I start by computing $G = -g^{AB}p_A p_B$, where A and B run over t and ϕ.

From the line element

$$\begin{aligned} ds^2 = k^2 e^{-2\psi_K} e^{2\gamma_K} \left(\frac{dx^2}{x^2-1} + \frac{dy^2}{1-y^2} \right) \\ +k^2 e^{-2\psi_K}(x^2-1)(1-y^2)d\phi^2 - e^{2\psi_K}(dt - \omega_K d\phi)^2 \end{aligned} \tag{5.11}$$

it follows that

$$g_{AB} = \begin{bmatrix} -e^{2\psi_K} & \omega_K e^{2\psi_K} \\ \omega_K e^{2\psi_K} & k^2 e^{-2\psi_K}(x^2-1)(1-y^2) - \omega_K^2 e^{2\psi_K} \end{bmatrix}, \tag{5.12}$$

such that the inverse is equal to

$$g^{AB} = -\frac{1}{k^2(x^2-1)(1-y^2)} \begin{bmatrix} -e^{2\psi_K}\omega_K^2 + k^2 e^{-2\psi_K}(x^2-1)(1-y^2) & -e^{2\psi_K}\omega_K \\ -e^{2\psi_K}\omega_K & -e^{2\psi_K} \end{bmatrix} \tag{5.13}$$

and therefore, using the conserved quantities $p_t = -E$ and $p_\phi = L_z$,

$$\begin{aligned} G &= -g^{AB}p_A p_B \\ &= \frac{1}{k^2(x^2-1)(1-y^2)} \left[\left(-e^{2\psi_K}\omega_K^2 + \frac{k^2}{e^{2\psi_K}}(x^2-1)(1-y^2) \right) E^2 + 2e^{2\psi_K}\omega_K E L_z - e^{2\psi_K} L_z^2 \right]. \end{aligned} \tag{5.14}$$

By substituting Eq. (5.14) into Eq. (3.10) and setting $\mu = 1$, the effective potential becomes

$$J = \frac{1}{(x^2-1)(1-y^2)}\left[\left(-e^{2\gamma_K}\omega_K^2 + \frac{k^2 e^{2\gamma_K}}{e^{2\psi_K}^2}(x^2-1)(1-y^2)\right)E^2 + 2e^{2\gamma_K}\omega_K E L_z - e^{2\gamma_K}L_z^2\right] - \frac{k^2 e^{2\gamma_K}}{e^{2\psi_K}}. \tag{5.15}$$

Substituting Eqs. (5.6) – (5.8) into Eq. (5.15) and grouping the x and y terms gives

$$\begin{aligned} J &= (G-1)\,V \\ &= \frac{k^2\left(7E^2-1\right)}{p^2} + x\frac{k^2\left(4E^2-2\right)}{p} + x^2k^2\left(E^2-1\right) \\ &+ \frac{1}{x^2-1}\left(\frac{4k^2E^2 + 4kEL_zqp + L_z^2q^2p^2 + 4k^2E^2p^2}{p^4}\right) \\ &+ \frac{x}{x^2-1}\left(\frac{8k^2E^2 + 4kEL_zqp}{p^3}\right) + \frac{y^2k^2q^2}{p^2}\left(E^2-1\right) - \frac{L_z^2}{1-y^2}, \end{aligned} \tag{5.16}$$

such that the effective potential is separable in prolate spheroidal coordinates (x, y).

5.4.2 Physical Space Plots

The allowed physical space is the region for which $J > 0$ (from Eq. (3.10)). In Figure 5.2 regions for which the effective potential is positive are shown for different parameter values. To ensure that the squares of p and q sum to 1, I express them as $p = \cos\alpha$ and $q = \sin\alpha$. From Eq. (5.10) we see that, for the mass of the Kerr black hole set to $M = 1$, changing α to vary p and q amounts to varying the spin of the black hole, a. The panels of Figure 5.2 show how the shape of the physical space changes as the spin of the black hole is varied for a fixed energy and angular momentum. The value for α is changed from 0 to $\pi/2$, to ensure that the spin ranges from 0 to 1. Figure 5.2(a) has $\alpha = a = 0$, corresponding to a non-spinning black hole. As the spin increases, from 5.2(b) to 5.2(c), a small bounded area is pinched off from the inner region. Orbits that are born close to the inner region of the physical space that runs all the way to the event horizon where $\rho = 0$ are plunging orbits and will fall rapidly to the central object. However, geodesic orbits born in the pinched off region will be bounded by its physical space boundaries and will therefore not plunge to the black hole. In the bottom panels (Figure 5.2(d) to 5.2(f)) the two regions have merged again with increasing spin. The joined region will continue to grow radially outwards as a maximally spinning Kerr black hole ($a = 1$) is approached. Orbits starting out in the outer part of this joined region can still remain bound. In Chapter 6 we will investigate bound regions for the Manko-Novikov metric in the same style. The Kerr physical

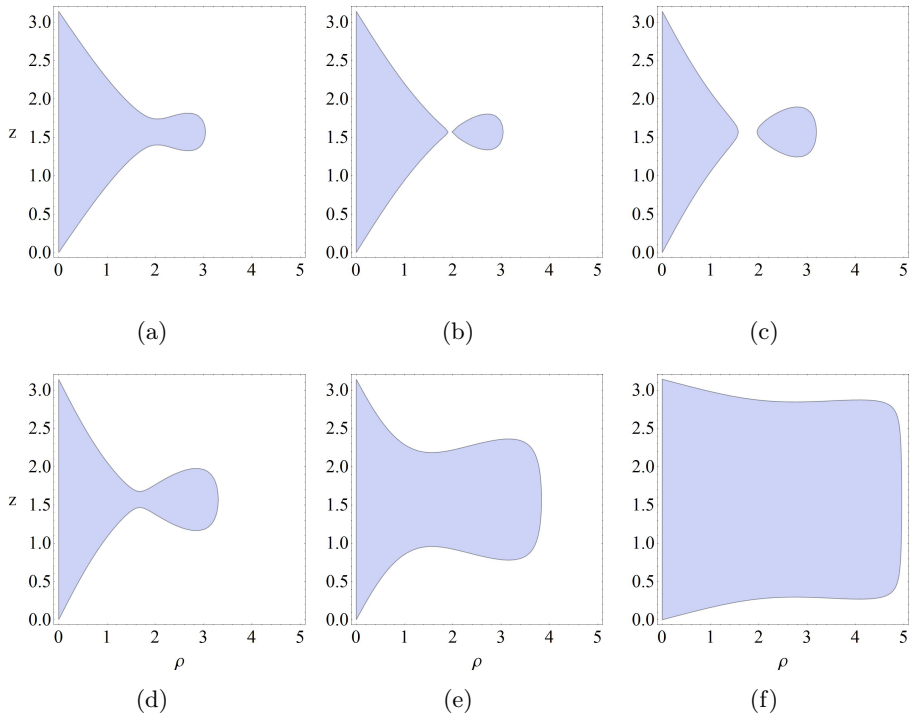

Figure 5.2: *(a)* **Physical space plot for** $E = 0.95$, $L_z = -3.5$, $\mu = M = k = 1$ **and** $\alpha = 0$, **where** $p = \cos\alpha$ **and** $q = \sin\alpha$ **was chosen, such that** $p^2 + q^2 = 1$ **as is required. This implies that** $q = a = 0$, **i.e. a non-spinning black hole.** *(b)* **Physical space plot for parameter values as before, but with** $\alpha = 0.1$ **(i.e. the spin** $a \approx 0.1$**). The outer region has pinched off to form a small bounded region, which lies roughly between** $\rho = 2$ **and** $\rho = 3$ **and is symmetric about the equatorial plane.** *(c)* **The value of** α **has been increased to** 0.3, **which implies a spin value of** $a \approx 0.3$, **causing the bounded outer region to move slightly outwards.** *(d)* **At a spin value of** $a \approx 0.39$ **(**$\alpha = 0.4$**) the two regions have joined again.** *(e)* **At** $\alpha = 0.8$ **the spin has increased to** $a \approx 0.72$ **and the physical space has increased significantly.** *(f)* **The physical space continues to grow outwards as the spin increases and will eventually become unbound at** $a = 1$, **a maximally spinning black hole.**

space is revisited in Appendix B where the Kerr limit of the Manko-Novikov metric is verified.

5.5 Poincaré Maps for Kerr

In Section 4.4 Poincaré maps were discussed as a valuable tool for investigating Hamiltonian flows and the integrability of Hamiltonian systems. In the case of the Kerr spacetime, after having introduced the constants of motion $p_t = -E$ and $p_\phi = L_z$, you are left with a system of two degrees of freedom and therefore a phase space of four dimensions (ρ, z, p_ρ, p_z) where ρ and z are the factor structure coordinates from Section 5.2. To draw a Poincaré map for this spacetime, I start by choosing a two dimensional slice in the phase space and study the successive intersections that the orbital trajectories make with this surface. For convenience's sake I chose to study the equatorial plane. That means setting $z = \pi/2$ (or $y = 0$). Figure 5.3(a)

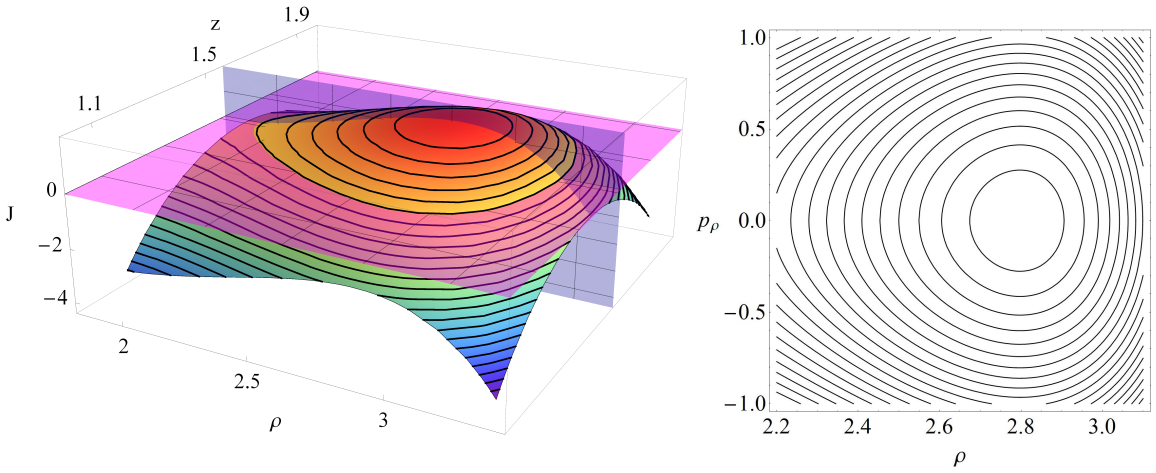

(a) (b)

Figure 5.3: ***(a)*** **The effective Kerr potential** $J(\rho, z)$ **for** $E = 0.95$, $L_z = -3.5$, $k = M = \mu = 1$, $p = \cos\alpha$ **and** $q = \sin\alpha$ **with** $\alpha = 0.3$ **– corresponding to the outer region of the top right panel of Figure 5.2. The horizontal (magenta) slice shows the line** $J = 0$ **to indicate the physical space is in the dome above this plane. The vertical (blue) slice shows the equatorial plane,** $z = \pi/2$**, the chosen surface of section for creating the Poincaré map on the right.** ***(b)*** **The Poincaré map for the Kerr spacetime with parameters given above. The map plots the** ρ **vs.** p_ρ **value for orbits piercing the equatorial plane. The closed curves are typical of a fully integrable system.**

shows a three dimensional plot of the effective potential associated with the pinched off region in Figure 5.2(c). In Figure 5.3(a) the horizontal (magenta) slice shows the surface $J = 0$, such that the orbits I am interested in lie in the dome above this plane. The vertical (blue) slice shows the chosen surface of section (namely the equatorial plane, $z = \pi/2$) through which I will study the orbital piercings.

Each time an orbit pierces the equatorial plane in a chosen direction, e.g. from below, a point of the Poincaré curve is generated. The plot uncovered by studying a family of orbits piercing the equatorial plane is the Poincaré Map. Dots that create a closed curve show that the corresponding orbit has an extra constant of motion. In the case of Kerr, which is integrable and has the Carter constant as a fourth constant of motion, we therefore expect closed curves for all initial values and no breaking of the tori. All the resonant periodic orbits are stable and do not form Birkhoff chains of island as was discussed in Section 4.5.

Consider the expression for the effective Kerr potential on the equatorial plane by setting $y = 0$ ($z = \pi/2$) in Eq. (5.16),

$$
\begin{aligned}
p_\rho^2 + p_z^2 = (G-\mu^2)V &= J(\rho, E, L_z, \mu^2) \\
&= \frac{k^2(7E^2-1)}{p^2} + x\frac{k^2(4E^2-2)}{p} + x^2k^2(E^2-1) \\
&+ \frac{1}{x^2-1}\left(\frac{4k^2E^2 + 4kEL_zqp + L_z^2q^2p^2 + 4k^2E^2p^2}{p^4}\right) \\
&+ \frac{x}{x^2-1}\left(\frac{8k^2E^2 + 4kEL_zqp}{p^3}\right) - L_z^2. \qquad (5.17)
\end{aligned}
$$

The Poincaré map I want to plot is the map of ρ vs. p_ρ, corresponding to the orbits piercing the equatorial plane from below. In the separable Kerr case we see that as a quick check, instead of evolving the equations of motion, we can just plot a contour map of

$$p_\rho^2 - J(\rho, E, L_z) = -p_z^2 \qquad (5.18)$$

where, for a chosen E, L_z and spin a (and values for μ, M and k), different values of p_z^2 will create different contours when plotting ρ against p_ρ , as is seen in Figure 5.3(b). In the case of Manko-Novikov the effective potential is *not* separable and, instead of making analytical contour plots as for Kerr, I will have to evolve the equations of motion numerically and interpolate the piercing points onto a chosen surface of section.

A Poincaré map for the Kerr spacetime is also shown in Appendix B. There it is obtained as a result of simplifying the Manko-Novikov spacetime to Kerr by dialling away the Manko-Novikov quadrupole moment deviation, i.e. by smoothing its *bumps* and then evaluating the equations of motion.

CHAPTER 6
Manko-Novikov Metric

The Manko-Novikov metric is an exact solution to the SAV field equations discussed in Chapter 3. This family of solutions was found in 1992 by Vladimir Manko and Igor Novikov. The Manko-Novikov metric is a concise analytical form metric that describes the vacuum exterior of any axisymmetric object with arbitrary mass multipole moments and a fixed spin [46, 16]. The Manko-Novikov metric is a deviation off Kerr in the sense that the multipole moments can be chosen in such a way that they agree with the Kerr multiple moments to a certain order and then deviate from the Kerr moments at a higher order. By switching off the deviation you recover Kerr.

As soon as a metric deviates from the Kerr multiple moments, the No-Hair multipole relations given by Eq. (2.2) no longer hold. Compact objects that differ from Kerr black holes with the addition of *bumps* in their higher order multipole moments have previously been termed bumpy black holes (see Chapter 1). The Manko-Novikov metric is therefore the metric with which I analyse the features of bumpy black holes.

To arrive at their solution, Manko and Novikov first constructed a non-linear superposition of the Kerr solution with an arbitrary static vacuum Weyl field [46]. The solution to the Ernst equation, given in Eq. (3.4), for such a construction has the form

$$\epsilon = e^{2\psi} A_- / A_+ \tag{6.1}$$

$$A_\mp := x(1+ab) + iy(b-a) \mp (1-ia)(1-ib) \tag{6.2}$$

where ψ is any solution to the Laplace equation $\Delta\psi = 0$, and a and b satisfy a set of first-order differential equations. (This a should not be confused with the a used to label the spin of the Kerr metric in Chapter 5.) In the case of the Manko-Novikov solution, ψ is set equal to the ordinary Weyl multipole moments. That means it has the form

$$\psi = \sum_{n=1}^{\infty} \alpha_n \psi_n = \sum_{n=1}^{\infty} \alpha_n r^{-n-1} P_n(xy/r), \tag{6.3}$$

$$\text{where} \qquad r \equiv (x^2 + y^2 - 1)^{1/2} \tag{6.4}$$

$$\text{and} \qquad \alpha_n = \text{constant}. \tag{6.5}$$

Each ψ_n satisfies the Laplace equation independently and P_n are the Legendre polynomials. These expressions are later given in Eq. (6.19). The solution obtained possesses an event horizon which has singularities only on the equator and is well behaved elsewhere.

In this thesis I will analyse a subclass of the solutions, for which the metric agrees with Kerr up until the mass quadrupole moment. This means setting $\alpha_n = 0$ for all $n \neq 2$ in Eq. (6.3). By varying a single parameter, α_2, the quadrupole moment is dialled away from the Kerr solution. Setting $\alpha_2 = 0$ along with a suitable choice of metric parameters, Kerr is recovered.

In this thesis I will focus on parameter sets which were analysed by both Gair et al. [22] and Lukes-Gerakopoulos et al. [45] in order to compare my results to theirs. Both these groups worked in Weyl coordinates (ρ_w, z_w), whereas my analysis is conducted in the factor structure coordinates (ρ, z) of Section 5.2. The transformation between these is straightforward and can be found in Appendix A.

6.1 Manko-Novikov Coefficients

As a member of the SAV metrics, the mentioned subclass of Manko-Novikov spacetimes (hence forth referred to as the Manko-Novikov metric) can be written in terms of the general SAV line element,

$$ds^2 = k^2 e^{-2\psi}[e^{2\gamma}(d\rho^2 + dz^2) + R^2 d\phi^2] - e^{2\psi}(dt - \omega d\phi)^2, \tag{6.6}$$

where again $x = \cosh\rho$ and $y = \cos z$ such that (x, y) are the prolate spheroidal coordinates and (ρ, z) factor structure coordinates. In the case of the Manko-Novikov metric the line element coefficients have the following expressions [22, 45, 8],

$$R = \left(x^2-1\right)^{1/2}\left(1-y^2\right)^{1/2} \tag{6.7}$$

$$e^{2\psi} = e^{2\tilde{\psi}}\left(\frac{A}{B}\right) \tag{6.8}$$

$$e^{2\gamma} = e^{2\tilde{\gamma}}\frac{A\left(x^2-y^2\right)}{\left(x^2-1\right)\left(1-\alpha^2\right)^2} \tag{6.9}$$

$$\tilde{\psi} = \alpha_2\frac{P_2}{r^3} \tag{6.10}$$

$$\tilde{\gamma} = \frac{1}{2}\ln\frac{x^2-1}{x^2-y^2} - \frac{1}{2}\left(\ln\left(\frac{a}{-\alpha}\right)+\ln\left(\frac{b}{\alpha}\right)\right) + \alpha_2^2\frac{9}{6}\frac{P_3^2-P_2^2}{r^6} \tag{6.11}$$

$$\omega = 2ke^{-2\tilde{\psi}}\frac{C}{A} - \frac{4k\alpha}{1-\alpha^2}, \tag{6.12}$$

where

$$A = \left(x^2-1\right)(1+ab)^2 - \left(1-y^2\right)(b-a)^2 \tag{6.13}$$

$$B = [x+1+(x-1)\,ab]^2 + [(1+y)\,a+(1-y)\,b]^2 \tag{6.14}$$

$$C = \left(x^2-1\right)(1+ab)\,[b-a-y\,(a+b)] + \left(1-y^2\right)(b-a)\,[1+ab+x\,(1-ab)]. \tag{6.15}$$

The above a and b are defined in terms of the logarithms

$$\ln\left(\frac{a}{-\alpha}\right) = -2\alpha_2[(x-y)\left(\frac{P_0}{r}+\frac{P_1}{r^2}+\frac{P_2}{r^3}\right)-1] \tag{6.16}$$

$$\ln\left(\frac{b}{\alpha}\right) = -2\alpha_2[(x+y)\left(\frac{P_0}{r}-\frac{P_1}{r^2}+\frac{P_2}{r^3}\right)-1], \tag{6.17}$$

$$\tag{6.18}$$

where the P_n are Legendre Polynomials defined recursively as

$$P_n\left(u\right) = \frac{1}{2^n n!}\left(\frac{d}{dz}\right)^n\left(z^2-1\right)^n \tag{6.19}$$

such that

$$P_0 = 1 \qquad P_1 = u \qquad P_2 = -\tfrac{1}{2}+\tfrac{3}{2}u^2 \qquad P_3 = \tfrac{u\left(5u^2-3\right)}{2} \tag{6.20}$$

$$\text{with} \qquad u = \tfrac{xy}{r} \qquad \text{and} \qquad r = \left(x^2+y^2-1\right)^{\frac{1}{2}}. \tag{6.21}$$

The parameters α, α_2 and k determine the multipole moments of the spacetime, with the first

few having the values

$$\begin{aligned} M_0 &= k\left(1+\alpha^2\right)/\left(1-\alpha^2\right) & S_0 &= 0 \\ M_1 &= 0 & S_1 &= -2\alpha k^2\left(1+\alpha^2\right)/\left(1-\alpha^2\right)^2 \\ M_2 &= -k^3[\alpha_2 + 4\alpha^2\left(1+\alpha^2\right)\left(1-\alpha^2\right)^{-3}] & S_2 &= 0 \\ M_3 &= 0 & S_3 &= 4\alpha k^4[\alpha_2 + 2\alpha^2\left(1+\alpha^2\right)\left(1-\alpha^2\right)^{-3}]/\left(1-\alpha^2\right). \end{aligned} \tag{6.22}$$

In order to coincide with Kerr at low order I choose the mass $M = M_0$ and the spin $S = S_1$. This requires that

$$k = M\tfrac{1-\alpha^2}{1+\alpha^2} \quad \text{and} \quad \alpha = \tfrac{-M+\sqrt{M^2-(S/M)^2}}{(S/M)}. \tag{6.23}$$

To investigate the effect of a quadrupole deviation from the Kerr value, define the dimensionless quadrupole deviation as $q = -(M_2 - M_2^{\text{Kerr}})/M^3$ where M_2^{Kerr} is as described in Section 2.2 and Eq. (2.2). In terms of α and k,

$$M_2^{\text{Kerr}} = -S^2/M = -\frac{4\alpha^2k^3(1+\alpha^2)}{(1-\alpha^2)^3}. \tag{6.24}$$

Substituting Eq. (6.24) into the expression of M_2 in Eq. (6.22) we note that α_2 quantifies the deviation off Kerr,

$$M_2 = -k^3[\alpha_2 + 4\alpha^2(1+\alpha^2)(1-\alpha^2)^{-3}] = -k^3\alpha_2 + M_2^{\text{Kerr}} \tag{6.25}$$

where

$$\alpha_2 = qM^3/k^3. \tag{6.26}$$

6.2 Metric Characteristics

Two conditions are pre-supposed for obtaining a solution that describes an astrophysical black hole - the spacetime must possess an event horizon and the spacetime must have no closed timelike curves outside of this horizon. Close timelike curves open up the possibility for traveling backwards in time, and are thus considered fundamentally unphysical. In Chapter 5 the Kerr metric was discussed as an example of an astrophysical spacetime. Before continuing my analysis of the dynamics of the Manko-Novikov metric, I look into these characteristics of the Manko-Novikov spacetime, and analyse how the quadrupole deviation parameter, q, impacts on them. Since the Manko-Novikov spacetime does not obey the No-Hair theorems, we expect it to break one or both of the above mentioned assumptions.

A spacetime is called *oblate* if its mass quadrupole moment M_2 is negative. From Eq. (6.24)

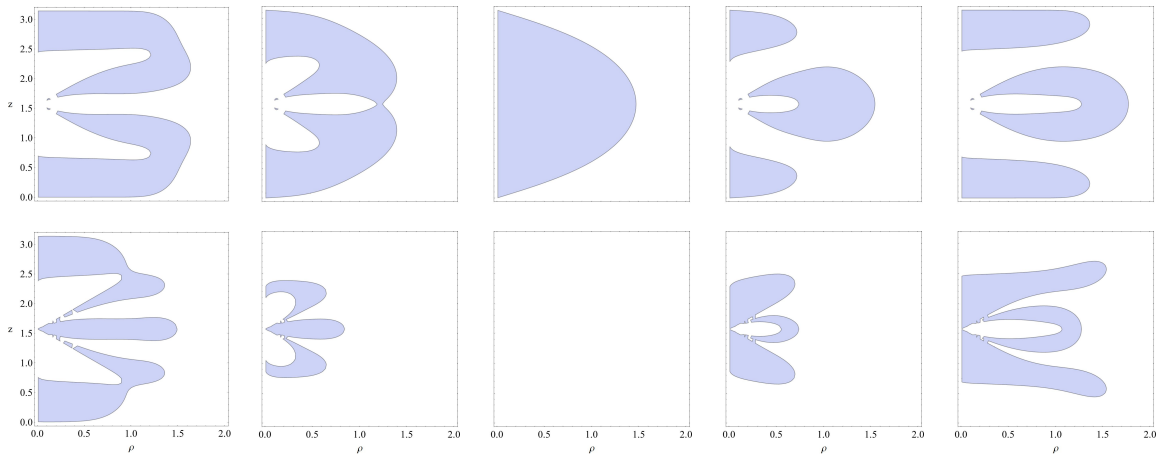

Figure 6.1: ***Top row*** **From left to right these panels show the regions for which the Manko-Novikov component $g_{tt} > 0$ with $g_{tt} = 0$ the ergoregion. For all the plots $E = 0.95$, $L_z = 3$ and $S = 0.9$. The first two panels in the row show the ergoregion for an extreme prolate perturbation ($q = -0.95$) and a less extreme prolate perturbation ($q = -0.1$), respectively. The middle panel shows the unperturbed spacetime where $q = 0$ and is therefore equivalent to the Kerr spacetime. The last two panels have an increasing oblate perturbation with $q = 0.1$ and $q = 0.95$ respectively.** ***Bottom row*** **From left to right these panels show regions in which the Manko-Novikov spacetime exhibit closed timelike curves (CTCs) as a function of increasing q. All the panels in the bottom row again have $E = 0.95$, $L_z = 3$ and $S = 0.9$. The first two panels have $q = -0.95$ and $q = -0.1$. The size of the region allowing for CTCs grows as the perturbation grows. For $q = 0$, corresponding to Kerr there is no region which admits CTCs. The next two panels have growing CTC regions with q-values $q = 0.1$ and $q = 0.95$.**

we see that Kerr is an oblate spacetime as can be expected for a rotating body. Figure 5.1 shows that in Boyer-Lindquist coordinates the Kerr spacetime can be represented as a sphere that has been flattened at the top and bottom. This is characteristic of an oblate perturbation. A *prolate* spacetime can be depicted as a sphere that has been squashed from the sides and is therefore elongated along the rotational axis. The type of perturbation (oblate or prolate) caused by the quadrupole moment deviation parameter q changes as q changes sign. In this thesis Kerr is taken as the reference metric, such that $q > 0$ represents an oblate perturbation off Kerr (making Kerr more oblate) and $q < 0$ represents a prolate perturbation (making Kerr less oblate).

The Manko-Novikov metric has a horizon at $\rho = 0$. This event horizon however is broken at the equatorial plane with a ring singularity at $z = \pi/2$ [46, 38]. Recall that the region between the event horizon and the static limit, beyond which no observer can remain stationary any longer, is called the ergoregion. For an SAV metric the static limit occurs at $g_{tt} = 0$ and the ergoregion at $g_{tt} > 0$. The top row panels of Figure 6.1 show the ergoregion for a Manko-Novikov compact object as a function of quadrupole deviation. Notice that a deviation from Kerr, whether prolate or oblate, causes the ergoregion to be much more complicated, exhibiting lobe structures, than

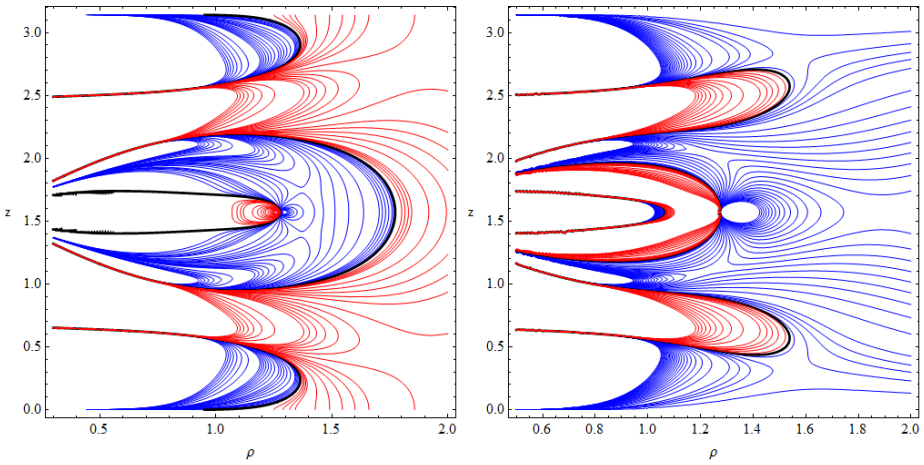

(a) (b)

Figure 6.2: ***(a)*** **Contour lines corresponding to g_{tt} of the Manko-Novikov spacetime with the same E, L_z and S parameter values as in Figure 6.1 and an oblate perturbation of $q = 0.95$. The physical ergoregion occurs for $g_{tt} > 0$.** ***(b)*** **Contour lines corresponding to $g_{\phi\phi}$ of the Manko-Novikov metric with the same parameter values as mentioned above. The regions for which $g_{\phi\phi} < 0$ indicate regions where closed timelike curves can occur. In both plots red indicates negative values and blue positive values. The black line shows where the metric component is equal to zero.**

for Kerr itself when $q = 0$. The shape of the ergoregion changes with respect to the type of perturbation. For prolate perturbations, the ergoregion has two main parts, one lying above the equatorial plane, the other below, whereas the oblate perturbed system has an ergoregion with three parts, one of which spans the equatorial plane and the others again above and below the equatorial plane respectively [22].

To investigate the presence of possible closed timelike curves in the spacetime we consider the conditions for which $g_{\phi\phi} < 0$ [22]. The bottom panels of Figure 6.1 show the Manko-Novikov regions that exhibit closed timelike curves as a function of different q values. Again these regions have lobe like structures and vary in shape depending on whether the perturbation is prolate or oblate. Notice that for $q = 0$ there are no closed timelike curves as one would expect for the astrophysical Kerr spacetime. One way to get rid of these closed timelike loops is by constructing an inner boundary and only considering the solutions exterior to that boundary. In this thesis all the orbital analysis will be conducted in the regions outside of these unphysical regions that would allow particles to move backwards in time. Figure 6.2 again shows the Manko-Novikov metric components g_{tt} and $g_{\phi\phi}$ for a constant spin and constant quadrupole deviation parameter. In this figure contour lines for constant metric component values are plotted, showing how the positive and negative regions for each are formed.

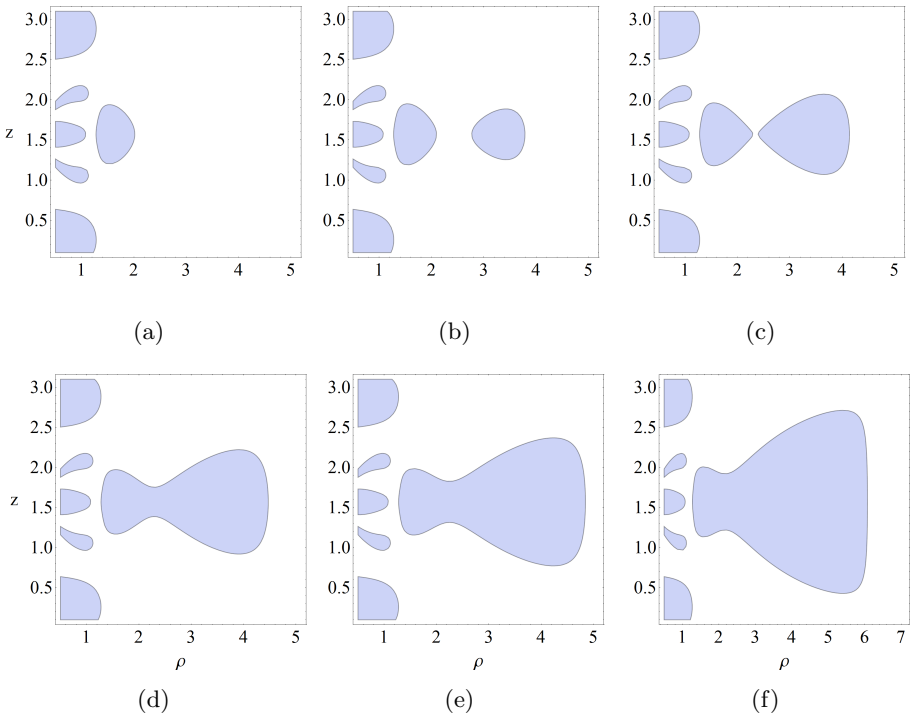

Figure 6.3: *(a)-(c)* **The energy increases from** $E = 0.93$ **to** $E = 0.94$ **to** $E = 0.95$**, all the while keeping angular momentum constant.** *(d)-(e)* **As the energy continues to rise taking on values** $E = 0.96$**,** $E = 0.97$ **and** $E = 0.99$ **the previously disjoint regions merge to form one bounded physical space. For** $E = 1.0$ **the merged region diverges to the right and does not close any longer. Note the symmetry of the physical space about the equatorial plane for which** $z = \pi/2 \approx 1.571$

6.3 Physical Space

To analyse orbital structure in Manko-Novikov spacetime I again investigate bound regions of the positive effective potential, $J(\rho, z)$, presented in Eq. (3.10), for a given parameter set, $(E, L_z, \mu, \alpha, \alpha_2)$. I set the rest mass of the probe (μ) and the mass of the black hole (M) equal to unity and choose to investigate a rapidly spinning black hole with $S = 0.9$ that has a high oblate quadrupole deviation measure, $q = 0.95$, such that $\alpha = 0.6268$ by Eq. (6.23) and $\alpha_2 = 11.4708$ by Eq. (6.26).

I now study the physical region as a function of changing energy E and azimuthal angular momentum L_z independently. Figure 6.3 shows how the bound regions of physical space change with a change in E. In Figure 6.4 similar effects can be obtained by varying L_z. In each of these figures the line $J = 0$ is plotted. Everything inside the bounded regions represent areas for which $J > 0$. The curves that don't close and lie at values for which roughly $\rho < 1.2$ represent plunging orbits. Probes in this region will rapidly fall onto the compact object at the centre. In Figure 6.3 we see that, as the energy increases from 6.3(a) to 6.3(c) a bounded outer region appears to the right of the bounded inner region. These two regions grow in size as the energy

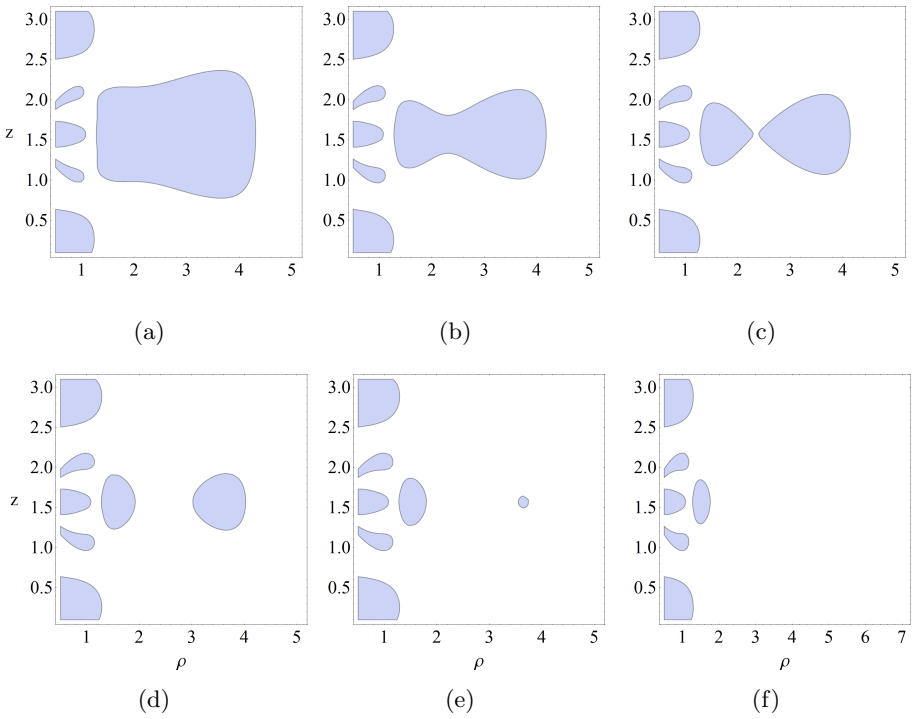

Figure 6.4: *(a)-(c)* **Keeping the energy constant at $E = 0.95$ the angular momentum is increased from $L_z = 2.4$ to $L_z = 2.9$ to again having $L_z = 3.0$ when the regions pinch off.** *(d)-(e)* **As the angular momentum increases even more, from $L_z = 3.2$ to $L_z = 3.4$ the outer region shrinks until for $L_z = 3.5$ it has disappeared entirely.**

increases. In panel 6.3(d) a further increase in energy has caused the inner and outer physical spaces to merge. In Figure 6.4 the physical space starts out as a merged space (panel 6.4(a)) and then slowly separates as L_z is increased. Finally for a high enough L_z (panel 6.4(f)) the outer region has disappeared.

An interesting parameter configuration from the above is the case for which $E = 0.95$ and $L_z = 3$. For these values, along with the chosen spin and quadrupole deviation, the physical space has split into two, exhibiting two bound regions with the inner boundaries relatively close to each other. This physical space was the focus of the studies by both Gair et al.[22] and Lukes-Gerakopoulos et al. [45]. I will start my analysis of the orbital structure within the Manko-Novikov spacetime by examining this configuration. Figure 6.5 shows the three dimensional structure of the effective potential J for these parameters. The lines on the 3D-figure have constant J values.

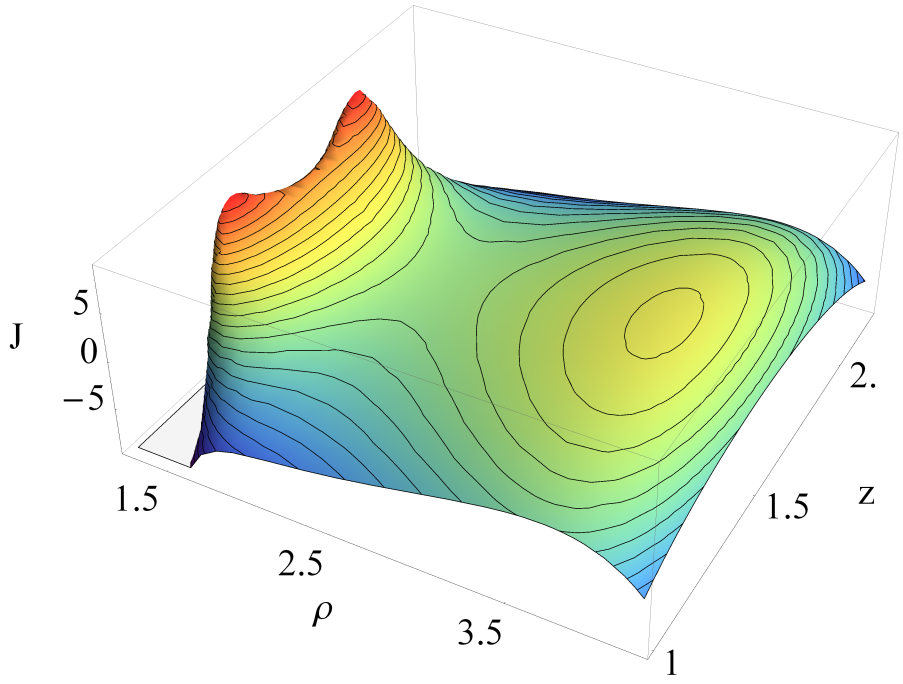

Figure 6.5: **The effective Manko-Novikov potential (J) as a function of coordinates ρ and z with $S = 0.9$, $q = 0.95$, $E = 0.95$ and $L_z = 3$. The black lines are lines of constant J-value. The region for which $J > 0$ represents the physical space for this set of parameters.**

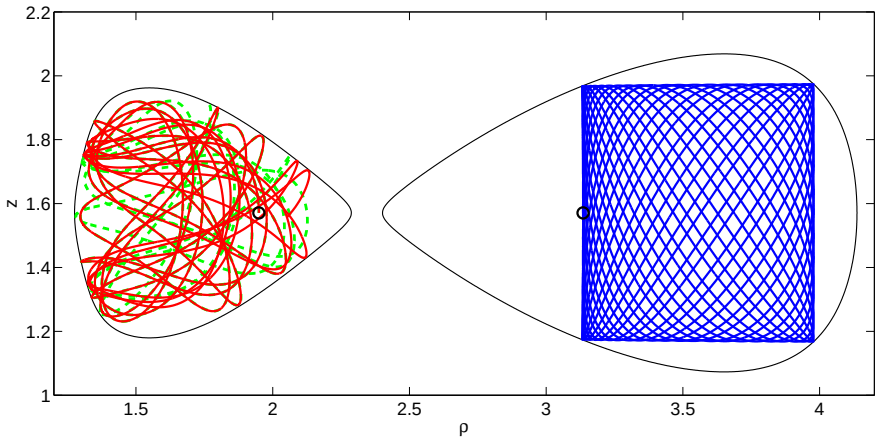

Figure 6.6: **Orbital trajectories in the physical space regions of the Manko-Novikov spacetime for a given parameter set. The chosen parameters are $E = 0.95$, $L_z = 3$, $S = 0.9$ ($\alpha = -0.6268$), $q = 0.95$ ($\alpha_2 = 11.4708$) and $k = \frac{1-\alpha^2}{1+\alpha^2}$. The black circles indicate the starting point of each orbit (on the equatorial plane, shooting out of the plane). In the outer region the orbits appears regular, whereas in the inner region the motion seems more chaotic. The green (dotted) and red (solid) lines in the inner region are orbits with initial conditions close to each other (the ρ coordinates lie within $\approx 5 \times 10^{-6}\%$ of each other). The trajectories for these orbits deviate significantly from each other. This is characteristic of chaotic motion.**

6.4 Orbital Motion

Since the Manko-Novikov spacetime described here is a perturbation off Kerr and Kerr is an integrable SAV metric exhibiting a fourth constant of motion (the Carter constant, refer to Chapter 5), it is of interest to explore the integrability of the Manko-Novikov metric and the possibility of finding an extra integral of motion in its case too. To start this exploration I examine the dynamics of a test particle within the allowed physical space region. This is done by solving the SAV equations of motion using the Manko-Novikov coefficients presented in Section 6.1. Recall from Eq. (3.11) that the equations of motion have the form $\dot{q}_i = p_i/V$ and $\dot{p}_i = \partial_{q_i} J/2V$, where the index i runs over the (factor structure) coordinates ρ and z. The potentials J and V are defined in Eq. (3.10) and the corresponding metric coefficients are calculated from Eqs. (6.8) to (6.21).

To plot the orbital trajectories in the ρ-z phase space slice, I find approximate solutions to the equations of motion by integrating over discretised proper time. For this purpose I make use of a numerical integrator that is based on an adaptive Runge-Kutta formula known as the Dormand-Prince pair [52].

To find approximate solutions to the equations of motion the integrator is presented with a set of initial conditions (ρ, z, p_ρ, p_z) that lie within the physical space. Only three of these are needed, since the fourth initial condition is automatically constrained by the other three initial conditions and the Hamiltonian constraint (refer to Eq. (3.10)). I make the simple choice of starting the orbit on the equatorial plane ($z = \pi/2$) and giving the particle initial momentum out of the equatorial plane only (i.e. $p_\rho = 0$ and $p_z = \sqrt{J(\rho, z)}$). I then plot the (ρ, z) trajectories as they evolve in proper time for various starting points in ρ. Figure 6.6 shows an example of orbital trajectories in the Manko-Novikov spacetime. At a first glance the orbits in the outer bounded region appear regular and typical of a system that exhibits integrability i.e. an extra constant of motion. The orbital structure of the inner region, closer to the compact object, however looks irregular and chaotic. Both Gair et al.[22] and Lukes-Gerakopoulos et al.[45] found this same basic correlation of regular motion with the outer region and chaotic motion with the inner region. They differ however in their more detailed analysis of the dynamics of the spacetime. I will further my investigation of the integrability of the spacetime by constructing Poincaré maps for the parameter sets associated with these two bounded regions.

6.5 Poincaré Maps

In the case of the Kerr metric I was able to derive an expression for the Poincaré map without evolving the equations of motion. This was possible since the separability of the effective potential

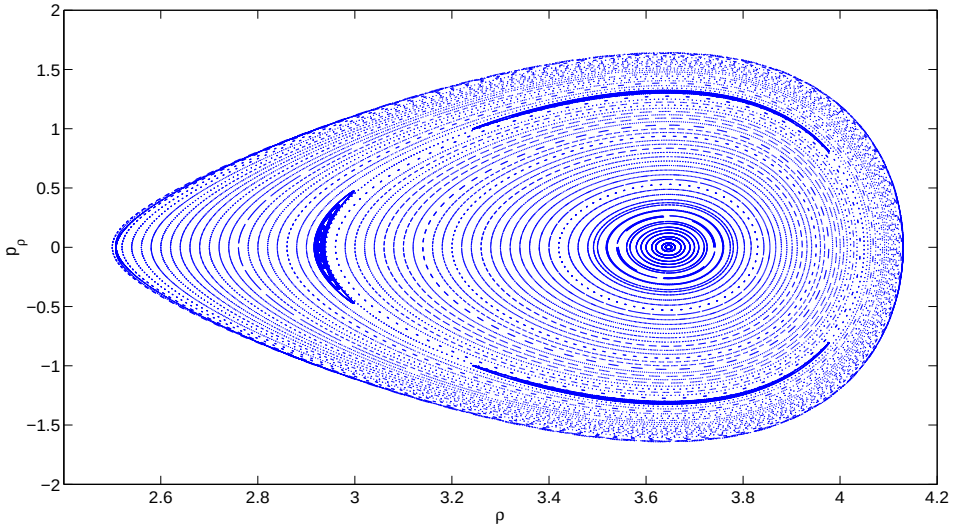

(a)

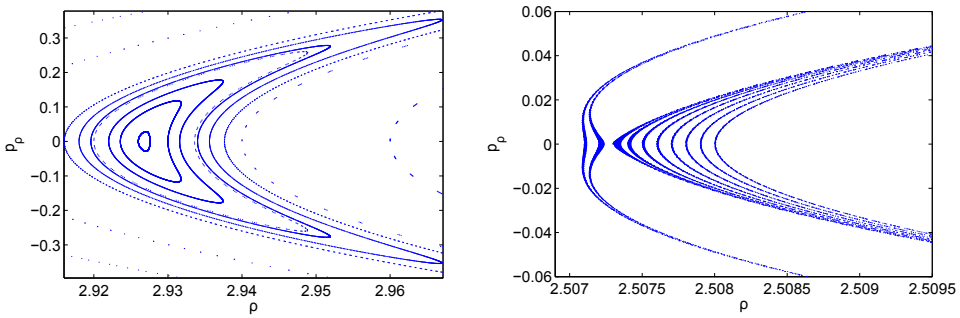

(b)

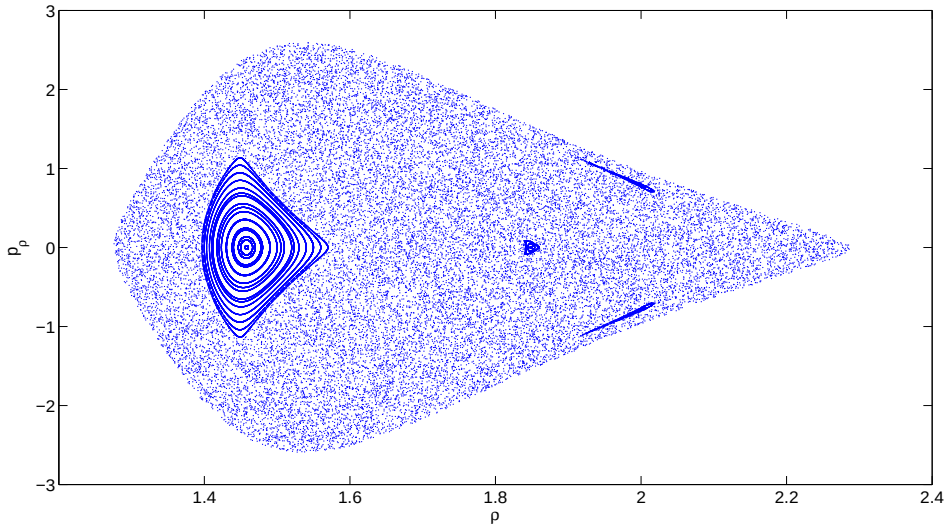

(c)

Figure 6.7: **Poincaré maps of the Manko-Novikov metric.** ***(a)*** **The outer region has mostly closed curves indicative of an additional constant of motion, however Birkhoff chains of islands appear which shows chaotic motion is present.** ***(b)*** **An O-point and X-point from the above map.** ***(c)*** **The map for the inner region is filled with dots characteristic of a chaotic system, but several closed curves appear too.**

made an analytic solution possible and a contour construction therefore straightforward. In the case of the Manko-Novikov metric the effective potential J is not separable. In order to obtain the Poincaré plot I have to find exact points of intersection of the orbital trajectories with a slice of section. I used a numerical integrator (suited for non-stiff functions) to approximate solutions to the equations of motion. In order to resolve the details of the structure of the Poincaré map, I evolved the equations for a million timesteps per orbit, with tolerances as follows: an initial step tolerance of 10^{-10}, a relative tolerance of 10^{-9} and an absolute tolerance of 10^{-12}[§].

Each orbit was started on the equatorial plane ($z = \pi/2$) with initial momentum out of the plane (i.e. $p_\rho = 0$ and $p_z = \sqrt{J(\rho, E, L_z, \alpha, \alpha_2, \mu)}$). To cover the physical space (for a given E, L_z, α, α_2 and μ) I advanced the ρ coordinate at times with increments as small as 0.002. After solving the equations of motion per set of initial conditions I interpolated the results to restrict myself to values in the equatorial plane. I chose to always evaluate the piercings of the $\rho - p_\rho$ slice made by trajectories that approached the surface from below and then passed upwards through it.

Figure 6.7(a) gives the Poincaré map for the outer region corresponding to Figure 6.6 for which $E = 0.95$, $L_z = 3$, $S = 0.9$ and $q = 0.95$. The Poincaré surface of section for this region exhibits mostly closed curves, indicative of an extra invariant quantity. This structure matches what both [22] and [45] found. However, fine combing the allowed physical space region we see that some of the closed curves are broken up and Birkhoff chains of islands surrounding the elliptical fixed points (as described in Section 4.5) can be made out. These islands were not found by [22] who did a too coarse overview of the parameter space. The Poincaré map they plotted had only closed curves in the outer region and therefore prompted them to speculate about the existence of a possible fourth constant of motion, in the same way that Kerr is associated with the Carter constant. The Birkhoff chains of island were however noted by [45].

Studying Figure 6.7(a) we see that two chains of islands can be made out in the outer region. The one island chain has a multiplicity of 3, meaning the invariant curve has split up to form 3 islands, i.e. 3 O-points and 3 X-points. The other island chain seen in Figure 6.7(a) has multiplicity 2. These islands are especially thin and hard to pick up in this surface of section. By choosing different initial conditions a Poincaré map can be generated that shows an island chain with multiplicity 2 more clearly. The existence of these two types of chains of islands proves that the system is non-integrable and the regular motion broken [45]. Some particular

[§]The tolerances adapt the time step size of the integrator. The initial tolerance provides an upper bound on the size of the first step and sets the scale of the problem. The relative tolerance provides the largest acceptable error relative to the size of each solution component during each time step. The absolute tolerance provides the largest acceptable error as solutions approach zero, i.e. it provides a measure of the smallest possible solution. If either the specified relative or absolute error is exceeded the time step size is reduced.

integrable systems with *one type* of island of stability do exist, however as soon as a system has more than one type of island it cannot be integrable any longer [17, 16].

The two panels of Figure 6.7(b) zoom in on an O-point and X-point, respectively, of Figure 6.7(a). The O-point shown corresponds to the islands of multiplicity 3, whereas the X-point corresponds to the 2-chain island. The dark regions left and right of the X-point are made up of single dots and represent the chaotic motion associated with X-points as was discussed in Section 4.5.

In the next section we will see that an easier way to find these chains of islands than scanning the parameter space carefully is by means of the *rotation number*. We expect the islands of stability to be associated with resonant orbits i.e. with rational frequency ratios as was shown in Figure 4.5. Figure 6.7(c) gives the Poincaré map of the inner region shown in Figure 6.6. As expected form the orbital plots, the biggest part of this Poincaré map is made up of piercings covering the space in its entirety and not forming any closed curves. What is unexpected however is the regular looking islands seen within this Poincaré map. A single multiplicity island lying between ρ-values 1.4 and 1.57 is found as well as a 3-chain island around $\rho \approx 1.85$ which is harder to discern. These islands of stability were not found by [22], but were picked up by [45]. The orbital motion corresponding to the multiplicity-3 islands in the outer region (Figure 6.7(a)) as well as the orbits of the main island in the inner region (Figure 6.7(c)) are shown in Figure 6.8. We see in Figure 6.8(a) that the orbits are tri-periodic, travelling from island to island. Figure 6.8(b) shows that the orbits in the main island of the inner region are contained and ordered as is expected form invariant curves in a Poincaré map. The structure of the orbits is however much more complicated when comparing them to the orbital trajectories of the outer region shown in Figure 6.6 (in blue).

6.6 Rotation Curves and Resonances

The detailed Poincaré map in the previous section exhibited the typical Birkhoff chains of islands (or islands of stability) that are associated with the breakdown of resonant tori in a nearly integrable system. In this section I set out to calculate the rotation curve for the Poincaré map to confirm that the islands are indeed associated with rational fraction values of the ratio of the characteristic frequencies of the system.

After having evolved the equations of motion and interpolating such that I am only considering points in the equatorial plane, I use these solutions to set up vectors that successively connect each point with the centre of the Poincaré map, as was done in Figure 4.4. The centre point value is calculated by finding the local maximum of the effective potential which corresponds to

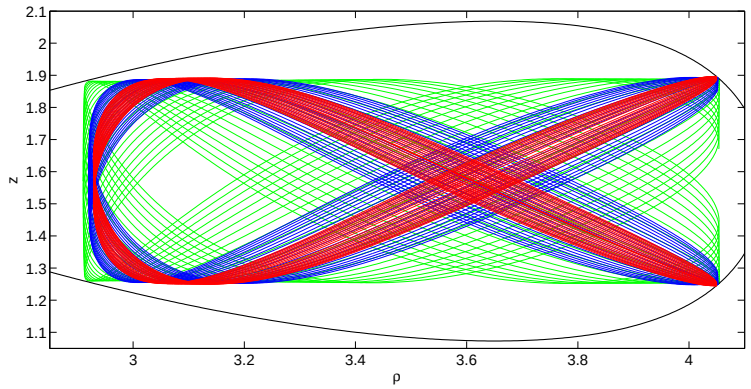

(a)

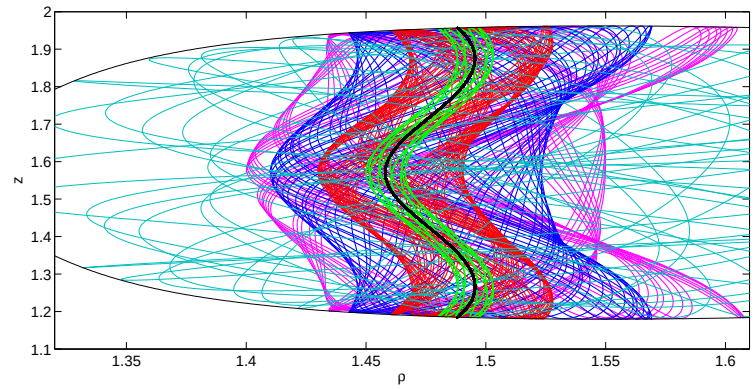

(b)

Figure 6.8: ***(a)*** **The trajectories of two orbits that corresponds to the multiplicity 3 islands found in Figure 6.7(a). Their starting points are $\rho = 2.92$ (blue) and $\rho = 2.93$ (red). Notice that they have a turning point within the physical space, whereas the green orbit that lies just outside of the islands ($\rho = 2.91$) has all its turning points on the boundaries of the physical space.** ***(b)*** **Orbits from the inner region of the physical space which corresponds to the main island in Figure 6.7(c). Their respective radial starting points are $\rho = 1.4$ (magenta), 1.41 (blue), 1.43 (red) and 1.45 (green). The single black line corresponds to the fixed point (centre point of the Poincaré map) and has $\rho \approx 1.458$. The orbit in the background is a chaotic orbit from the region outside of the main island. All the orbits in (a) and (b) were launched from the equatorial plane ($z = \pi/2$) and out of the plane ($p_\rho = 0$).**

the fixed point to a high order of accuracy. Refer to Figure 6.5 to see this correspondence.

Averaging over a sufficient number of calculated angles and expressing this average as a fraction of a circle (refer to Eq. (4.8)) gives the rotation number for a given orbit, i.e. for a given closed curve on the Poincaré map. I plot these values as a function of the orbit's leftmost ρ value which is the initial ρ value. This can be translated to a distance from the centre point as well.

The rotation curve for the Poincaré map in Figure 6.7(a) (i.e. the outer region) is shown in Figure 6.9(a). The plot shows that the rotation curve increases monotonically and is mostly smooth. However, as expected, there is a plateau in the curve where the rotation number equals

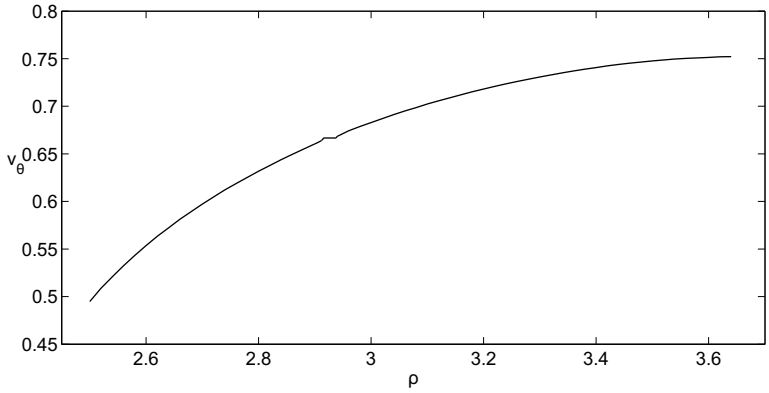

(a)

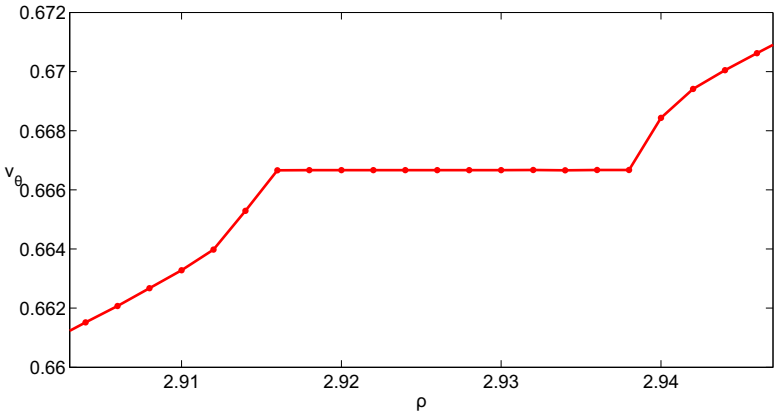

(b)

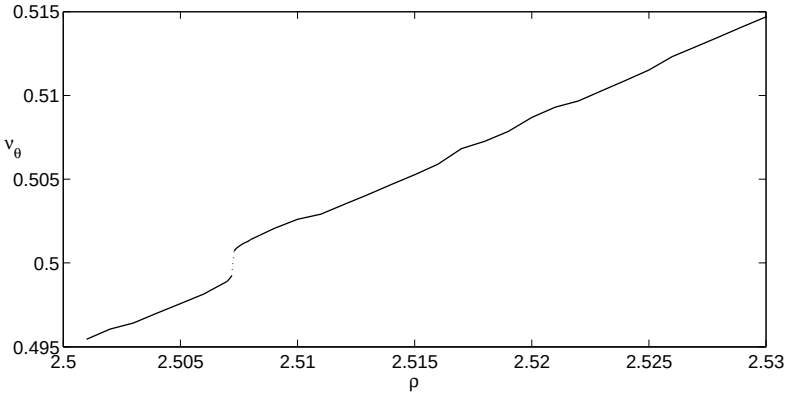

(c)

Figure 6.9: *(a)* **Rotation curve for the Manko-Novikov metric with $E = 0.95$ and $L_z = 3$ and spin and quadrupole deviation as before. The rotation curve shows a plateau at the rational number $2/3$ corresponding to the multiplicity-3 islands of stability present in the Poincaré map of Figure 6.7(a).** *(b)* **An enlargement of the $2/3$-plateau.** *(c)* **The rotation number for the X-point associated with the $1/2$ resonance in Figure 6.7(a) is undefined. This is seen as an inflection point at $\nu_\theta = 1/2$ on the rotation curve. Note that the ρ-values on all the plots correspond to the initial ρ-value of an equatorial orbit.**

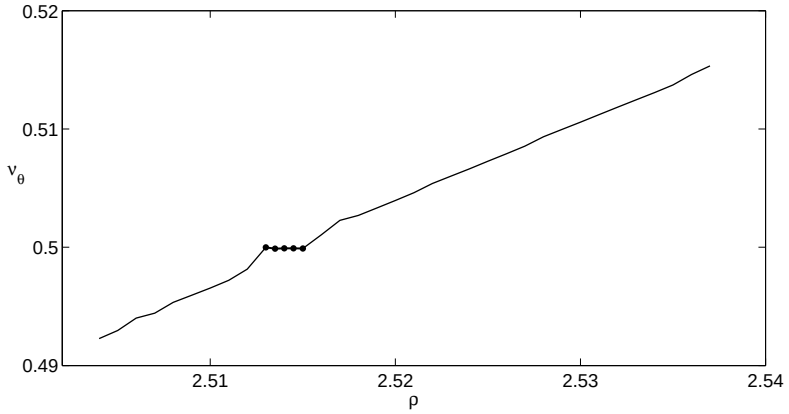

Figure 6.10: **The rotation curve for a system with initial conditions along the line $p_\rho = 0.1$ shows the $1/2$-plateau that was previously not seen in Figure 6.9. For this different set of starting points the rotation number remains equal to $1/2$ for all the orbits with initial conditions within the associated island of stability.**

a rational fraction value such as $2/3$. The rotation number remains equal to this value over a small range in ρ as can be seen more clearly in Figure 6.9(b). Looking back at the Poincaré map in Figure 6.7(a) we see that these ρ's correspond to the Birkhoff chains of islands of multiplicity 3. Figure 6.7(b) shows an X-point in the equatorial plane for $\rho \approx 2.5073$. Recall from Section 4.7 that the rotation number associated with an X-point is undefined and therefore shows up as an inflection point in the rotation curve. This inflection point associated with the $1/2$ resonance is visible in Figure 6.9(c).

To see the plateau associated with the $1/2$ resonance I have to change the initial conditions of the orbits such that the X-point itself is not a starting condition. By choosing a different initial momentum ($p_\rho = 0.1$ instead of $p_\rho = 0$) the plateau in the rotation curve can be found. This $1/2$ resonance is shown in Figure 6.10.

6.7 Observational Signatures

6.7.1 Quadrupole deviation

The plateaus seen in the rotation curves associated with orbital motion in the Manko-Novikov metric can in principle serve as an observational signature for a non-Kerr central compact object. The magnitude of the plateau scales with the size of the islands of stability and hence with the magnitude of the deviation parameter q. In Figure 6.11 I show two Poincaré maps and the corresponding rotation curves for a quadrupole deviation parameter of $q = 0.5$ and 0.2 respectively. The orbital constants of motion are as before. Comparing the Poincaré map in Figure 6.11(a) with the Poincaré map in Figure 6.7(a) we see that, as q changes from 0.95

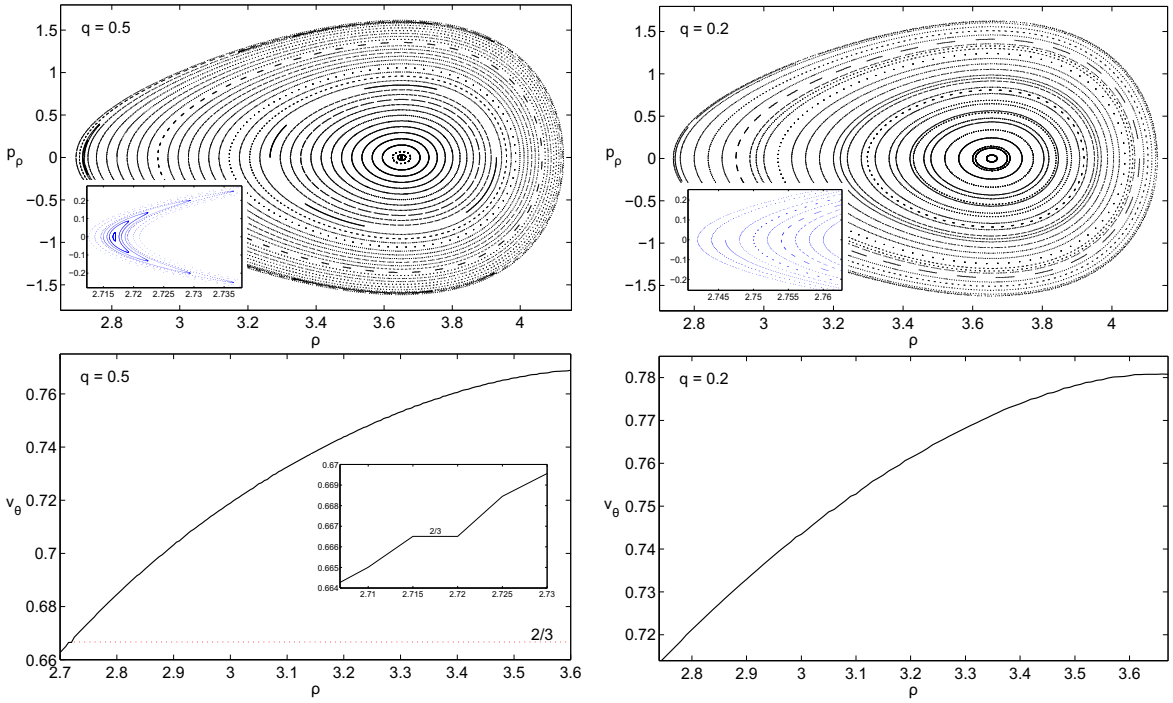

Figure 6.11: **Changing the quadrupole deviation parameter. The panels in *(a)* have a deviation measure of $q = 0.5$, this is lowered to $q = 0.2$ in *(b)*. For $q = 0.5$ a Birkhoff chain of islands appears close to the inner boundary of the physical spaces. The existence of the island of stability shows up as a $2/3$-plateau in the corresponding rotation curve. For $q = 0.2$ no islands of stability are seen in the physical space and the rotation curve shows no real plateaus. Thus, the smaller the deviation from Kerr, the less likely we are to see a significant difference between the Kerr and the Manko-Novikov metric.**

to $q = 0.5$, the island of stability with multiplicity 3 remains visible, but has moved closer in (i.e. closer to the compact object). The rotation curve corresponding to this value of $q = 0.5$ exhibits a plateau for $\nu_\theta = 2/3$. This plateau is roughly 4 times smaller than the $2/3$ plateau seen when $q = 0.95$. In Figure 6.11(b) the q value has been shrunk even further to $q = 0.2$. For this value of q my numerical technique no longer picks up any island of stability in the Poincaré map. Instead it shows a periodic orbit where an island of stability was anticipated. Also in the rotation curve there is no proper plateau. For such small deviations from Kerr it will therefore be increasingly difficult to measure the observational differences between an EMRI event involving a Manko-Novikov compact object and an EMRI event involving a conventional Kerr black hole.

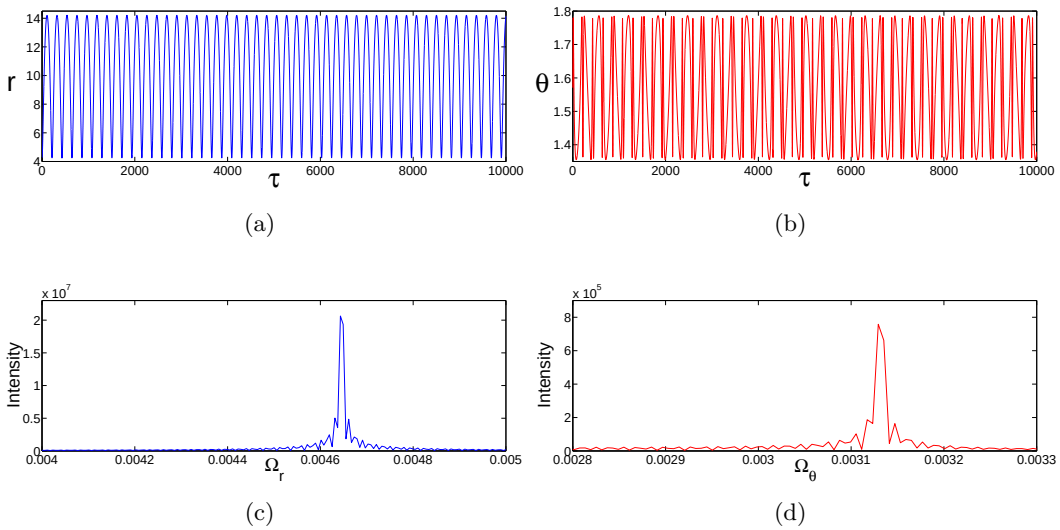

Figure 6.12: ***T*he Radial *(a)* and polar *(b)* oscillations plotted as a function of proper time. The chosen orbit has initial conditions on the equatorial plane, with momentum out of the plane ($p_\rho = 0$) and starting position $\rho = 2.7$. The geodesic parameters have values $E = 0.95$, $L_z = 3$, $S = 0.9$, $q = 0.95$ and $\mu = 1$, $M = 1$ as before. In panels *(c)* and *(d)* the periodicity of the radial and polar coordinates are clear from the prominent peaks (Ω_r and Ω_θ) in each of the corresponding Fourier spectra.**

6.7.2 Coordinate Frequencies and Fourier Transforms

The Poincaré maps and corresponding rotation curves have been useful to investigate the integrability of the Manko-Novikov metric by indicating whether and where islands of stability associated with non-integrable systems occur. The plateaus in the rotation curves have been considered as possible candidates by which to distinguish non-Kerr black holes from Kerr black holes. However, once we are able to detect the gravitational waves coming off an EMRI event, it will be the oscillations and corresponding Fourier spectra of the system frequencies that we observe [45]. In this section I further my investigation of the relationship between the calculated rotation number and the observed Fourier spectra that we expect to construct from observational measurements.

Figures 6.12(a) and 6.12(b) show the radial and polar oscillations for a given orbit in the Manko-Novikov space. These were achieved by evolving the equations of motion for 10^5 time steps of constant size $dt = 0.01$. The constant time steps ensure that the renormalisation of the frequency axis to produce Fourier spectra is straightforward. For the purpose of this investigation I have transformed back to Boyer-Lindquist coordinates using Eq. (5.9). The motivation for this is that the Boyer-Lindquist (r, θ) have a more clear physical interpretation than the factor structure coordinates (ρ, z) in which the Manko-Novikov metric was presented. In the Boyer-Lindquist coordinates the Fourier spectrum of the radial frequency also has higher intensity peaks

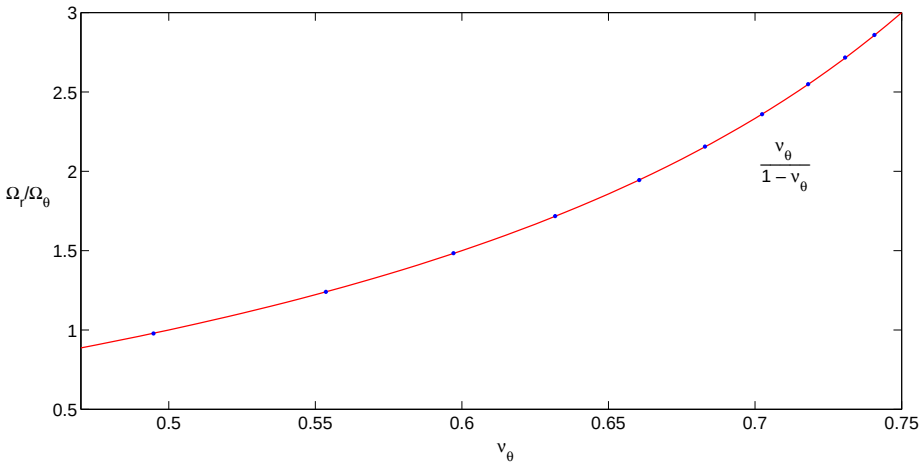

Figure 6.13: **The ratio of the prominent frequencies obtained from Fourier spectra plotted as a function of the orbital rotation number. The calculated orbital data (blue dots) are fitted with the function $\nu_\theta/(1-\nu_\theta)$ (red line). The orbital parameters are $(E, L_z, S, q) = (0.95, 3, 0.9, 0.95)$ with initial conditions on the equatorial plane and momenta out of the equatorial plane ($p_\rho = 0$).**

which makes it more suited for determining the characteristic frequency of the orbits [45]. (Note that, since $y = \cos z$ in factor structure coordinates and $y = \cos\theta$ from Eq. (5.9), it follows that $z = \theta$.)

The Fourier spectra of the orbital oscillations shown in Figure 6.12(a) and 6.12(b) are presented in Figure 6.12(c) and 6.12(d). These were produced through fast Fourier transforms of the oscillatory data. Each Fourier spectrum shows the most prominent peak associated with the radial and polar oscillations independently. The frequencies associated with these peaks are labelled Ω_r and Ω_θ.

In Figure 6.13 I plot the ratio of the frequencies associated with the most prominent Fourier peaks (Ω_r/Ω_θ) as a function of the orbital rotation number. The following empirical relationship is obtained from Figure 6.13

$$\frac{\Omega_\rho}{\Omega_z} = \frac{\nu_\theta}{1-\nu_\theta}. \tag{6.27}$$

A possible explanation for this relationship is that we expect the frequency value associated with the highest peak in the Fourier spectrum to be equal to a multiple of the fundamental frequencies (ω_i) of the system, i.e.

$$\Omega_k = \sum_i a_i^k \omega_i \tag{6.28}$$

with a_i^k's integers [45]. The ratio of frequencies associated with the most intense peaks (which are not harmonically related to each other) can therefore be expressed in terms of the rotation

number such that

$$\frac{\Omega_\rho}{\Omega_z} = \frac{a_1\omega_\rho + a_2\omega_z}{b_1\omega_\rho + b_2\omega_z} = \frac{\bar{a_1}\nu_\theta + \bar{a_2}}{\bar{b_1}\nu_\theta + \bar{b_2}} \tag{6.29}$$

where the definition of Eq. (4.9) was used and a_1, a_2, b_1 and b_2 as well as the barred quantities are integers. The empirical relationship found in Eq. (6.13) suggests that in this case $\bar{a_1} = 1$, $\bar{a_2} = 0$, $\bar{b_1} = -1$ and $\bar{b_2} = 1$.

As an example consider the Fourier spectra of the orbit which has the starting position $(\rho, z) = (2.7, \pi/2)$ as depicted in Figure 6.12(c) and 6.12(d). By introducing a Gaussian curve fit to the prominent peaks of the Fourier spectra, I find that $\Omega_r = \Omega_\rho \approx 4.646 \times 10^{-3}$ and $\Omega_\theta = \Omega_z \approx 3.132 \times 10^{-3}$. It follows that $\Omega_\rho/\Omega_z \approx 1.48$. The rotation number corresponding to this orbit with starting point $\rho = 2.7$ is $\nu_\theta \approx 0.5971$, as can roughly be seen from Figure 6.9(a). From these values we see that the empirical relationship of Eq. (6.27) holds, since $\nu_\theta/(1-\nu_\theta) = 0.5971/(1-0.5971) \approx 1.48$

For a resonant orbit with $\nu_\theta = 2/3$, I find that $\Omega_\rho/\Omega_z \approx 4.705 \times 10^{-3}/2.35 \times 10^{-3} \approx 2/1$, so that the ratio of characteristic frequencies is a rational fraction as was expected.

These calculations aim to illustrate the relationship that exists between the observable outputs, namely the Fourier spectra obtained from the detected gravitational waves, and the rotation curves constructed from a theoretical analysis of the relevant Hamiltonian system.

CHAPTER 7
Investigating Orbital Behaviour in a Non-convex Effective Potential

In Chapter 6 I investigated the Manko-Novikov spacetime's integrability by means of orbital plots, Poincaré maps and rotation curves. The analysis was done for a given set of parameters ($E = 0.95$, $L_z = 3$, $q = 0.95$ and $S = 0.9$) for which the physical space separates into two parts, namely an outer region that contains mostly regular orbits and an inner region that contains mostly chaotic orbits. Thorough investigation of the outer region showed that, although at first it appears regular, at resonance values the closed curves of the Poincaré map break up to form islands of stability. The spacetime was thus found to be non-integrable and will therefore not exhibit an extra constant of motion.

Previously in Figures 6.3 and 6.4 we have seen that changing the values of the orbital energy and angular momentum changes the shape of the allowed physical space. For some combinations of energy and angular momentum the inner and outer regions of the physical space will fuse. In this chapter I investigate the orbital dynamics within such a merged or non-convex[¶] physical space.

By increasing the energy from $E = 0.95$ to $E = 0.951$ a narrow neck connecting the outer and inner regions is created as shown in Figure 7.1(a). I investigate this physical space by studying orbital trajectories with initial conditions on the equatorial plane and varying radial launch points. Orbits starting in the inner region and in the parts of the neck facing the inner region spend most of their time in the chaotic regime, but will traverse the neck on occasion. After escaping through the neck to the outer region the particle exhibits regular motion there before crossing back to the inner region. Most orbits with initial conditions in the outer region or the regions of the neck facing the outer region do not traverse the neck. Instead they exhibit the same regular type motion as was discussed in Chapter 6 for the outer region. If however an orbit in the outer region starts out very close to the boundary of the outer region's allowed physical space, these orbits too will traverse the neck, spending time in both (previously disjoint) regions.

Figure 7.1 shows the orbital structure for different equatorial initial conditions in physical spaces with necks of changing width. A decrease in angular momentum L_z or, alternatively an

[¶]A region in $\mathbb{R}^n$ is convex if every pair of points within the object can be joined with a straight line segment that lies within the object. If the inner and outer region of the Manko-Novikov physical space is joined by a neck it forms a dumbbell shaped object which is non-convex.

increase in energy E, causes the neck to widen. As the neck widens the interactions between the two regions increase. Orbits in the outer most regions however mainly remain bound to their side of the physical space (unless the orbits start out close to the boundaries of the outer region). Two of the orbital trajectories shown in Figure 7.1(c) are presented again in Figure 7.3 - this time with the contour lines of the associated effective potential superimposed on the figure. The contour plot of the potential shows two spikes, symmetric about the equatorial plane. Orbits that visit these plunging regions of the gravitational potential tend to cluster here for long times before moving off again to the outer region. To gain further insight into the regularity of the orbits in a merged physical space, I consider the Poincaré maps corresponding to the various situations.

The Poincaré maps with increasing neck widths are presented in Figure 7.2. From 7.2(a) to 7.2(c) there is a clear increase in chaotic orbits around the main island of the outer region. This corresponds to observing orbits that start out between the last KAM curve and the boundary of the outer region. These orbits occasionally travel to the inner region and back again.

The phenomenon by which chaotic layers tend to keep alongside the regular curves has been termed *stickiness* by Contopoulos [14, 45]. As long as the chaotic layer remains close to the invariant curve it will exhibit two characteristic frequencies like conventional regular orbits. When the layer releases itself from the invariant curve to traverse the neck, the characteristic frequencies disappear, and the spectrum becomes chaotic [45]. It has been suggested that this emergence and disappearance of two characteristic frequencies could be a tell-tale sign of a non-Kerr spacetime, i.e. a bumpy black hole spacetime. However this phenomenon may in practice be difficult to measure with gravitational wave detectors [45]. Also note from the Poincaré maps that the main island of stability which existed in the inner region before becomes smaller and disappears as the neck widens. There is therefore a general increase in chaos as the neck widens and the two previously disjoint regions merge.

Clearly the occurrences of resonances and the associated chaotic region have a strong dependence on the shape of the gravitational potential. The effective potential is parameterised by characteristics of the spacetime that describes the compact object around which the low mass probe orbits. These are the intrinsic spin S and the quadrupole moment deviation q. Additionally the gravitational potential is shaped by the orbital constants of motion, namely the energy E and angular momentum L_z of the orbiting probe. In Figures 7.1 and 7.2 the S and q remained constant while E and L_z were changed only slightly. Cleary such an analysis investigates a very specific situation and not the complete accessible parameter space. One way of aiming to characterise the effective potential and its resonances completely is to find analytic expressions for

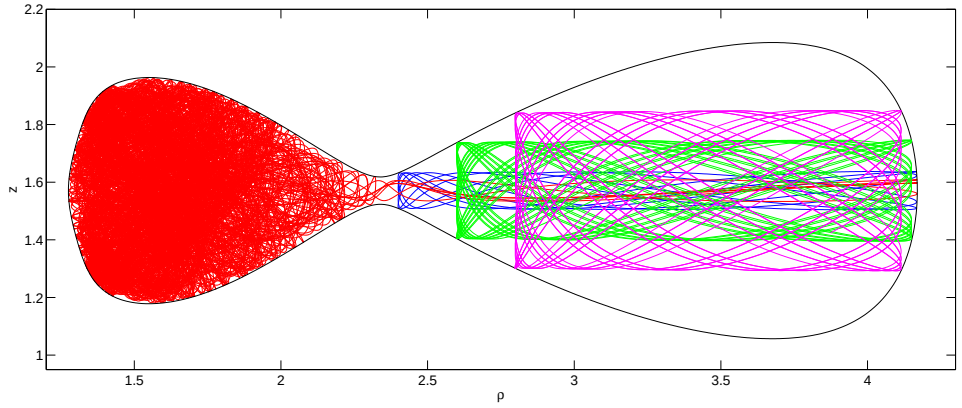

(a)

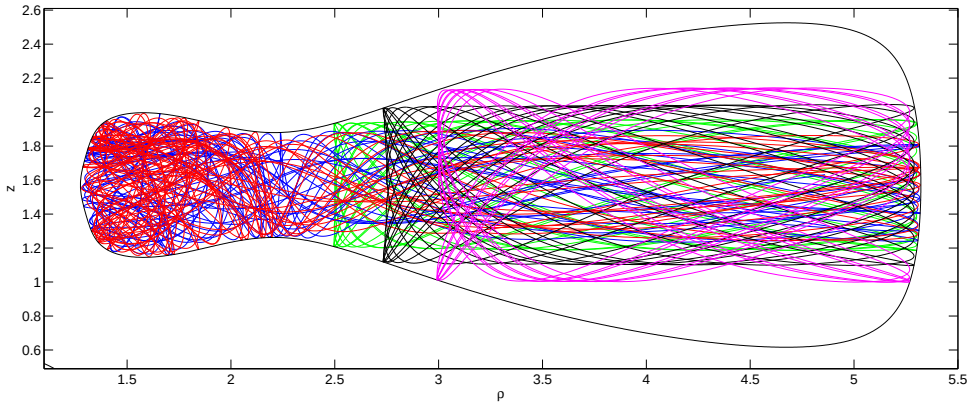

(b)

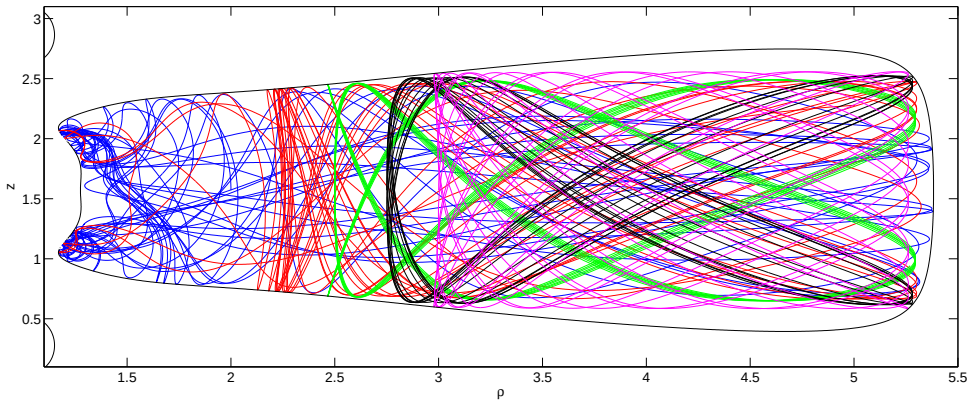

(c)

Figure 7.1: **The neck connecting the inner and outer regions widens as the energy and angular momentum is changed. From these orbital structure plots we see that orbits starting in the inner region can traverse the neck and follow a temporary, more organised trajectory in the outer region before returning to the inside. Orbits starting in the outer region or the parts of the neck that face the outer region tend to stay on the outside and exhibit regular structure. From *(a)* to *(c)* the corresponding parameters are** $(E = 0.951, L_z = 3)$**,** $(E = 0.98, L_z = 3)$ **and** $(E = 0.98, L_z = 2)$**.**

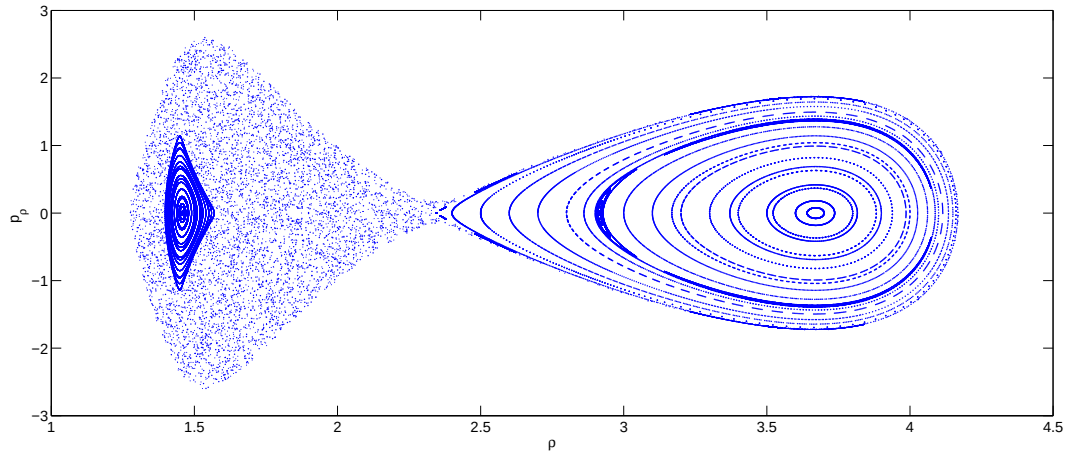

(a)

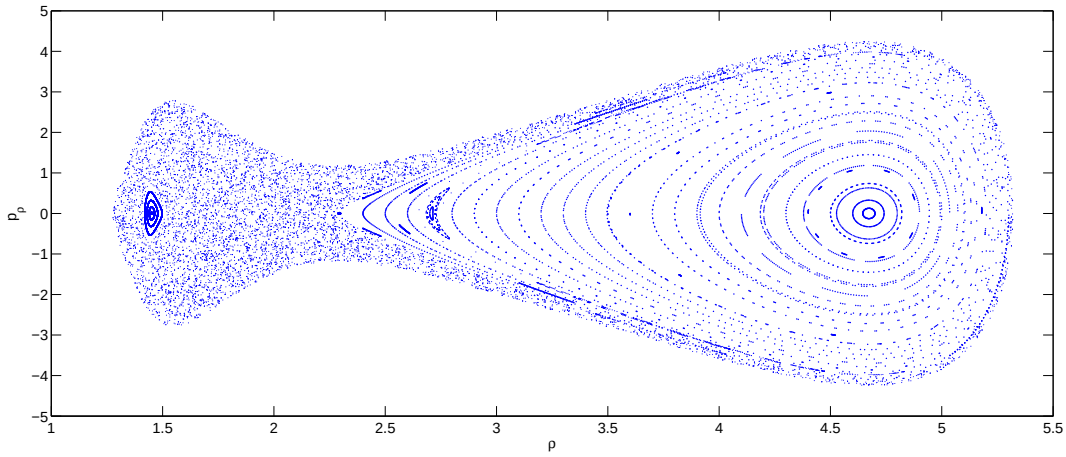

(b)

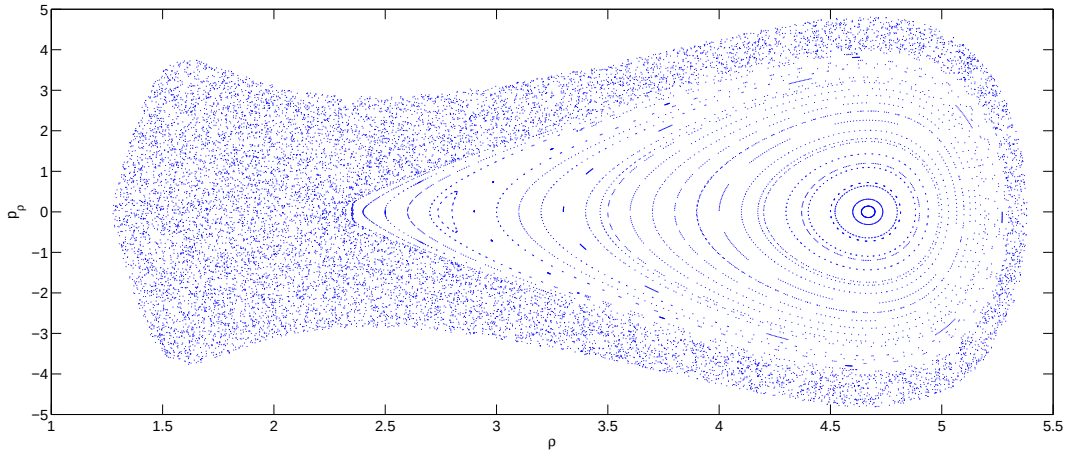

(c)

Figure 7.2: **Poincaré maps corresponding to the orbits of Figure 7.1. As the neck widens the *stickiness* surrounding the outer KAM curves increases. This emphasises that not only orbits with initial condition in the inner region traverse the neck. Instead orbits lying between the last KAM curve and the outer boundary of the physical space visit both regions too. The increase in neck width causes the multiplicity 3 island in the outer region to move closer to the neck and shrink. In the inner region the main island of stability shrinks from *(a)* to *(b)* and finally disappears in *(c)*.**

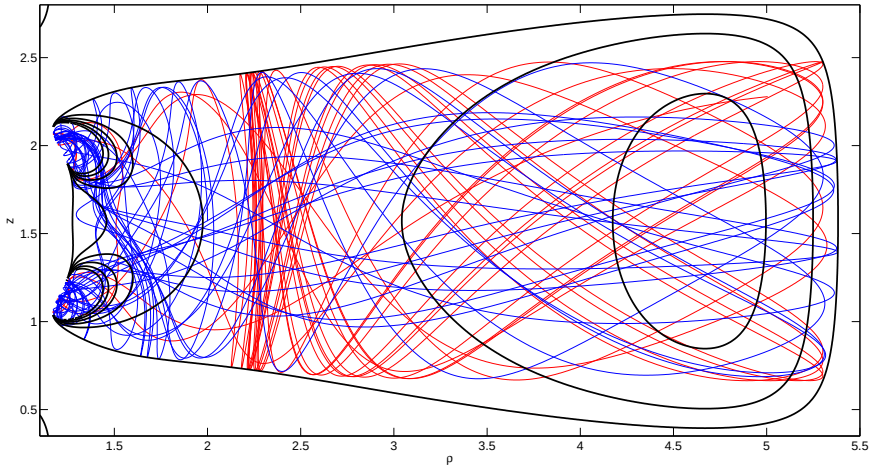

Figure 7.3: **Two orbital trajectories in the physical space prescribed by the parameters $E = 0.98$ and $L_z = 2$. Overlaid is a contour map of the effective potential $J(\rho, z)$. The two prominent spikes in the effective potential ($\rho \approx 1.2$) cause orbits to cluster in this area of the plot.**

the roots of the potential. In Appendix C I set out to calculate the roots of the Manko-Novikov potential as a function of S, q, E and L_z on the equatorial plane. Eventually I had to be satisfied with only an analytical expression for the biggest equatorial root, and even such an expression is long and messy. In the next chapter I devise a different scheme for investigating the occurrence of resonances (and therefore possibly chaos) as a function of the complete parameter space.

CHAPTER 8
Resonances in Kerr spacetime

In this chapter I start an investigation of the low-order resonances in the Kerr metric. The idea is to explore, as a function of the complete parameter space, where low-order resonances in Kerr are likely to occur if the spacetime is to be perturbed. The study was conducted (and will be expanded on) in collaboration with Dr. Jeandrew Brink and Dr. Tanja Hinderer [7].

From the previous chapters discussing the Manko-Novikov spacetime (Chapter 6 and 7) it is clear that a change in any of the parameters that characterise a geodesic in the spacetime will alter the shape of the effective gravitational potential and consequently influence the regularity of the orbits. Chapter 7 demonstrated how changes in the gravitational potential can create changes in the transport of orbits between the ergodic region and the more regular region of the system. Ultimately the geodesic parameters determine where resonances and the associated breakdown of ordered orbits take place in the Manko-Novikov spacetime.

To date there have been a couple of studies, most notably by Contopoulos, Apostolatos and Lukes-Gerakopoulos, that aim to quantify the occurrences of resonant orbits in the Manko-Novikov metric. The investigations are conducted by changing each geodesic parameter independently and then noting how the change modifies the shape of the effective potential as well as the location of the Birkhoff chains in the corresponding Poincaré map [16, 15]. The shortcoming of such an approach is that you are considering the impact of one parameter by itself separate from the impact of the others. In this way you are always only analysing a very specific situation and not sampling all of the orbits or all of the parameter space. Ideally we would like to understand the occurrence of resonances in the Manko-Novikov metric as a function of all the parameters.

The integrable Kerr metric provides an easier model in which to characterise the resonant orbits as a function of the complete parameter space. A natural set of variables to transform to under these circumstances are the Keplerian parameters conventionally used to describe elliptical orbits. These variables serve well to characterise the physics and geometry of the orbit in an easily interpretable manner and allow for a direct reduction to ordinary orbital parameters in the Newtonian regime. This means that instead of describing an orbit in terms of the probe's energy E, angular momentum L_z and the Carter constant Q, the orbit is characterised geometrically by its eccentricity e, its inclination angle θ_- and its semi-latus rectum p. The probe's closest approach to the central orbit along the elliptical track is called the *periastron* and is given by

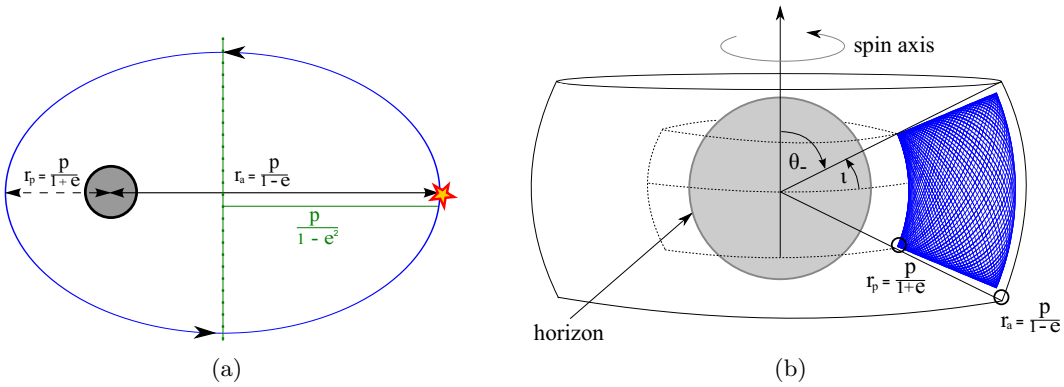

Figure 8.1: *(a)* **Parameters describing an elliptic orbit of a probe around a black hole. The eccentricity, e, is a measure of how elliptic the orbit is, i.e. how much it deviates from a circular orbit. The orbit is perfectly circular when $e = 0$. As e deviates from 0 it becomes more elliptic until at $e = 1$ the orbit is no longer an ellipse but has a parabolic trajectory instead. The semi-lactus rectum, p, can be defined in terms of the eccentricity and the semi-major axis of the ellipse as is show in green in the figure. The closest approach of the probe to the compact object is called the *periastron* and given by r_p in the sketch. The furthest orbital approach is the *apastron* and is denoted by r_a. *(b)* The orbital trajectories around a Kerr black hole. The third orbital parameter necessary to describe these orbits (apart from p and e) is the inclination angle θ_-. It measures the angle between the rotation axis of the black hole and the orbital plane. This can alternatively be described by $\iota = \pi/2 - \theta_-$, the angle with respect to the black hole's equatorial plane.**

$r_p = p/(1+e)$. The furthest distance between the probe and the compact object is the *apastron* and equal to $r_a = p/(1-e)$. See Figure 8.1 for the geometrical interpretation of these parameters.

By the KAM theorem (presented in Section 4.6) we expect the orbits that have the lowest resonance value, i.e. for which the denominator of the ratio of the frequencies ω_r/ω_θ is the lowest, to have the biggest measurable impact. We have also seen in Chapter 6 that the 1/2- and 2/3-resonances show up for orbits in the Manko-Novikov spacetime. For these reasons I study the occurrence of the 1/2- and 2/3-resonance in Kerr in this chapter. The methods used can however be applied for finding higher order resonances as well. There are different ways of computing the characteristic frequencies of orbits in the Kerr metric. A systematic approach was presented by Schmidt in 2002 [54] who used the integrability of the Kerr metric to rewrite the associated Hamiltonian in terms of action angle variables. Form Chapter 4 Section 4.1 we know that, once a Hamiltonian system is written in action angle variables, computing its characteristic frequencies is straightforward (see Eqs. (4.3) and (4.4)). In the next section I give a quick overview of Schmidt's results.

8.1 The Kerr Fundamental Frequencies

To determine the action angle variables a canonical transformation is needed such that the Kerr Hamiltonian becomes cyclic in all the new generalised coordinates. In Section 4.1 it was shown that this is similar to finding a characteristic function (W) which is a solution to the Hamilton-Jacobi equation given in Eq. (4.2).

An expression for the Hamiltonian associated with the Kerr spacetime is obtained by substituting the Kerr line element (given in Boyer-Lindquist coordinates in Eq. (5.1)) into the general expression for the Hamiltonian of an SAV spacetime (Eq. (3.5)),

$$\begin{aligned} H(\boldsymbol{q},\boldsymbol{p}) = &-\frac{(r^2+a^2)^2-\Delta a^2\sin^2\theta}{2\Delta\Sigma}{p_t}^2 - \frac{2aMr}{\Delta\Sigma}p_t p_\phi \\ &+\frac{\Delta - a^2\sin^2\theta}{2\Delta\Sigma\sin^2\theta}{p_\phi}^2 + \frac{\Delta}{2\Sigma}{p_r}^2 + \frac{1}{2\Sigma}{p_\theta}^2, \end{aligned} \tag{8.1}$$

where $\Sigma = r^2 + a^2\cos^2\theta$, $\Delta = r^2 - 2Mr + a^2$ and $a = S/M$ is the spin per unit mass, as before. The generalised coordinates and momenta are given by $q = (t, r, \theta, \phi)$ and $p = (p_t, p_r, p_\theta, p_\phi)$.

After replacing the constants of motion $E = -p_t$, $L_z = p_\phi$ and Carter constant Q with the expression given in Eq. (5.4), the characteristic function is given by

$$W = -Et + \int \frac{\sqrt{R}}{\Delta}dr + \int \sqrt{\Theta}d\theta + L_z\phi, \tag{8.2}$$

with

$$R = \left[(r^2+a^2)E - aL_z\right]^2 - \Delta\left[\mu^2 r^2 + (L_z - aE)^2 + Q\right], \tag{8.3}$$

$$\Theta = Q - \left[(\mu^2 - E^2)a^2 + \frac{L_z^2}{\sin^2\theta}\right]\cos^2\theta. \tag{8.4}$$

R and Θ are known as the radial and polar potentials respectively [54]. The characteristic function is used to rewrite the Hamiltonian using the action angle variables into a form from which the fundamental frequencies can be calculated. For the details of the calculation I refer the reader to Schmidt's paper [54]. The closed form expressions for the fundamental frequencies are given in terms of integrals that can be approximated numerically. In terms of the Keplerian variables (p, e, θ_-) and dimensionless quantities the characteristic frequencies $\bar{\omega_r}$ and $\bar{\omega_\theta}$ are expressed as

$$\bar{\omega_r} = \frac{\pi p K(k)}{(1-e^2)\Lambda} \tag{8.5}$$

$$\bar{\omega_\theta} = \frac{\pi \bar{\beta} z_+ \bar{X}}{2\Lambda}, \tag{8.6}$$

$$\text{with} \qquad \Lambda = (\bar{Y} + \bar{a}^2 z_+^2 \bar{X})K(k) - \bar{a}^2 z_+^2 \bar{X} E(k). \tag{8.7}$$

The barred quantities are dimensionless and $\bar{\beta}^2 = \bar{a}^2(1-\bar{E}^2)$. The roots of the polar potential (Eq. (8.4)) are expressed as $z_\pm^2$ after having made the substitution $z = \cos\theta$, i.e. $\Theta(z_\pm^2) = 0$. The parameter k is a function of these roots such that $k = \sqrt{z_-/z_+}$. $K(k)$ and $E(k)$ are elliptic integrals of the first and second kind respectively. The dimensionless radial integrals in Eqs. (8.5) - (8.7) have the form

$$\bar{X} = \int_0^\pi \frac{d\chi}{\sqrt{J(\chi)}} \tag{8.8}$$

$$\bar{Y} = \int_0^\pi \frac{p^2 d\chi}{(1+e\cos\chi)^2\sqrt{J(\chi)}}, \tag{8.9}$$

where J is defined by

$$\begin{aligned} J(\chi) = {} & (1-\bar{E}^2)(1-e^2) + 2(1-\bar{E}^2 - \frac{1-e^2}{p})(1+e\cos\chi) \\ & + ((1-\bar{E}^2)\frac{3+e^2}{1-e^2} - \frac{4}{p} + [\bar{a}^2(1-\bar{E}^2) + \bar{L_z}^2 + \bar{Q}]\frac{1-e^2}{p})(1+e\cos\chi)^2. \end{aligned} \tag{8.10}$$

The parameters E, L_z and Q in Eq. (8.10) should be interpreted as functions of p, e and $z_- = \cos\theta_-$, such that in the end the fundamental frequencies are functions of only one set of constants of motion. For a given set of orbital parameters p, e and θ_-, I use the scheme suggested in Appendix B of [54] to calculate the values E, L_z and Q numerically. Four possible solution sets (E, L_z, Q) arise for a given set of p, e and θ_-. The solution sets can easily be reduced to two, by noting that two solutions correspond to the time reversal of the motion. The remaining two solutions, (E^P, L_z^P, Q^P) and (E^R, L_z^R, Q^R), can be interpreted as particles that either corotate or counterrotate with respect to the rotation of the black hole. Orbits of particles that corotate with the black hole are called *prograde* orbits and those that counterrotate are called *retrograde* orbits. The prograde angular momentum is higher than the retrograde angular momentum. On the other hand prograde orbits have lower orbital energy and retrograde orbits higher orbital energy [54]. In the case of prograde orbits the particle's angular momentum L_z and the intrinsic spin of the black hole S (or a) have the same sign, since the rotation is in

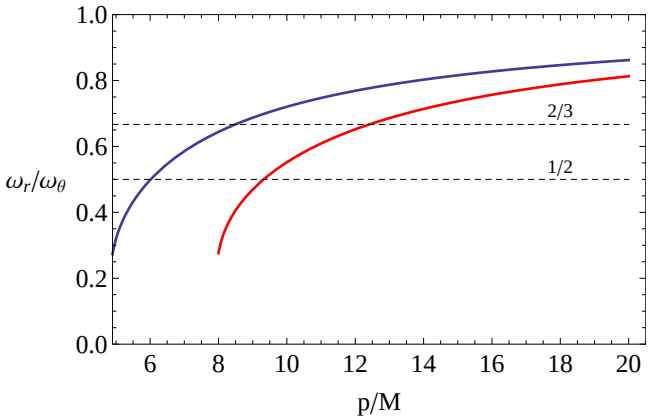

Figure 8.2: **The ratio of the fundamental orbital frequencies ω_r/ω_θ for parameter values $a = 0.95$, $e = 0.638$ and $\iota = 1.2$ as a function of the semi-latus rectum, p, given in units of M. The ratio of frequencies for prograde orbits is shown in blue and for retrograde orbits in red. In a retrograde system the possibility of encountering resonances occur further out than for the prograde system. Two resonant frequency values, $1/2$ and $2/3$, are highlighted in the figure. If the Kerr metric is perturbed it is likely that orbits corresponding to these parameters values will be sources of chaotic motion.**

the same direction. In the case of a retrograde orbit the particle's angular momentum has the opposite sign of the black hole's spin.

8.2 Characterising resonances in the global parameter space

I now characterise the ratio of the fundamental frequencies, ω_r/ω_θ, in terms of the orbital parameters p, e and ι, where $\iota = \pi/2 - \theta_-$ is the inclination angle with respect to the equatorial plane as shown in Figure 8.1(b). Figure 8.2 shows ω_r/ω_θ for a given eccentricity (e) and inclination angle (ι) while the semi-latus rectum (p) is the only dependent variable. The ratios of frequencies for both retrograde and prograde orbits are shown. The fundamental frequencies were calculated numerically using Eqs. (8.5) - (8.10). In Figure 8.2 the rational fraction values $\omega_r/\omega_\theta = 1/2$ and $2/3$ are highlighted. From the plot it is clear that the resonances, $1/2$ and $2/3$, occur further out from the black hole for retrograde orbits than for prograde orbits. For both prograde and retrograde systems the $2/3$-resonance is encountered before reaching the closer in $1/2$-resonance. In the case of a retrograde system the $2/3$-resonance corresponds to $p \approx 12.4M$ such that $r_a \approx 34.3M$ and $r_p \approx 7.6M$.

In order to facilitate a complete parameter study I am interested in finding out where low-order resonances are expected to occur for the parameter space as a whole. I choose a single resonance, the $2/3$ resonance, and search for the values of (e, p, ι) for which the ratio ω_r/ω_θ equals $2/3$. The expression for ω_r/ω_θ given by Eqs. (8.5) and (8.6) is a function of p, e and ι.

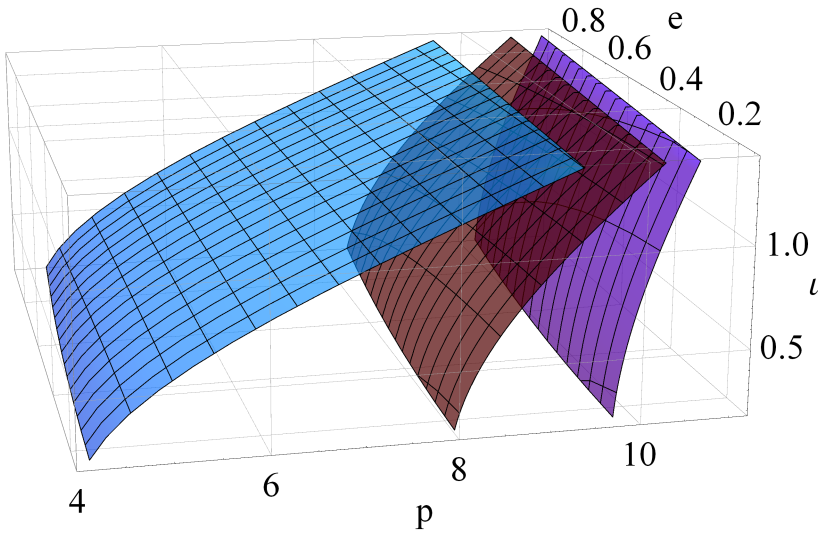

Figure 8.3: **The orbital constants of motion (e, p, ι) for which the ratio of the fundamental frequencies $\omega_r/\omega_\theta = 2/3$. For these orbits we therefore expect that resonance is likely to occur if the Kerr spacetime is perturbed. Each sheet represents prograde motion and corresponds to a different spin value of the Kerr black hole. The blue (left) sheet has a spin value of $S = 0.99$, the red (middle) sheet has $S = 0.5$ and the magenta (right) sheet has $S = 0.2$. The lower the spin value of a prograde orbit, the further out resonance will occur. The resonances seem to be rather insensitive to the effect of eccentricity.**

Since the values for e and ι are well constrained, with $0 < e < 1$ and $0 < \iota < \pi/2$, I choose several e's and ι's to cover this range and numerically solve the implicit equation $\omega_r/\omega_\theta = 2/3$ for p. The resulting sets of data points are plotted to form the sheets in Figure 8.3. All three sheets correspond to prograde orbits, each with a different spin parameter. The lower the spin value and the more inclined the orbital plane, the larger the corresponding p value and therefore, the further out the resonances occur.

From Figure 8.3 we note that the eccentricity of the orbit has the least impact on the location of the resonances. A quick way to therefore optimise the numerical work is to choose the eccentricity constant and solve for the values of p and ι for which the frequency ratios have the rational fraction value of 2/3. Figure 8.4 shows the dependence of the orbits on these two parameters, p and ι, for both prograde and retrograde orbits with different spin values. In the case of the retrograde orbits the resonant orbits move outward as the spin increases. We understand this phenomenon by the fact that in general the orbits of probes are pushed outward when they are counterrotating with the black hole and pulled inward when they corotate.

The plot also shows that, the higher the inclination angle, the less dependent the resonances are on the spin value of the black hole. This makes sense since at $\iota \approx \pi/2$ you have a polar orbit where the spin axis lies in the orbital plane. From Figure 8.4 we see that, in the case of a rapidly

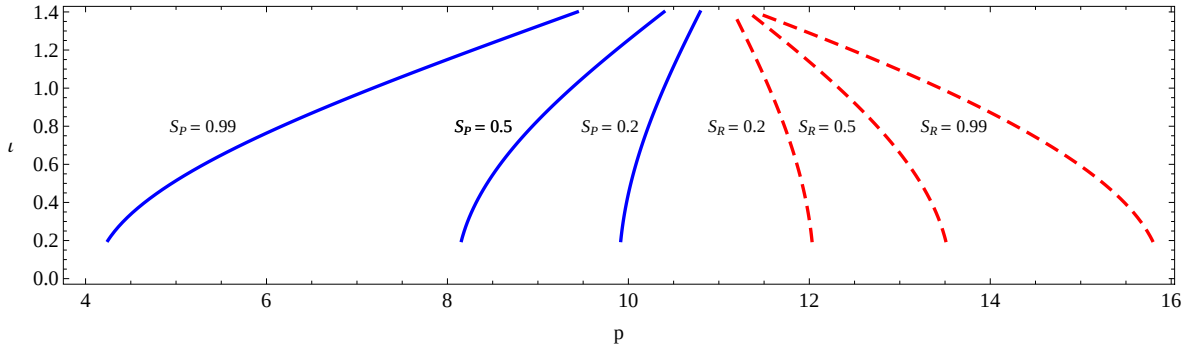

Figure 8.4: **Curves corresponding to the resonance value of $2/3$ as a function of p and ι, but with a constant eccentricity of $e = 0.6$. The blue (solid) curves correspond to a two dimensional projection of the prograde sheets shown in Figure 8.3 with spin decreasing from $S = 0.99$ to 0.5 to 0.2 from left to right. The red (dashed) curves are the complementary curves for retrograde orbits. Here spin increases from left to right with the same three numerical values as for the prograde curves.**

spinning black hole ($S = 0.99$) and a probe on an orbit with $e = 0.6$ close to the equatorial plane, the resonances can occur as far in as $p \approx 4M$ for prograde orbits and as far out as $p \approx 16M$ for retrograde orbits. This translates to radial values of $r_p \approx 2.5M$, $r_a \approx 10M$ and $r_p \approx 10M$, $r_a \approx 40M$ respectively.

To determine whether these resonances will be observable by LISA (or eLISA) in the Galactic Centre, consider the following expression for the radial separation of two inspiraling masses as a function of the gravitational wave frequency [9].

$$R \approx 300(\frac{M}{2.8M_{\odot}})^{1/3}(\frac{100Hz}{f_{GW}})^{2/3} \text{ km} \tag{8.11}$$

where M is the mass of the compact object and f_{GW} the frequency of the emitted gravitational waves. This can be expressed in units of mass by dividing by the conversion factor G/c^2[‖]. As was mentioned in Chapter 1, eLISA will be operational in the frequency band 10^{-4}Hz to 10^{-1}Hz. Recent studies have estimated the mass of Sgr A* at $M_{SgrA*} \approx 4.31 \times 10^6 M_{\odot}$ [26]. Inserting these values into Eq. (8.11) we see that eLISA is sensitive to probes at a radial distance of $0.54M$ to $54M$ with respect to Sgr A*. This overlaps with the region within which we roughly expect to pick up resonances in a perturbed Kerr metric. These results will also be valid for the Manko-Novikov spacetime with a small quadrupole moment deviation for which the Kerr spacetime is a good approximation. If indeed the gravitational wave detectors are troubled by resonances and the introduction of chaotic orbits, disentangling structural information about the

[‖] G is the gravitational constant equal to $G = 6.67384 \times 10^{-11} m^3 kg^{-1} s^{-2}$ and $c = 299792458 ms^{-1}$ is the speed of light.

compact object central to the EMRI event will be increasingly complicated.

8.3 The Relationship between rotation curves and the Keplerian parameter study

In this section I aim to reconcile the parameters used to produce rotation curves via Poincaré maps of the Kerr metric, with the Keplerian variables introduced in this chapter. A complete and analytic understanding of this transformation forms part of a study still in progress. Here I give one example to show that the transformation holds.

To check this transformation for the Kerr metric I start by picking a set of (p, e, ι) associated with the resonance for which $\omega_r/\omega_\theta = 2/3$ for a given spin value. If I choose a prograde orbit with the spin value equal to $a = 0.5$ this means I pick off a point on the red (middle) sheet of Figure 8.3. Let this point be $(p, e, \iota) \approx (8.5827, 0.6, 0.6)$. Using the numerical technique put forth in Appendix B of [54] I can calculate the corresponding prograde energy and angular momentum value. I find that

$$\begin{aligned} E^p(a, p, e, \iota) &= E^p(0.5, 8.5827, 0.6, 0.6) \approx 0.96525 \\ L_z^p(a, p, e, \iota) &= L_z^p(0.5, 8.5827, 0.6, 0.6) \approx 2.9015 \end{aligned} \tag{8.12}$$

I use these orbital constants of motion together with initial conditions along the equatorial plane and initial momentum out of the plane to set up the equations of motion as before (Eq. (3.11)). I solve these using the same (independent) integrator that was used in Section 6.4 to produce the associated Poincaré map and its corresponding rotation curve. These are shown in Figure 8.5. I want to pick off the 2/3 resonance from the rotation curve and check that the coordinates describing its location matches the Keplerian coordinates used to describe this resonance in Figure 8.3. Interpolating the data used to produce the rotation curve in Figure 8.5(b) shows that the 2/3 resonance occurs when $\rho \approx 2.30007$. From Eqs. (5.9) and (5.10) this corresponds to the Boyer Lindquist $r \approx 5.3627$. By the Keplerian variables this same periastron r_p value can be calculated using

$$r_p = \frac{p}{1+e} = \frac{8.5827}{1.6} = 5.3642. \tag{8.13}$$

The physical r-location for which the $\omega_\theta/\omega_r = 2/3$ resonance occurs in the Kerr spacetime is therefore independent of the choice of coordinates and the procedure followed. I executed this check for several orbits to ensure that the transformation holds regardless of the initial

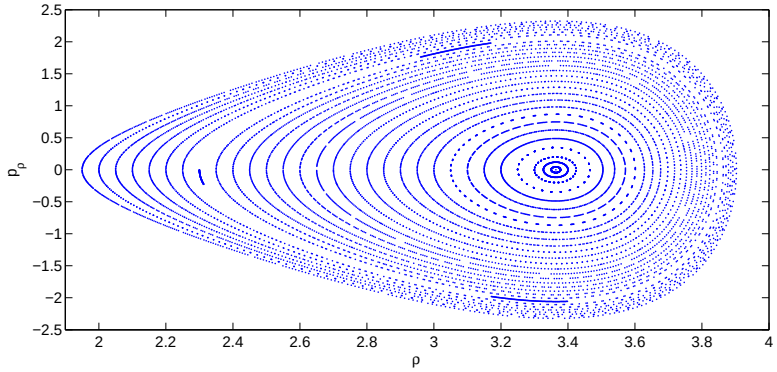

(a)

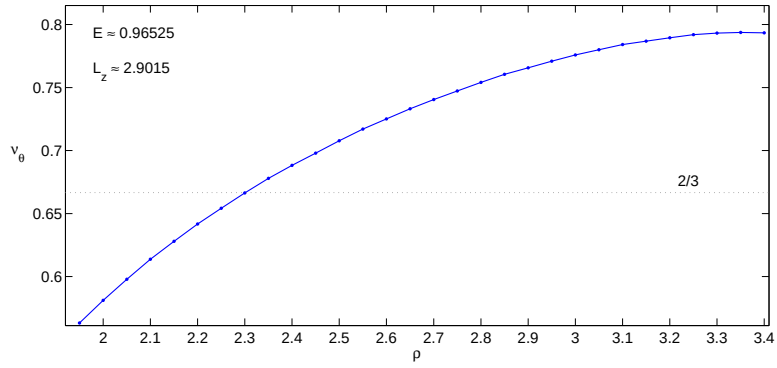

(b)

Figure 8.5: *(a)* **The Poincaré map for orbits with constants of motion** $(E, L_z, S) = (0.96525, 2.9015, 0.5)$**. The quadrupole deviation parameter has been set to zero to simplify the Manko-Novikov effective potential to that of Kerr (see Appendix B). The absence of any islands of stability confirms that this is indeed the integrable Kerr metric. The initial conditions of all the orbits lie along the equatorial plane with initial momenta out of the plane.** *(b)* **The rotation curve associated with the Poincaré map above. The 2/3-periodic orbit is shown where the dashed line intersects the curve, i.e. at** $\rho \approx 2.30007$**.**

conditions. A quick and analytic transformation between the methods will be a valuable tool for switching between the coordinates in which observables of an EMRI event is measured and coordinates that are theoretically convenient to use.

8.4 Resonances with Carlson's Integrals

Producing the numerical sheets in Figure 8.3 was computationally expensive** and therefore prompted an investigation into solving the fundamental frequencies for Kerr globally in a more efficient way. We are currently investigating using Carlson's integrals to speed up the evaluation

**The calculations were done in Mathematica and ran over several hours on a desktop PC with 8 cores (Intel i7) of 2GB RAM each.

of the fundamental frequencies. This study is still in an infant phase such that, apart from introductory statements about Carlson's integrals, no results are presented in this section.

We have seen that resonant orbits are defined by the parameter values for which ω_r and ω_θ have commensurate values. We first rewrite this condition in terms of the radial and polar potentials respectively. In order to do so we investigate the associated equations of motion. By Eq. (4.1) we have that $p_\beta = g_{\beta\alpha}\partial W/\partial q^\alpha$. Using the expression for the characteristic function (Eq. (8.2)) along with Kerr Hamiltonian given in Eq. (8.1), the r and θ equations of motion are given by [12, 47]

$$\mu\Sigma\frac{dr}{d\tau} = \sqrt{R} \qquad\qquad \mu\Sigma\frac{d\theta}{d\tau} = \sqrt{\Theta}, \tag{8.14}$$

with τ proper time and R and Θ as defined in Eqs. (8.3) and (8.4). From the above the fundamental frequencies become

$$\mu\Sigma\int_{r_p}^{r_a}\frac{dr}{\sqrt{R}} = \int_{\tau_1}^{\tau_2} d\tau = \frac{1}{\omega_r} \tag{8.15}$$

$$\mu\Sigma\int_{-\theta_-}^{\theta_-}\frac{d\theta}{\sqrt{\Theta}} = \int_{\tau_1}^{\tau_2} d\tau = \frac{1}{\omega_\theta}, \tag{8.16}$$

where the boundaries of the integrals are the turning points of the radial and polar potentials respectively. The resonance condition therefore becomes

$$m\int_{-\theta_-}^{\theta_-}\frac{1}{\sqrt{\Theta}}d\theta = n\int_{r_p}^{r_a}\frac{dr}{\sqrt{R}} \tag{8.17}$$

with m and n integers.

The integrals in the above equation can be rewritten in terms of Carlson's integrals as follows. Start by writing the radial (R) and polar potential (Θ) in terms of their roots. The radial potential is a fourth order polynomial with roots $r_a > r_p > r_3 > r_4$. After substituting $z = \cos\theta$, the polar potential can be expressed as the square of a quadratic polynomial with roots $z_\pm$. The integrals in Eq. (8.17) become

$$an\int_{r_a}^{r_p}\frac{dr}{\sqrt{(r_a - r)(r - r_p)(r - r_3)(r - r_4)}} = m\int_{-z_-}^{z_-}\frac{dz}{\sqrt{(z^2 - z_-^2)(z^2 - z_+^2)}} \tag{8.18}$$

with a the spin of the Kerr black hole.

These integrals can be written in terms of Carlson's integrals which have the form

$$R_F(\alpha,\beta,\gamma) = \frac{1}{2}\int_0^\infty \frac{dt}{\sqrt{(t+\alpha)(t+\beta)(t+\gamma)}}. \tag{8.19}$$

The Carlson's integrals provide a rapidly converging numerical scheme and even the potential of finding an analytical solution for the fundamental frequencies. We hope to make use of the symmetries of these types of integrals to solve the resonant conditions. The Carlson's symmetries are (amongst others)

$$R_F(\alpha,\beta,\gamma) = 2R_F(\alpha+\lambda,\beta+\lambda,\gamma+\lambda), \tag{8.20}$$

where $\lambda = (\alpha\beta)^{1/2} + (\alpha\gamma)^{1/2} + (\beta\gamma)^{1/2}$. Also $R_F(\beta,\beta,\beta) = \beta^{-1/2}$. Carlson's functions are furthermore homogeneous of degree $-1/2$, such that

$$R_F(\lambda\alpha,\lambda\beta,\lambda\gamma) = \lambda^{-1/2}R_F(\alpha,\beta,\gamma). \tag{8.21}$$

In terms of Carlson's integrals, the resonance condition of Eq (8.18) becomes

$$anR_F(0,(r_p-r_3)(r_a-r_4),(r_p-r_4)(r_a-r_3)) = mR_F(0,(z_-+z_+)^2,(z_--z_+)^2) \tag{8.22}$$

By employing the symmetries of Carlson's integrals, this can be rewritten such that

$$R_F(0,(r_p-r_3)(r_a-r_4),(r_p-r_4)(r_a-r_3)) = R_F(0,\frac{a^2n^2}{m^2}(z_+^2-z_-^2),\frac{a^2n^2}{m^2}z_+^2) \tag{8.23}$$

The most naive way of solving this equations is to say that the individual entries in each R_F function must be equal. This may not be the most general solution, but it is a starting point. This brings us to

$$(r_p-r_3)(r_a-r_4) = \frac{a^2n^2}{m^2}(z_+^2-z_-^2) \tag{8.24}$$

$$(r_p-r_4)(r_a-r_3) = \frac{a^2n^2}{m^2}z_+^2 \tag{8.25}$$

Note that the ratio of these equations is independent of the resonance condition i.e.

$$\frac{(r_p-r_3)(r_a-r_4)}{(r_p-r_4)(r_a-r_3)} = 1-\frac{z_-^2}{z_+^2} \tag{8.26}$$

The next step is to solve the roots of this equation and check whether this could provide a much quicker numerical scheme by which to produce projections of the sheets in Figure 8.3. Finalising this work however lies beyond the scope of this thesis.

CHAPTER 9
Conclusions and Outlook

In this thesis I used the EMRI model to seek a framework within which we will be able to differentiate between traditional Kerr black holes and bumpy black holes observationally. The Manko-Novikov metric was presented as an example of a spacetime that allows for compact objects with multipole mass moments different from Kerr. The dynamics of a low mass probe in the effective Manko-Novikov potential and the dependence of this motion on the geodesic parameters was studied. In Chapters 6 and 7, the Manko-Novikov spacetime was explored numerically to determine whether this non-Kerr spacetime admits any extra constants of motion, i.e. whether it is integrable or not. By means of Poincaré maps (Figure 6.7) it was found that certain periodic orbits in the Manko-Novikov spacetime break up into islands of stability, called Birkhoff chains of islands, with differing multiplicities. These are smoking guns for Hamiltonian systems which are not integrable. A system which is not integrable can in turn not possess additional conserved quantities beyond E, L_z and μ. The rotation curves of Figure 6.9 and 6.10 were used to demonstrate that the islands of stability are associated with orbits for which the ratio of fundamental frequencies has a rational fraction value. It is through resonances that the breaking of regular orbital motion or alternatively the introduction of chaotic motion takes place. These findings are in accordance with the predictions of the Poincaré-Birkhoff Theorem and the KAM theorem of Sections 4.5 and 4.6. The orbits for which the fundamental frequencies have a ratio equal to a low-order rational fraction such as 2/3 show up as plateaus in the rotation curves drawn from the corresponding Poincaré maps. These plateaus in rotation curves can serve as possible observational signatures by which gravitational wave detectors and radio telescopes using pulsar timing arrays, can differentiate between Kerr black holes and non-Kerr black holes. Apart from an outer region of the effective potential containing predominantly regular orbits an inner region exhibiting full blown chaos was also found (Figure 6.7(c)). Changing the orbital constants of motion (E and L_z) can cause these two regions to merge. Figure 7.1 and 7.2 shows that within this joint non-convex potential orbits with a hybrid structure of order and chaos arise. The general increase in the chaos of the system raises questions as to how well we will be able to distinguish between Kerr and Manko-Novikov black holes, and how trustworthy and predictable observations will be.

In Chapter 8 I initiated a study by which we ultimately aim to quantify the occurrence of resonances in the complete Kerr parameter space. The results for the Kerr metric will be valid

for the Manko-Novikov spacetime with a small quadrupole moment deviation (see Section 6.7.1 and Appendix B) and provide quantitative insight into the dynamics of the problem. By the KAM theorem we expect the break of regularity under a perturbation of the Kerr spacetime to be best observable for orbits with low-order commensurate frequency values. For this reason I investigated the occurrence of the lower order resonances in the Kerr metric as a function of its orbital parameters. I find that the 2/3-resonance occurs further out than the 1/2-resonance as shown in Figure 8.2. Furthermore in Figure 8.4 I showed that the resonances associated with retrograde orbits occur further out than those associated with prograde orbits. The higher the spin value of the black hole, the closer in (further out) the resonances for prograde (retrograde) orbits occur. This analysis quantises where in the parameter space resonances occur. Our finding that resonances occur within 40 M (20 Schwarzschild radii) of the event horizon has mainly two implications for observations in the Galactic Centre

1. Resonances occur in the region where EMRIs enter the eLISA frequency band (10^{-4} Hz - 10^{-1}Hz) when orbiting Sgr A*

2. There is a large regime between 50M and 1000M where pulsar timing techniques can be used to track EMRI's free of resonances. In this nearly integrable regime our result that low-order resonances are absent, guarantees that canonical perturbation theory calculations correctly capture the dynamics. In the region where resonances occur the canonical perturbation theory fails.

The machinery used in Chapter 8 of this thesis to determine the location of resonances in the Kerr spacetime builds strongly on the work by Schmidt [54] who found a closed form expression for the Kerr fundamental frequencies as a function of the Keplerian variables. Unfortunately, solving the corresponding resonant orbits in this way is computationally expensive. A possible solution to speed up these evaluations is by means of Carlson's integrals. A further investigation into the effectiveness of such a technique will form part of a future study that complements the work done in this thesis.

Other possible future projects include an investigation into the smallest deviation from the Kerr quadrupole moment that we expect to be measurable. Most of the analysis of the Manko-Novikov metric in this thesis was conducted with an almost maximum quadrupole deviation measure of $q = 0.95$. It is questionable whether we should expect such a dramatic deviation. The impact of having a much smaller deviation parameter should be investigated thoroughly and a quantitative study made of the parameter space. To characterise the Manko-Noviko metric

more effeciently a method for finding an analytic expression for the roots of the effective potential would be valuable. This can then be used to approximate the Manko-Novikov potential by its Kerr equivalent and consequently solve the occurrence of resonances in the Manko-Novikov space globally.

APPENDIX A
Weyl Coordinates

Weyl coordinates (ρ_w, z_w) are related to the prolate spheroidal coordinates (x, y) in the following manner.

$$\rho_w = k\sqrt{(x^2-1)(1-y^2)} \qquad\qquad z_w = kxy \tag{A.1}$$

Both [22] and [45] presented their analysis of the Manko-Novikov spacetime in Weyl coordinates. The reverse relationship, namely prolate spheroidal coordinates (x, y) written in terms of Weyl coordinates (ρ_w, z_w), can be found by choosing

$$r_\pm = \sqrt{{\rho_w}^2 + (z_w \pm k)^2} \tag{A.2}$$

and

$$x = \frac{r_+ + r_-}{2k} \qquad\qquad y = \frac{r_+ - r_-}{2k}. \tag{A.3}$$

To check this relationship, we first note that from Eq. (A.3)

$$x^2 = \frac{r_+^2 + 2r_+r_- + r_-^2}{4k^2} \qquad\qquad y^2 = \frac{r_+^2 - 2r_+r_- + r_-^2}{4k^2} \tag{A.4}$$

and from Eq. (A.2)

$$r_+^2 + r_-^2 = \rho_w^2 + z_w^2 + 2kz_w + k^2 + \rho_w^2 + z_w^2 - 2kz_w + k^2 \tag{A.5}$$

$$= 2(\rho_w^2 + z_w^2 + k^2). \tag{A.6}$$

Substituting the expressions for x^2 and y^2 given by Eq. (A.4) into $\frac{\rho_w^2}{k^2} = (x^2-1)(1-y^2)$ gives

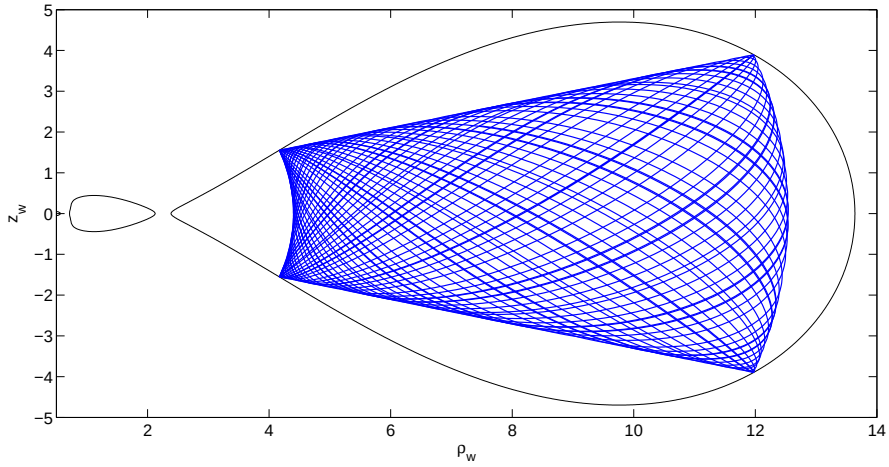

Figure A.1: **A physical space plot showing an orbital trajectory for the Manko-Novikov metric in Weyl coordinates. The parameters $E = 0.95$, $L_z = 3$, $S = 0.9$ and $q = 0.95$ are chosen to match and reproduce Figure 4 in [22] as well as Figure 1 in [45].**

$$
\begin{aligned}
\frac{\rho_w^2}{k^2} \Rightarrow & \left(\frac{r_+^2 + 2r_+r_- + r_-^2 - 4k^2}{4k^2}\right)\left(\frac{4k^2 - r_+^2 + 2r_+r_- - r_-^2}{4k^2}\right) && \text{using Eq. (A.6)} \\
&= \left(\frac{2(\rho_w^2 + z_w^2 - k^2) + 2r_+r_-}{4k^2}\right)\left(\frac{2r_+r_- - 2(\rho_w^2 + z_w^2 - k^2) +}{4k^2}\right) \\
&= \frac{4r_+^2r_-^2 - 4(\rho_w^2 + z_w^2 - k^2)^2}{16k^4} \\
&= \frac{4(\rho_w^2 + (z_w + k)^2)(\rho_w^2 + (z_w - k)^2) - 4(\rho_w^2 + z_w^2 - k^2)^2}{16k^4} && \text{using Eq. (A.2)} \\
&= \frac{4(\rho_w^2 + z_w^2 + 2kz_w + k^2)(\rho_w^2 + z_w^2 - 2kz_w + k^2) - 4(\rho_w^2 + z_w^2 - k^2)^2}{16k^4} \\
&= \frac{4(\rho_w^2 + z_w^2 + k^2)^2 - 16k^2z_w^2 - 4(\rho_w^2 + z_w^2 - k^2)^2}{16k^4} \\
&= \frac{\rho_w^2k^2 + z_w^2k^2 - z_w^2k^2}{k^4} \\
&= \frac{\rho_w^2}{k^2} \\
&= LHS, && \text{(A.7)}
\end{aligned}
$$

by which the transformation holds. Figure A.1 shows that the above transformation correctly reproduces the plots obtained by [22] and [45].

APPENDIX B
Manko-Novikov in the Kerr Limit

In this thesis it has often been mentioned that the Manko-Novikov metric can be simplified to the Kerr spacetime by dialling the quadrupole deviation to zero, that is to say *by flattening the bumps*. This Appendix verifies that the Kerr spacetime is a simplification of the Manko-Novikov spacetime and serves as a check of my numerical work in the previous chapters.

The deviation from Kerr has thus far been described by the parameter α_2, which relates to the actual quadrupole deviation parameter q through

$$\alpha_2 = \frac{qM}{k^3}, \tag{B.1}$$

where k is a function of the black hole spin, $k = M(1-\alpha^2)/(1+\alpha^2)$, as in Eq. (6.23). I again set $M = 1$ throughout. Switching the quadrupole bump off is then the same as setting $\alpha_2 = 0$, which reduces the Manko-Novikov coefficients (Eqs. (6.8) – (6.19)) as follows,

$$\tilde{\psi} = \alpha_2 \frac{P_2}{r^3} = 0 \tag{B.2}$$

$$\tilde{\gamma} = \frac{1}{2}\ln\left(\frac{x^2-1}{x^2-y^2}\right) - \frac{1}{2}\left(\ln\left(\frac{a}{-\alpha}\right) + \ln\left(\frac{b}{\alpha}\right)\right) + {\alpha_2}^2\left(\frac{3}{2}\right)^2 \frac{{P_3}^2 - {P_2}^2}{r^6} \tag{B.3}$$

$$= \frac{1}{2}\ln\left(\frac{x^2-1}{x^2-y^2}\right) \tag{B.4}$$

$$\ln\left(\frac{a}{-\alpha}\right) = -2\alpha_2[(x-y)\left(\frac{P_0}{r} + \frac{P_0}{r} + \frac{P_0}{r}\right)] = 0 \tag{B.5}$$

$$\ln\left(\frac{b}{\alpha}\right) = -2\alpha_2[(x+y)\left(\frac{P_0}{r} - \frac{P_1}{r^2} + \frac{P_2}{r^3}\right) - 1] = 0 \tag{B.6}$$

Note that from Eqs. (B.5) and (B.6) it follows that $a = -\alpha$ and $b = \alpha$, such that

$$A = (x^2-1)(1-\alpha^2)^2 - 4\alpha^2(1-y^2), \tag{B.7}$$

$$B = [x+1-\alpha^2(x-1)]^2 + 4\alpha^2 y^2, \tag{B.8}$$

$$C = 2\alpha(x^2-1)(1-\alpha^2) + 2\alpha(1-y^2)[1-\alpha^2+x(1+\alpha^2)]. \tag{B.9}$$

From the reduced parameters above I calculate the elements of the Manko-Novikov metric, in order to find a relationship between these and the Kerr parameters given by Eqs. (5.6) – (5.8).

I start by calculating $e^{2\psi}$ for the reduced Manko-Novikov spacetime,

$$\begin{aligned} e^{2\psi} &= e^{2\tilde{\psi}}\frac{A}{B} = \frac{A}{B} && \text{using Eq. (B.2)} \\ &= \frac{(x^2-1)(1-\alpha^2)^2 - 4\alpha^2(1-y^2)}{(x+1-\alpha^2(x-1))^2 + 4\alpha^2y^2} && \text{using Eqs. (B.7) and (B.8)} \\ &= \frac{k^2x^2 + \frac{4\alpha^2y^2}{1+\alpha^2}^2 - 1}{(kx+1)^2 + \frac{4\alpha^2y^2}{(1+\alpha^2)^2}}, && \text{(B.10)} \end{aligned}$$

where in the last step the substitution $k = (1-\alpha^2)/(1+\alpha^2)$ was made. Compare this result with the expression for $e^{2\psi}$ for the Kerr metric in Eq. (5.6),

$$e^{2\psi_\kappa} = \frac{p_\kappa^2x^2 + q_\kappa^2y^2 - 1}{(p_\kappa x+1)^2 + q_\kappa^2y^2}. \tag{B.11}$$

The κ-subscript is used to emphasise that these are the Kerr metric parameters as given in Section 5.2. Correlating p_κ^2 with k^2 and q_κ^2 with $\frac{4\alpha^2}{(1+\alpha^2)^2}$, which satisfies $p_\kappa^2 + q_\kappa^2 = 1$ as required, ensures a match. Next I calculate the reduced expression for $e^{2\gamma}$ by substituting Eqs. (B.2) and (B.9) into Eq. (6.9) to obtain

$$\begin{aligned} e^{2\gamma} &= e^{2\tilde{\gamma}}\frac{A(x^2-y^2)}{(x^2-1)(1-\alpha^2)^2} \\ &= \frac{A}{(1-\alpha^2)^2} \\ &= \frac{(x^2-1)(1-\alpha^2)^2 - 4\alpha^2(1-y^2)}{(1-a^2)^2} \\ &= x^2 - \frac{1}{k^2} + 4\alpha^2y^2(1-\alpha^2)^2 \\ &= \frac{x^2k^2 + \frac{4\alpha^2y^2}{(1+\alpha^2)^2} - 1}{k^2}. \end{aligned} \tag{B.12}$$

Compare this with the Kerr form,

$$e^{2\gamma_\kappa} = \frac{p_\kappa^2x^2 + q_\kappa^2y^2 - 1}{p_\kappa^2}. \tag{B.13}$$

This is equal to Eq. (B.12) above when again $p_\kappa^2 = k^2$ and $q_\kappa^2 = \frac{4\alpha^2}{(1+\alpha^2)^2}$ is chosen. It still remains to be shown that the Manko-Novikov form for ω reduces to the Kerr definition for ω_κ. This is done by substituting Eqs. (B.7) and (B.9) into Eq. (6.12),

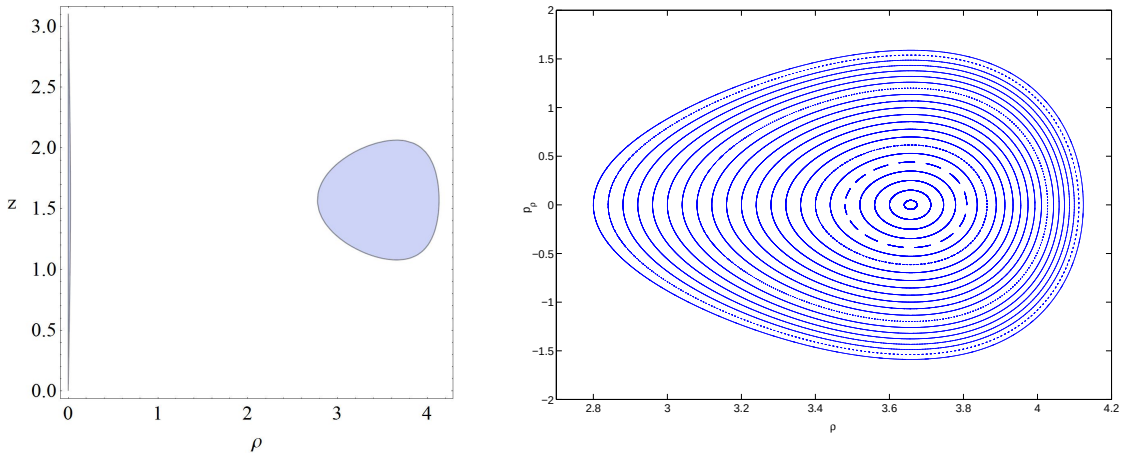

(a) (b)

Figure B.1: ***(a)*** **The reduced physical space of the Manko-Novikov metric when the quadrupole bumps are dialled away. This plot can either be found by using the Manko-Novikov coefficients of Section 6.1 and setting $q = \alpha_2 = 0$, with parameters $E = 0.95$, $L_z = 3$ and $S = 0.9$ ($\alpha = 0.6268$). Or by using the Kerr coefficients of Section 5.2 with $E = 0.95$, $L_z = 3$ and $S = 0.9$ ($\alpha = 0.6268$) while choosing $p_\kappa = k = (1-\alpha^2)/(1+\alpha^2) = 0.4359$ and $q_\kappa = 2\alpha/(1+\alpha^2) \approx 0.9$.** ***(b)*** **The Poincaré map for Manko Novikov simplified to Kerr, with the parameter set as for the physical space plot. In this Poincaré map I find only closed curves, which shows that Kerr is an integrable spacetime as was expected. The rotation curve associated with this Poincaré map is monotonically increasing without any plateaus.**

$$\omega = 2k\left(\frac{C}{A} - \frac{2\alpha}{(1-\alpha^2)}\right) \tag{B.14}$$

$$= 2k\cdot 2\alpha\left(\frac{(x^2-1)(1-\alpha^2)+(1-y^2)(1-\alpha^2+x(1+\alpha^2))}{(x^2-1)(1-\alpha^2)^2-4\alpha^2(1-y^2)} - \frac{1}{(1-\alpha^2)}\right) \tag{B.15}$$

$$= \frac{4k\alpha}{(1+\alpha^2)}\frac{1}{k}\left(\frac{(1-y^2)(1+kx)}{x^2k^2+\frac{4\alpha^2y^2}{(1+\alpha^2)^2}-1}\right), \tag{B.16}$$

which has the format for $\omega_\kappa = \frac{2kq_\kappa(1-y^2)(p_\kappa x+1)}{p_\kappa(p_\kappa^2x^2+q_\kappa^2y^2-1)}$ with $p_\kappa = k$ and $q_\kappa = \frac{2\alpha}{(1+\alpha^2)}$.

By choosing p_κ and q_κ as was given above, we have that all the coefficients of the Manko-Novikov line element reduce to those of Kerr. Plotting from this the Physical Space and Poincaré Maps for Kerr gives Figure B.1.

APPENDIX C
Analytical roots for the effective Manko-Novikov potential

C.1 Roots of Potential V

To find the roots of the effective potential J I consider

$$J = V(G - \mu^2) = 0 \tag{C.1}$$

so that $V = 0$ or $G = 1$, for $\mu = 1$. I start by solving $V = k^2 e^{2\gamma} e^{-2\psi} = 0$. To simplify the calculations I only consider roots on the equatorial plane, i.e. $y = 0$. Then

$$e^{2\gamma} e^{-2\psi} = e^{2\tilde{\gamma} - 2\tilde{\psi}} \frac{Ax^2}{(x^2-1)(1-\alpha^2)^2} \frac{B}{A} \tag{C.2}$$

$$= e^{2\tilde{\gamma} - 2\tilde{\psi}} \frac{Bx^2}{(x^2-1)(1-\alpha^2)^2}. \tag{C.3}$$

Next I investigate how the expressions for $\tilde{\gamma}$ and $\tilde{\psi}$ simplify on the equatorial plane. For the Legendre Polynomials we have $P_0 = 1, P_1 = 0, P_2 = 1/2$ and $P_3 = 0$. Also $r = (x^2 - 1)^{\frac{1}{2}}$. This brings about $a = -b$ for $y = 0$, so that

$$\tilde{\gamma} = \frac{1}{2} ln \frac{x^2 - 1}{x^2 - y^2} - \frac{1}{2}(ln(\frac{a}{-\alpha}) + ln(\frac{b}{\alpha})) + \alpha_2^2 \frac{9}{6} \frac{P_3^2 - P_2^2}{r^6} \tag{C.4}$$

$$= \frac{1}{2} ln \frac{x^2 - 1}{x^2} - ln(\frac{a}{-\alpha}) - \frac{3\alpha_2^2}{8r^6} \tag{C.5}$$

$$\tilde{\psi} = \frac{\alpha_2 P_2}{r^3} = -\frac{\alpha_2}{2r^3} \tag{C.6}$$

and hence

$$e^{2\psi - 2\gamma} = \Big(\frac{x^2 - 1}{x^2}\Big) \frac{\alpha^2}{a^2} e^{-\frac{3\alpha_2^2}{4r^6} + \frac{\alpha_2}{r^3}} \times \frac{Bx^2}{(x^2-1)(1-\alpha^2)^2} \tag{C.7}$$

$$= \frac{B\alpha^2}{a^2(1-\alpha^2)^2} e^{-\frac{3\alpha_2^2}{4r^6} + \frac{\alpha_2}{r^3}}. \tag{C.8}$$

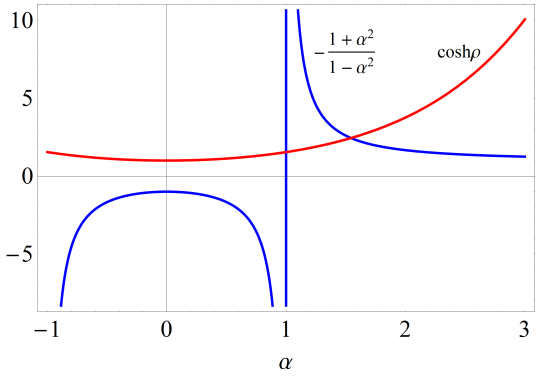

Figure C.1: **This figure shows there exists no points of intersection between $x = cosh\rho$ and $-1/k$ for $-1 < \alpha < 0$ which are the values that α takes on for spin values of $0 < S < 1$, by Eq. (6.23). This shows that the roots of the V potential do not dictate the roots of the effective potential J and we expect that potential G's roots will play an important role.**

Also, B on the equatorial plane is equal to $[x(1-\alpha^2)+(1+\alpha^2)]^2$, such that

$$V = \frac{k^2\alpha^2[x(1-\alpha^2)+(1+\alpha^2)]^2}{a^2(1-\alpha^2)^2} e^{-\frac{3\alpha_2^2}{4r^6}+\frac{\alpha_2}{r^3}} \tag{C.9}$$

$$= \frac{\alpha^2[x(1-\alpha^2)+(1+\alpha^2)]^2}{a^2(1+\alpha^2)^2} e^{-\frac{3\alpha_2^2}{4r^6}+\frac{\alpha_2}{r^3}}, \tag{C.10}$$

$$\tag{C.11}$$

where $k = (1-\alpha^2)/(1+\alpha^2)$ has been used.
Next insert $a = -\alpha e^{-2\alpha_2[x(\frac{1}{r}-\frac{1}{2r^3})-1]}$ to get

$$V = \frac{[x(1-\alpha^2)+(1+\alpha^2)]^2}{(1+\alpha^2)^2} e^{4\alpha_2[x(\frac{1}{r}-\frac{1}{2r^3})-1]-\frac{3\alpha_2^2}{4r^6}+\frac{\alpha_2}{r^3}}. \tag{C.12}$$

Finding the zeros to potential V amounts to solving

$$\frac{[x(1-\alpha^2)+(1+\alpha^2)]^2}{(1+\alpha^2)^2} = 0, \tag{C.13}$$

that is

$$x = -\frac{1+\alpha^2}{1-\alpha^2} = -\frac{1}{k}. \tag{C.14}$$

C.2 Roots of $G - \mu^2$

Since from the above it is clear that the roots of J will be determined by the roots of the function $G-\mu^2$, we set out to solve this. Again start by solving the roots on the equatorial plane, that is set $y = 0$ in the parameters for the Manko-Novikov metric. The following simplifications

come about

$$\frac{C}{B} = \frac{-2ax}{(x+1) - a^2(x-1)} \tag{C.15}$$

$$\frac{A}{B} = \frac{(x-1) + a^2(x+1)}{a^2(x-1) - (x+1)} \tag{C.16}$$

$$\frac{C}{A} = \frac{2ax}{(x-1) + a^2(x+1)}. \tag{C.17}$$

Using the above and substituting $a = -\alpha e^{-2\alpha_2[x(1/r - 1/2r^3) - 1]}$, the potential G can be expressed as

$$\begin{aligned} G = e^{-\frac{\alpha_2}{r^3}} \Big[& \alpha^2(\alpha^2-1)^2E^2(x-1)^3 e^{\frac{2\alpha_2}{r^3}} - (\alpha^2-1)^2E^2(x+1)^3 e^{-\frac{2\alpha_2(2r^3-2r^2x+x-1)}{r^3}} \\ & + (x-1)(4\alpha E + \alpha^2 L_z + L_z)^2 e^{2\alpha_2(-\frac{x}{r^3}+\frac{2x}{r}-2)} \\ & + 8\alpha(\alpha^2-1)E(4\alpha E + \alpha^2 L_z + L_z)x e^{-\frac{\alpha_2(2r^3-2r^2x+x-1)}{r^3}} \\ & - \alpha^2(x+1)(4\alpha E + \alpha^2 L_z + L_z)^2 \Big] \Big/ \Big[(\alpha^2-1)^2(x^2-1)(\alpha^2(x-1) - (x+1)e^{2\alpha_2(-\frac{x}{r^3}+\frac{2x}{r}-2)}) \Big]. \end{aligned} \tag{C.18}$$

Similarly, for Kerr (where $\alpha_2 = 0$) on the equatorial plane,

$$\begin{aligned} G_K = \Big[& -8EL_z\alpha(1+\alpha^2)^2 - L_z^2(1+\alpha^2)^2 - L_z^2(1+\alpha^2)^2(1+\alpha^2+x(\alpha^2-1)) \\ & + E^2(-1-15\alpha^2-15\alpha^4-\alpha^6+x^3(\alpha^2-1)^3 - 3x^2(\alpha^2-1)^2(\alpha^2+1) \\ & + x(-3-7\alpha^2+7\alpha^4+3\alpha^6) \Big] / \\ & \Big[(x^2-1)(\alpha^2-1)^2(-1-\alpha^2+x(\alpha^2-1)) \Big]. \end{aligned} \tag{C.19}$$

In the Kerr case solving for $G_K = 1$ amounts to solving the cubic polynomial

$$a_3x^3 + a_2x^2 + a_1x + a_0 = 0, \tag{C.20}$$

where

$$
\begin{aligned}
a_3 &= (\alpha^2-1)^3(E^2-1) \\
a_2 &= (\alpha^2-1)^2(\alpha^2+1)(1-3E^2) \\
a_1 &= (\alpha^2-1)^3 - L_z^2(\alpha^2-1)(\alpha^2+1)^2 + E^2(-3-7\alpha^2+7\alpha^4+3\alpha^6) \qquad \text{(C.21)} \\
a_0 &= -(\alpha^2+1)\Big\{(\alpha^2-1)^2 + 8EL_z\alpha(\alpha^2+1) + L_z^2(\alpha^2+1)^2 + E^2(1+14\alpha^2+\alpha^4)\Big\}. \qquad \text{(C.22)}
\end{aligned}
$$

Once in the form of a cubic polynomial this can be solved analytically, see for example [29]. I now cast the Manko-Novikov metric into the same polynomial shape (although, since it contains exponential expressions, it's not an actual polynomial). To solve $G_{MN} = 1$ I have to find the roots of the 'polynomial' in x, $b_3x^3 + b_2x^2 + b_1x^1 + b_0$ with coefficients

$$
\begin{aligned}
b_3 &= E^2(\alpha^2-1)^2[-e^{-A}e^{-2B} + \alpha^2e^A] + (\alpha^2-1)^2[e^{2C} - \alpha^2] \qquad \text{(C.23)} \\
b_2 &= 3E^2(\alpha^2-1)^2[-e^{-A}e^{-2B} - \alpha^2e^A] + (\alpha^2-1)^2[e^{2C} + \alpha^2] \qquad \text{(C.24)} \\
b_1 &= 3E^2(\alpha^2-1)^2[-e^{-A}e^{-2B} + \alpha^2e^A] \\
&\quad + 8e^{-A}e^{-B}E\alpha(\alpha^2-1)(L_z + 4E\alpha + L_z\alpha^2) \\
&\quad + (L_z + 4E\alpha + L_z\alpha^2)^2e^{-A}[e^{2C} - \alpha^2] + (\alpha^2-1)^2[-e^{2C} + \alpha^2] \qquad \text{(C.25)} \\
b_0 &= -E^2(\alpha^2-1)^2[e^{-A}e^{-2B} + \alpha^2e^A] \\
&\quad - (L_z + 4E\alpha + L_z\alpha^2)^2e^{-A}[e^{2C} + \alpha^2] - (\alpha^2-1)^2[e^{2C} + \alpha^2] \qquad \text{(C.26)}
\end{aligned}
$$

where

$$
\begin{aligned}
e^A &= e^{\alpha_2/r^3} \qquad \text{(C.27)} \\
e^B &= e^{[\alpha_2(-1+2r^3+x-2r^2x)/r^3]} \qquad \text{(C.28)} \\
e^C &= e^{[\alpha_2(-2-x/r^3+2x/r)]}. \qquad \text{(C.29)}
\end{aligned}
$$

Replacing these with their expansions around $x = 0$ to linear order in α_2 (after having replaced, $r = \sqrt{x^2-1}$), the cubic 'polynomial' from before can now be rewritten as quartic polynomial in x,

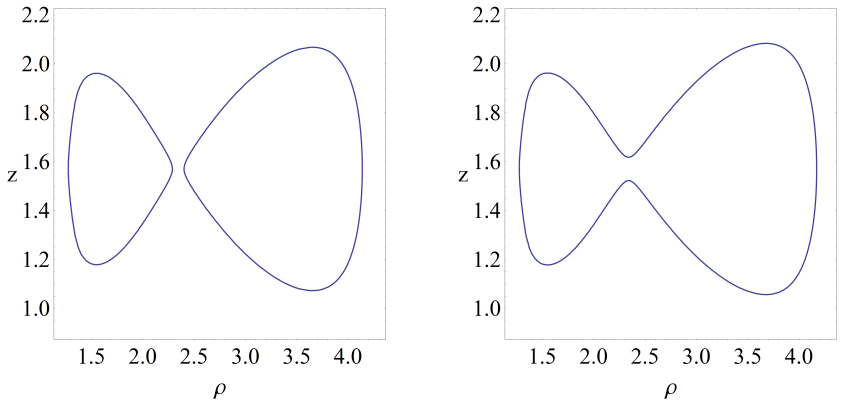

Figure C.2: **The values of the roots found numerically are for (a)** $\rho_1 \approx$ **4.13667,** $\rho_2 \approx 2.40154$, $\rho_3 \approx 2.28746$, $\rho_4 \approx 1.27546$ **and for (b)** $\rho_1 \approx$ **4.16974 and** $\rho_2 \approx 1.27546$**. The analytical roots, found by solving the above quartic polynomial (Eq.** (C.30)**) analytically for the parameter sets** $(E, L_z, S, q) = (0.95, 3, 0.9, 0.95)$ **and** $(E, L_z, S, q) = (0.951, 3, 0.9, 0.95)$ **are** $(\rho_1, \rho_2, \rho_3, \rho_4) \approx (1.94859, 0.35907 + 3.14i,$**4.13662, 2.53666)** **and** $(\rho_1, \rho_2, \rho_3, \rho_4) \approx (1.96059, 0.36200 + 3.14i,$**4.16971, 2.51136)**. In both cases the biggest numerical (underlined) root compares well with the biggest analytical root (underlined) for a given set of parameters.**

$$
\begin{aligned}
Q_{MN} = {} & (E^2-1)(\alpha^2-1)^3x^4 - (3E^2-1)(\alpha^2-1)^2(\alpha^2+1)x^3 \\
& (\alpha^2-1)[(\alpha^2-1)^2 - L_z^2(\alpha^2+1)^2 + E^2(3+10\alpha^2+3\alpha^4)]x^2 \\
& - [(\alpha^2-1)^2(\alpha^2+1) - E^2(\alpha^2-1)^2(\alpha^2+1) - \\
& (\alpha^2+1)(L_z + 4E\alpha + L_z\alpha^2)^2 + E^2(-1+\alpha^2)^3\alpha_2]x \\
& - \frac{3}{2}(\alpha^2-1)^2[1+E^2(1+2\alpha^2)]\alpha_2. \qquad \text{(C.30)}
\end{aligned}
$$

From this expression I can analytically solve for the biggest equatorial root for the Manko-Novikov metric. This is done by rewriting the quartic as a monic polynomial and changing variables to express it as a depressed quartic (i.e. the coefficient of the cubic term is zero). Finally the roots of the quartic polynomial are expressed in terms of a newly constructed cubic. For the details of this process see texts such as [34]. In my analytic calculations of the roots only the biggest root is accurate since approximating the exponents in Eq. (C.29) to linear order is only a good approximation for x or r big. The correspondence between the biggest numerical root and the calculated analytical root is shown in Figure C.2.

BIBLIOGRAPHY

[1] Theocharis A. Apostolatos, Georgios Lukes-Gerakopoulos, and George Contopoulos. How to Observe a Non-Kerr Spacetime Using Gravitational Waves. *Phys.Rev.Lett.*, 103:111101, 2009.

[2] V I Arnold. *Russian Math. Survey*, 18:85–193, 1963.

[3] V I Arnold. *Russian Math. Survey*, 18:9–36, 1963.

[4] V. I. Arnold. *Mathematical methods of classical mechanics, Graduate texts in mathematics*. New York: Springer, 1978.

[5] G. D. Birkhoff. Proof of poincaré's geometric theorem. *Trans. Amer. Math. Soc.*, 14:14 – 22, 1913.

[6] George David Birkhoff. *Dynamical Systems*. New York American Mathematical Society, 1927.

[7] J. Brink, M. Geyer, and T. Hinderer. Characterizing resonances in the kerr metric and the observational implications. *in prep.*

[8] Jeandrew Brink. Spacetime encodings. ii. pictures of integrability. *Phys. Rev. D*, 78:102002, 2008.

[9] Alessandra Buonanno. Gravitational waves. *ArXiv 0709.4682*, 2007.

[10] S. M. Carroll. *Spacetime and geometry. An introduction to general relativity*. Addison Wesley, 2004.

[11] B. Carter. Axisymmetric Black Hole Has Only Two Degrees of Freedom. *Phys.Rev.Lett.*, 26:331–333, 1971.

[12] Brandon Carter. Global structure of the kerr family of gravitational fields. *Physical Review*, 174(5):1559–1571, 1968.

[13] Nathan A. Collins and Scott A. Hughes. Towards a formalism for mapping the spacetimes of massive compact objects: Bumpy black holes and their orbits. *Phys. Rev. D*, 69:124022, Jun 2004.

[14] G. Contopoulos. *Astron J.*, 76:147, 1971.

[15] G. Contopoulos, M. Harsoula, and G. Lukes-Gerakopoulos. Periodic orbits and escapes in dynamical systems. *Celestial Mechanics and Dynamical Astronomy*, 113:255–278, July 2012.

[16] G. Contopoulos, G. Lukes-Gerakopoulos, and T. A. Apostolatos. Orbits in a non-kerr dynamical system. *ArXiv 1108.5057*, 2011.

[17] George Contopoulos. Higher order resonances in dynamical systems. *Celest. Mech.*, 18:195, 1978.

[18] George Contopoulos. *Order and Chaos in Dynamical Astronomy*. Springer, 2002.

[19] A. Einstein. Die Grundlage der allgemeinen Relativitätstheorie. *Annalen der Physik*, 354:769–822, 1916.

[20] G.F.R. Ellis. Classnotes: Course on General Relativity. *Applied Mathematics University of Cape Town*, 2009.

[21] Frederick J Ernst. New formulation of axially symmetric gravitational field problem. *Physical Review*, 167(5):1175, 1968.

[22] Jonathan R Gair, Chao Li, and Ilya Mandel. Observable properties of orbits in exact bumpy spacetimes. *Phys. Rev. D*, 77:024035, 2008.

[23] R. Geroch. A Method for Generating Solutions of Einsten's Equations. *Journal of Mathematical Physics*, 12:918–924, June 1971.

[24] R. Geroch. A method for generating new solutions of Einstein's equation. II. *Journal of Mathematical Physics*, 13:394–404, 1972.

[25] Marisa Geyer and Jeandrew Brink. Of Butterflies and Bumpy Black Holes. *Quest*, 28 - 32:042003, 2012.

[26] S. Gillessen, F. Eisenhauer, S. Trippe, T. Alexander, R. Genzel, et al. Monitoring stellar orbits around the Massive Black Hole in the Galactic Center. *Astrophys.J.*, 692:1075–1109, 2009.

[27] K. Glampedakis. Extreme mass ratio inspirals: LISA's unique probe of black hole gravity. *Class.Quant.Grav.*, 22:S605–S659, 2005.

[28] Kostas Glampedakis and Stanislav Babak. Mapping spacetimes with LISA: Inspiral of a test-body in a 'quasi-Kerr' field. *Class.Quant.Grav.*, 23:4167–4188, 2006.

[29] Karl Hahn. Solving Cubic and Quartic Polynomials. *http://www.karlscalculus.org/pdf/cubicQuartic.pdf*, Jul. Jul. 2005.

[30] R.O. Hansen. Multipole moments of stationary space-times. *J.Math.Phys.*, 15:46–52, 1974.

[31] S.W. Hawking. Black holes in general relativity. *Commun.Math.Phys.*, 25:152–166, 1972.

[32] S.W. Hawking and G.F.R. Ellis. *The Large Scale Structure of Space-Time*. Cambridge: Cambridge University Press, 1973.

[33] T. Johannsen and D. Psaltis. Testing the No-hair Theorem with Observations in the Electromagnetic Spectrum. II. Black Hole Images. *Astrophys.J.*, 718:446–454, July 2010.

[34] John Kennedy. Solving Quartic Equations. *http://homepage.smc.edu/kennedy_john*, Jan. 2012.

[35] R. P. Kerr. Gravitational Field of a Spinning Mass as an Example of Algebraically Special Metrics. *Physical Review Letters*, 11:237–238, September 1963.

[36] R. P. Kerr. Discovering the Kerr and Kerr-Schild metrics. *ArXiv 0706.1109*, June 2007.

[37] Bence Kocsis, Alak Ray, and Simon Portegies Zwart. Mapping the Galactic Center with Gravitational Wave measurements using Pulsar Timing. *arXiv 1110.6172*, 2011.

[38] Hideo Kodama and Wataru Hikida. Global structure of the Zipoy-Voorhees-Weyl spacetime and the $\delta = 2$ Tomimatsu-Sato spacetime. *Class. Quantum Grav.*, 20:5121–5140, 2003.

[39] John Kormendy and Douglas Richstone. Inward bound: The Search for supermassive black holes in galactic nuclei. *Ann.Rev.Astron.Astrophys.*, 33:581, 1995.

[40] M Kruskal. *Journal of Math. Phys.*, 3:806–828, 1962.

[41] T. Lewis. Some Special Solutions of the Equations of Axially Symmetric Gravitational Fields. *Royal Society of London Proceedings Series A*, 136:176–192, May 1932.

[42] A. J. Lichtenberg and M.A. Lieberman. *Regular and Chaotic Dynamics, Second Edition*. Springer-Verlag, 1992.

[43] K. Liu, N. Wex, M. Kramer, J.M. Cordes, and T.J.W. Lazio. Prospects for Probing the Spacetime of Sgr A* with Pulsars. *Astrophys.J.*, 747:1, 2012.

[44] G Lukes-Gerakopoulos. Non-linear effects in non-kerr spactimes. In *Proceedings: Relativity and Gravitation 100 years after Einstein in Prague.* Edition Open Access, 25 - 29 June 2012.

[45] Georgios Lukes-Gerakopoulos, Theocharis A. Apostolatos, and George Contopoulos. An observable signature of a background deviating from the kerr metric. *Phys. Rev. D*, 81:124005, Jun 2010.

[46] Vladimir S Manko and Igor D Novikov. Generalizations of the kerr and kerr - newman metrics possessing an arbitrary set of mass-multipole moments. *Class. Quantum Grav.*, 9:2477–2487, 1992.

[47] C. W. Misner, K. S. Thorne, and J. A. Wheeler. *Gravitation.* W.H. Freeman and Company, 1973.

[48] J Moser. *Stable and Random Motions in Dynamical Systems.* Princeton, NJ : Princeton University Press, 1973.

[49] R. Penrose. The topology of ridge systems. *Ann. Hum. Genet., Lond.*, 42:435, 1979.

[50] H Poincaré. *Méthodes Nouvelles de la Méchanique Celeste vol 2.* Paris: Gauthier-Villars, 1893.

[51] H. Poincaré. Sur un théorème de géométrie. *Rend. Circ. Mat. Palermo*, 33:375 – 407, 1912.

[52] Matlab R2008b. The Language of Technical Computing. *Product Help.*

[53] F.D. Ryan. Gravitational waves from the inspiral of a compact object into a massive, axisymmetric body with arbitrary multipole moments. *Phys. Rev. D*, 52:5707–5718, 1995.

[54] Wolfram Schmidt. Celestial mechanics in kerr spacetime. *Class. Quantum Grav.*, 19(10):2743–2764, 2002.

[55] Heinz Georg Schuster and Wolfram Just. *Deterministic Chaos, An Introduction.* WILEY-VCH Verlag GmbH & Co. KGaA, 2005.

[56] H. Stephani, D. Kramer, M. MacCallum, C. Hoenselaers, and E. Herlt. *Exact Solutions of Einstein's Field Equations.* Cambridge University Press, London, 2003.

[57] Steven H. Strogatz. *Nonlinear Dynamics and Chaos with applications to Physics, Biology and Chemistry and Engineering*. Perseus Books, 1994.

[58] N Voglis and C Efthymiopoulos. Angular dynamical spectra. a new method for determining frequencies, weak chaos and cantori. *Journal of Physics A: Mathematical and General*, 31(12):2913, 1998.

[59] H. Weyl. Zur Gravitationstheorie. *Annalen der Physik*, 359:117–145, 1917.

[60] KJ Whiteman. Invariants and stability in classical mechanics. *Rep. Prog. Phys.*, 40:1033–1069, April 1977.